OPTICAL, ELECTRICAL, AND MAGNETIC FIELD STUDIES OF ORGANIC MATERIALS FOR LIGHT EMITTING DIODES AND PHOTOVOLTAIC APPLICATIONS

by

Tek Prasad Basel

A dissertation submitted to the faculty of
The University of Utah
in partial fulfillment of the requirements for the degree of

Doctor of Philosophy

in

Physics

Department of Physics and Astronomy

The University of Utah

December 2014

THE UNIVERSITY OF UTAH GRADUATE SCHOOL

STATEMENT OF DISSERTATION APPROVAL

The following faculty members served as the supervisory committee chair and members for the dissertation of **Tek Prasad Basel**

Dates at right indicate the members' approval of the dissertation.

Zeev Valy Vardeny , Chair		**07/18/2014** Date
Christoph Boehme , Member		**07/18/2014** Date
Brian Saam , Member		**07/18/2014** Date
Anil Seth , Member		**07/18/2014** Date
Michael Morse , Member		**07/18/2014** Date

The dissertation has also been approved by **Carleton DeTar**

Chair of the Department of **Physics and Astronomy**

and by **David B. Kieda**, Dean of The Graduate School.

ABSTRACT

We studied optical, electrical, and magnetic field responses of films and devices based on organic semiconductors that are used for organic light emitting diodes (OLEDs) and photovoltaic (OPV) solar cell applications.

Our studies show that the hyperfine interaction (HFI)-mediated spin mixing is the key process underlying various magnetic field effects (MFE) and spin transport in aluminum tris(8-hydroxyquinoline)[Alq_3]-based OLEDs and organic spin-valve (OSV). Conductivity-detected magnetic resonance in OLEDs and magneto-resistance (MR) in OSVs show substantial isotope dependence. In contrast, isotope-insensitive behavior in the magneto-conductance (MC) of same devices is explained by the collision of spin ½ carriers with triplet polaron pairs.

We used steady state optical spectroscopy for studying the energy transfer dynamics in films and OLEDs based on host-guest blends of the fluorescent polymer and phosphorescent molecule. We have also studied the magnetic-field controlled color manipulation in these devices, which provide a strong proof for the 'polaron-pair' mechanism underlying the MFE in organic devices.

The critical issue that hampers organic spintronics device applications is significant magneto-electroluminescence (MEL) at room temperature (RT). Whereas inorganic spin valves (ISVs) show RT magneto-resistance, MR>80%, however, the devices do not exhibit electroluminescence (EL). In contrast, OLEDs show substantive

EL emission, and are particularly attractive because of their flexibility, low cost, and potential for multicolor display. We report a conceptual novel hybrid organic/inorganic spintronics device (h-OLED), where we employ both ISV with large MR at RT, and OLED that has efficient EL emission.

We investigated the charge transfer process in an OPV solar cell through optical, electrical, and magnetic field measurements of thin films and devices based on a low bandgap polymer, PTB7 (fluorinated poly-thienothiophene-benzodithiophene). We found that one of the major losses that limit the power conversion efficiency of OPV devices is the formation of triplet excitons in the polymer through recombination of charge-transfer (CT) excitons at the interface, and presented a method to suppress the dissociation of CT states by incorporating the spin ½ additive, galvinoxyl in the bulk heterojunction architecture of the active organic blend layer.

To my parents, and my wife

CONTENTS

ACKNOWLEDGEMENTS

I would like to express my deepest gratitude to my advisor, Prof. Zeev Valy Vardeny, for his exemplary guidance, care, and constant encouragement. I was so fortunate to experience and learn from his knowledge, patience, and critical thinking which led to the completion of this study. I cannot express enough thanks to my supervisory committee members for their support: Professors Christoph Boehme, Brian Saam, Anil Seth, and Michael Morse. I must express my sincere thanks to Prof. Eitan Ehrenfreund, Prof. Tho Nyugen, and Prof. ChuanXiang Sheng for their research guidance, suggestions, and fruitful discussions.

I would like to thank Dr. Randy Polson, Dr. Mathew Delong, and Mr. Leonard Wojcik for their technical help in the lab and suggestions. My completion of this project could not have been accomplished without the support of my current group members, Dr. Dali Sun, Dr. Charlie Zhang, Uyen Huynh, Yaxin Zhai, Run Li, and Matthew Groesbeck. I would like to offer my special thanks to Ryan McLaughlin for proof reading the thesis and to Anil Ghimire for helping to resolve technical issues in writing. I would not forget my former group members Dr. Ye Zhang, Dr. Golda Hukic Markosian, Dr. Bill Pandit, Dr. Ella Olejnik, and Dr. Sanjeev Singh, who introduced me to the field and experimental techniques. I would like to thank Dr. Bhoj Gautam, who as a good friend was always willing to help and give his best suggestions.

I am indebted to my parents and family members for their love and inspiration

with their best wishes. I would like to express my gratitude to my caring and loving wife, Komal Bagale, for her continuous support and encouragement during my studies.

CHAPTER 1

INTRODUCTION

The most commonly used semiconducting material, silicon, has high carrier mobility and device stability. But the production of pure silicon is expensive since it occurs exclusively in oxidized states and its chemical reduction requires a large amount of energy [1]. In addition, fabricating the electronic device using inorganic materials requires multiple etching, deposition, and lithographic steps. In contrast, the possibility of chemically manipulating the material properties of polymers (plastics) combined with a variety of easy and cheap processing techniques has made polymer-based materials present in almost every aspect of modern society [2]. Although to date inorganic semiconductors are still the most popular materials in the electronic industry, the unique properties of organic semiconductors, such as electroluminescence, flexibility, solubility, light weight, low cost, and easily tunable bandgap, make them very attractive for a number of novel optoelectronic applications such as organic light emitting diodes (OLEDs) [3], organic photovoltaic cells (OPVs) [4], organic field effect transistors (OFETs) [5], organic spin valves [6], thin film magnetometers [7], etc. In the early days, polymers were considered to be insulators. However, in the 1970s, researchers succeeded doping the polymers, which increased their conductivity by several orders of magnitude, and this boosted the excitement surrounding polymer research from the practical point of

view. Several doping methods were introduced to produce conducting polymer known as "synthetic metals" [8]. In the present chapter, we present a brief review of π-conjugated polymer physics and applications in the fields of photovoltaics and light emitting diodes.

1.1 π-Conjugated Polymers (PCP)

Organic materials mainly consist of carbon atoms which have 4 valence electrons; 1 s electron and 3 p-electrons. In a molecule, the carbon atoms hybridize with other atoms to form covalent bonds. The bond between carbon and the other atoms may be single, double, or triple depending on the number of shared electrons, namely 1, 2, or 3. If all the valence electrons are singly bonded (sp^3 hybridization), they form the strong σ-bonding which leads to a bandgap of more than 5eV, and thus the molecule would be an insulator. In case of a double bond, known as sp^2 hybridization, several bonds become σ-bonded, whereas the other is a much weaker π-bond. Bonding and hybridization schemes are shown in Figure 1.1. The σ bonds are strong and determine the shape of the backbone, whereas the π-electrons are loosely bound, delocalized over a number of intrachain carbon atoms [9], and are primarily responsible for the electronic and optical properties of the polymer. Throughout this thesis, polymer refers to the carbon-based macromolecule of high molecular weight (>1000g/mole) that consists of a large number of repeat units forming a chain that may have side groups. The polymer with sp^2 hybridization, called π-conjugated polymer, has one π-electron per C-atom in the chain, forming a half-filled electronic band. However, this one-dimensional electron distorts and dimerizes, doubling the period of the π-electronic potential (Peierls' instability) due to electron-phonon coupling and electron-electron interactions and opens an energy gap at

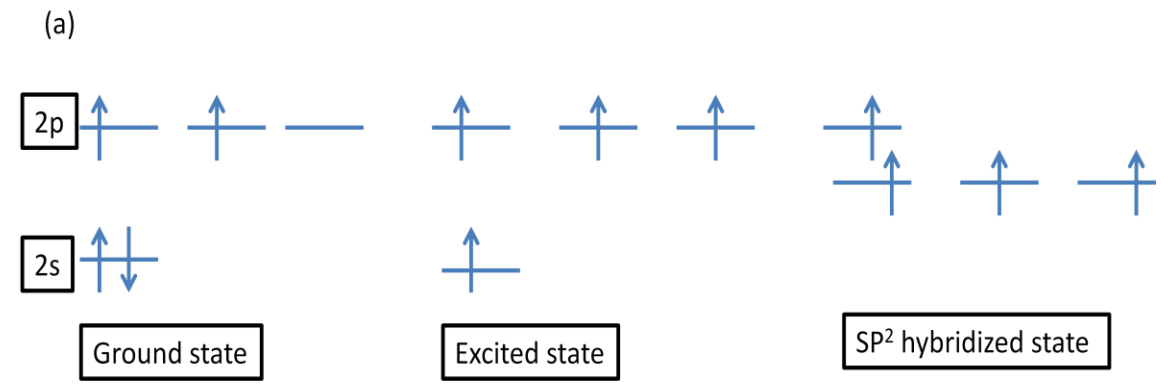

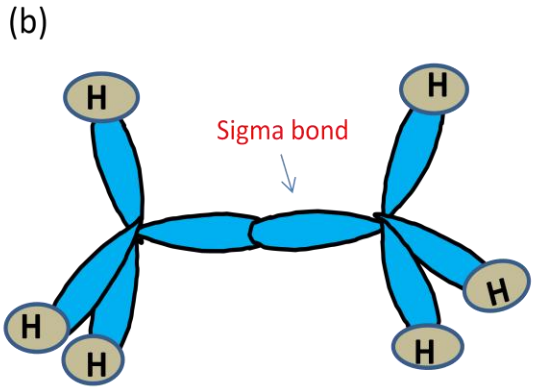

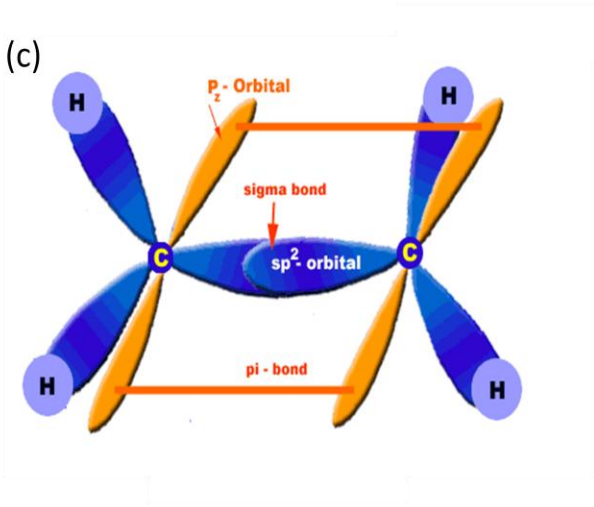

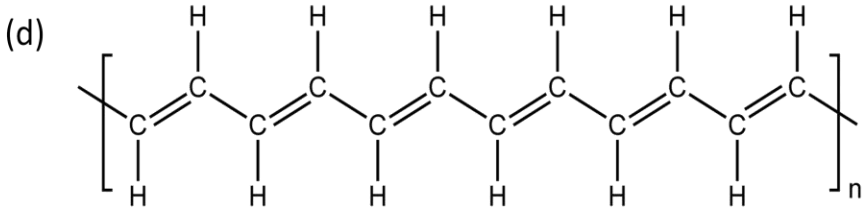

Figure 1.1. Bonding scheme for π-conjugated polymer. (a) SP^2 hybridization in excited states. Bond diagram for (b) SP^3 hybridization in ethane and (c) SP^2 hybridization in ethane (Adapted from www.collegiate.com). (d) Chemical structure of trans-polyacetylene; a π-conjugated polymer.

k= ±π/2a [10]. The energy gap between the highest occupied molecular orbital (HOMO) and the lowest occupied molecular orbital (LUMO) can be tuned with different molecular combinations of the polymer by changing the extent of π-electrons' delocalization. This makes the π-conjugated polymers exciting for both pure academic research and optoelectronic applications.

1.2 Excitation Models in π-Conjugated Polymers

Several models are introduced to explain the excitations in π-conjugated polymer. The simplest model, which only considers the nearest neighbour interactions based on the tight binding approximation, is the Huckel model [10]. This approximation well describes the bandgap of the polymer but cannot explain the excitation energy levels. The Su, Schrieffer, and Heeger (SSH) model [11] was introduced by incorporating only the electron-phonon interaction and a restoring energy. This model uses the semiclassical Hamiltonian which contains classically treated lattice kinetic energy and a quantum mechanically treated electron-phonon interaction as shown in Eq. (1.1).

$$H_{SSH} = \frac{k}{2}\Sigma_n (u_n - u_{n-1})^2 + \frac{M}{2}\Sigma_n (\frac{du_n}{dt})^2 - \Sigma_{n,s}(t_0 + \alpha(u_{n+1} - u_n))(C^+_{n+1,s}C_{n,s} + C^+_{n,s}C_{n+1,s}) \quad (1.1)$$

where t_0 is the hopping integral between the nearest neighbors for an undistorted chain, α is the electron lattice coupling constant, and $C^+_{n,s}$ and $C_{n,s}$ are the creation and annihilation operators of an electron on site n with spin s. k is the spring constant due to π-electrons and u_n is the deviation of n^{th} site from the equilibrium position in an undistorted chain with equal distance between sites. According to this model, the

dimerization lowers the system energy and opens an energy gap, $E_g = 2\Delta$, where $\Delta = 4\alpha u$, and u is the dimerization amplitude in equilibrium. Consequently, the occupied electronic states in equilibrium are lowered, resulting in a more stable configuration where the lattice constant is doubled.

In contrast, in the Hubbard model, only the repulsion between two electrons on the same site is included. Hubbard Hamiltonian is:

$$H_{Hubb} = U \sum_i n_{i,\uparrow} n_{i,\downarrow} \tag{1. 2}$$

where U is Coulomb repulsion between two electrons on the same site, $n_{i,\uparrow}$ and $n_{i,\downarrow}$ are the density operators for the electron with spin up and spin down, respectively. Since the Hubbard model does not take into account electron-phonon interaction, which is quite strong in the PCP, and the SSH model neglects the Coulomb repulsion, a combination of these two models, known as the Pariser-Parr-Pople (PPP) model [12], is more realistic to use for explaining the energy levels in PCP. This model can explain many aspects of the excited states in PCP, and was also used to explain the energy levels in fullerene molecules and nanotubes.

1.3 Major Excitations in the Class of π-Conjugated Polymers

The excitations in PCP can be classified in two classes, namely charged or neutral. When photons with above gap energy excite the PCP, neutral excitations, called excitons, are created. Initially, they have spin 0, and later they may either undergo intersystem crossing to the triplet manifold having spin 1, or dissociate into two separate charges, called polarons. In electrical excitation (i.e. current injection), charged excitations (polarons) are formed first, which later recombine to form neutral polaron

pairs that recombine to form singlet and triplet excitons. Here, we will discuss these two major type of excitations.

1.3.1 Excitons

Singlet excitons (SE) are formed when an electron is promoted from HOMO to LUMO upon photon absorption. Excitons in PCP are coulombically bound electron-hole pairs and have binding energy of the order of ~0.5eV. SE may either radiatively recombine to the ground state by emitting light called photoluminescence (PL) or transfer to the triplet exciton (TE) state. Both SE and TE are neutral excitations and the wavefunction that represents them can be constructed by using the Slater determinant:

$$\Psi = \frac{1}{\sqrt{2}}\begin{vmatrix} \psi_i(r)\chi_i(\sigma) & \psi_i(r')\chi_i(\sigma') \\ \psi_j(r)\chi_j(\sigma) & \psi_j(r')\chi_j(\sigma') \end{vmatrix} \tag{1. 3}$$

where $\psi_i(r)$ and $\chi_i(\sigma)$ are the spatial and the spin part of the wavefunction, respectively. The total spin quantum number (S) can be either 0 for SE and or 1 for TE. Thus, there are a total of four states whose wavefunctions are as follows:

$$\Psi^{S=0} = \frac{1}{2}[\psi_1(1)\psi_2(2) + \psi_2(1)\psi_1(2)][\uparrow(1)\downarrow(2) - \uparrow(2)\downarrow(1)] \tag{1. 4}$$

$$\Psi^{S=1} = \frac{1}{2}[\psi_1(1)\psi_2(2) - \psi_2(1)\psi_1(2)][\uparrow(1)\downarrow(2) + \uparrow(2)\downarrow(1)] \tag{1. 5}$$

$$\Psi^{S=1} = \frac{1}{2}[\psi_1(1)\psi_2(2) + \psi_2(1)\psi_1(2)][\uparrow(1)\uparrow(2)] \tag{1. 6}$$

$$\Psi^{S=1} = \frac{1}{2}[\psi_1(1)\psi_2(2) + \psi_2(1)\psi_1(2)][\downarrow(1)\downarrow(2)] \tag{1. 7}$$

where ↑ and ↓ symbols represent the spin projection of χ as up and down, respectively. In case of interacting spins, SE and TE energy levels are separated by exchange energy, and

usually the triplet has the lower energy level. Singlet exciton bands are shown in Figure 1.2(a). In the energy band diagram, $1A_g$ is the ground state and $1B_{u,}$ mA_g, and kA_g are the excited singlet states, where g stands for gerade (even parity) and u stands for ungerade (odd parity). The dipole coupled transitions from $1B_u$ to higher lying A_g states are shown in this figure by the vertical arrows which can be observed by ultrafast pump-probe techniques. Singlet exciton from $1B_u$ state can either decay to the ground state, emitting PL or heat in Figure 1.2(a), or convert to triplet 1^3B_u state. Triplet excitons are long-lived species and thus can be probed with CW pump-probe techniques.

Sometimes, a triplet exciton can radiatively decay in the presence of a spin flipping mechanism such as spin-orbit coupling; this type of emission is called phosphorescence and typically has longer lifetime, on the order of milliseconds [13]. Phosphorescence is not a general case in organic materials, so we have to use the photo-induced absorption technique to monitor the density of the triplet excitons in the material, where transitions in the triplet manifold may occur, as shown in Figure 1.2(b).

1.3.2 Polarons

The intermolecular forces in organic molecules are due to Van der Waals interaction, which is much weaker than the covalent or ionic bonding in inorganic materials. Consequently, a moving charge carrier can distort the lattice and thus form a quasi-particle called polaron where the lattice deformation moves along with the charge carrier. A polaron can be charged positively (P^+) or negatively (P^-) and has spin ½. It has two localized states within the gap that lead to two allowed transitions, P1 and $P_{2,}$ as shown in Figure 1.3. Polarons can be created in several ways: chemically by doping,

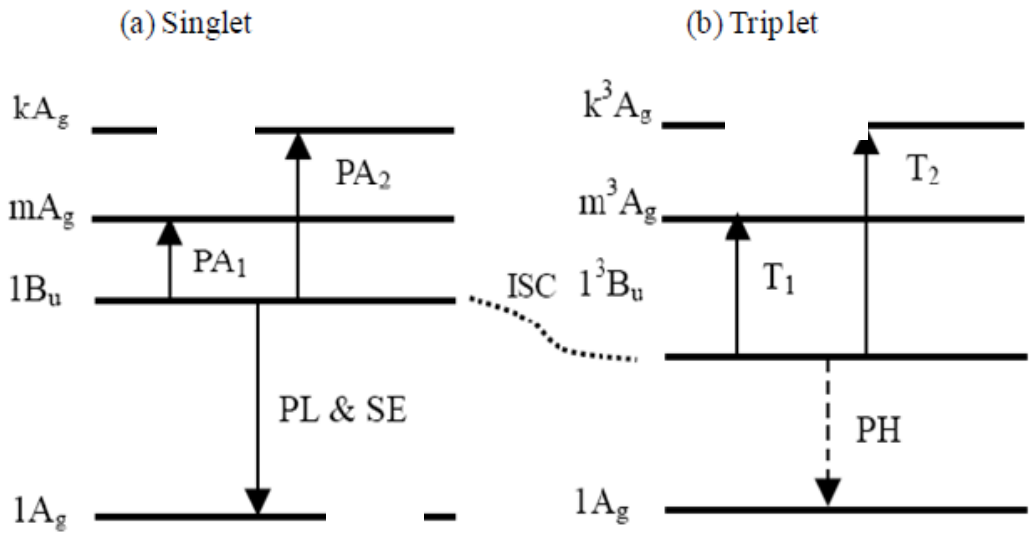

Figure 1.2. Neutral photoexcitations in PCP. (a) Singlet exciton and (b) triplet exciton energy levels and the transitions.

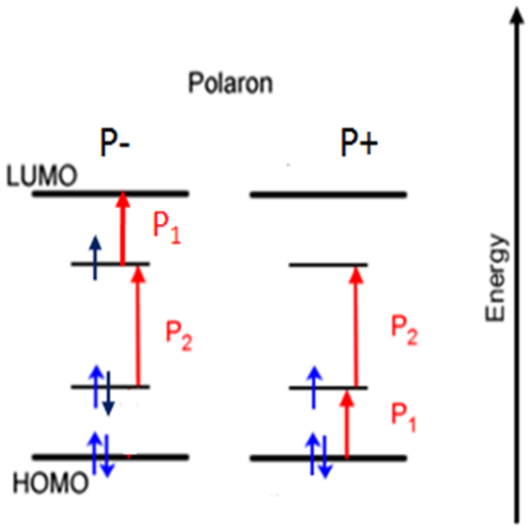

Figure 1.3. Charged excitations in PCP and their related optical transitions. Negative polarons on the left and positive polaron on the right.

optically by photon absorption, and electrically by carrier injection. Polaron transitions can be observed by CW pump-probe method. In general, we get both excitons and polarons in the pump-probe technique and there are several ways two identify them. In this thesis, Doping-induced Absorption (DIA), Magneto-Photo-induced Absorption (MPA), and the Optically-detected Magnetic Resonance (ODMR) methods are employed to identify the polaron transitions. Polarons move from chain to chain by hopping through the discrete and localized energy levels, and they are the major charge carrier in organic devices such as photovoltaic and light emitting diodes.

1.3.3 Other Excitations

Besides excitons and polarons, there are several other excitations discussed in the literature (e.g. polaron pairs, bipolarons, excimers, exciplexes, etc). Excimers and exciplexes are interchain species, which are generated due to the interaction of two adjacent chains in PCPs. They are formed when the neighboring molecules share the excited state π-electrons. The formation of an excimer is accompanied by a strong geometric distortion along the intermolecular axis. Excimers usually quench the luminescence due to their large nonradiative decay rate. If sharing of the electrons is not equal in terms of π-electron density, exciplexes are formed with a partial degree of charge transfer character.

Polaron pairs (PPs) are the combination of two oppositely charged polarons formed on adjacent polymer chains [14]. PPs are coulombically bound intermediate state between free polarons and excitons. A polaron pair may be formed either by the relaxation of a high energy singlet exciton, which is known as geminate pair and thus

initially has spin 0, or by the polarons from an unrelated electron and hole which is known as a nongeminate pair and can have both spin 0 and 1. Two polarons of the same charge on the same site is called bipolaron (BP). BPs are formed in cases of high polaron density of one charge that is formed by heavily doping, which can distort the lattice to overcome the coulomb repulsion.

1.4 Organic Photovoltaic (OPV)

To address the issue of the energy crisis, people are constantly looking for renewable energy sources, and the solar cell is one alternative. Although inorganic solar cells were invented and commercialized several decades ago, their complicated fabrication process makes them too expensive, and so research into their counterpart, organic solar cells, has been carried on. However, low power conversion efficiency (PCE), degradation, and limited lifetime of the OPV are the main challenges to be improved prior to commercialization. Light absorption in OPV based on pristine polymers is followed by exciton formation and their dissociation into polarons, which has low mobility compared to free carriers in inorganic solar cells. Furthermore, the intermediate step of exciton dissociation is not efficient enough to achieve high PCE and is not clearly understood to date. The exciton dissociation efficiency increases when two organic semiconductors are mixed together. Then one acts as donor, and the other acts as acceptor. This is the case when PCPs are mixed with fullerene molecules. Under this condition, the PCP acts as donor (D) and the fullerene molecule acts as acceptor (A).

The device structure of the OPV cell is as follows: Anode/organic layer/Cathode. Usually, transparent ITO-coated glass slides are used as a substrate and serve as the

anode followed by the PEDOT:PSS as the hole transport layer and calcium (Ca) and Aluminum (Al) are used as cathode and capping layer, respectively. The organic layer can be a single layer, bilayer/multilayer, or D-A bulk heterojunction (BHJ). In single layer OPV, excitons cannot dissociate easily, whereas a bilayer, which consists of two materials, donor and acceptor, creates an internal electric field which allows them to dissociate more easily [15]. Excitons have the diffusion length of only a few nm, so the excitons created far from the Donor/Acceptor (D/A) interface will not be able to dissociate. There will be "photon loss" without absorption if the layers are too thin and "exciton loss" without dissociation if the layers are too thick. To overcome this situation, either the D/A multilayer or a BHJ solar cell is introduced [16]. BHJs are a solution processed, phase separated, interpenetrating network of D/A domains [17, 18]. If the exciton diffusion length is comparable to the domain size of the donor polymer, then each exciton has the possibility to dissociate. For the efficient transport of the charges, continuous pathways to the electrode are needed, which may not always be the case (for example, polymer domains are surrounded completely by the fullerenes and vice-versa) and so, there has been tremendous effort put toward improving morphology [19].

The working principle of OPV is shown in Figure 1.4. First, photons are absorbed by the polymer creating the excitons. Low bandgap polymers are developed, which can absorb the infrared solar spectrum and so increase the number of absorbed photons. Second, excitons diffuse toward the D-A interface within a time range of picoseconds [20, 21], and form the CT-state upon arrival [22, 23]. Third, CT excitons dissociate into weakly bound PPs at the interface. CT-excitons may relax to form the triplet exciton or decay radiatively or nonradiatively [24] contributing to the loss mechanism. Fourth,

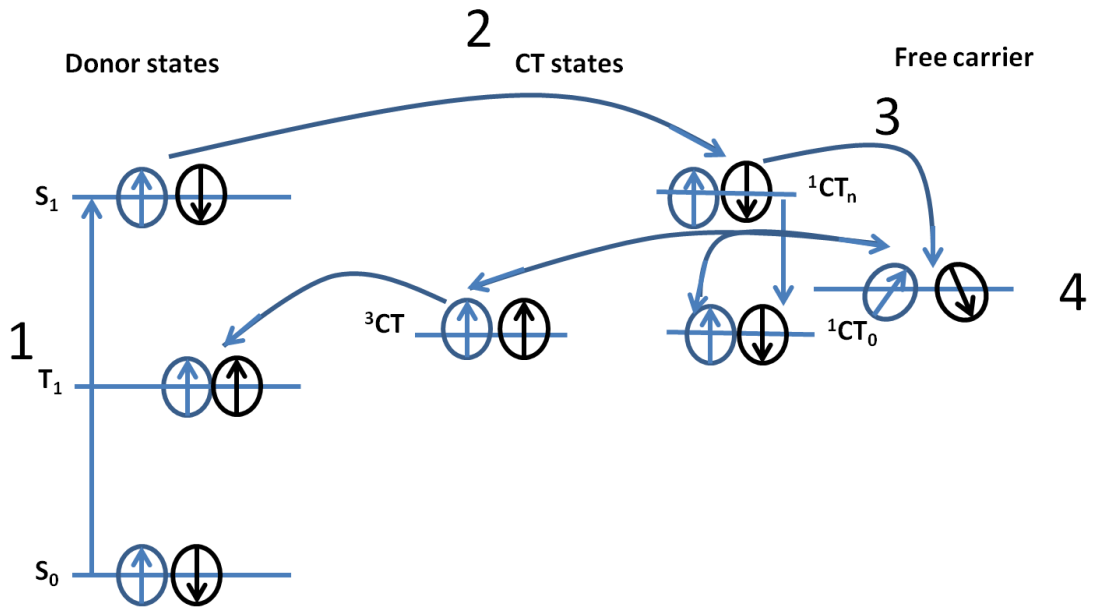

Figure 1.4. Working scheme in OPV. Process 1: Absorption of photon. Process 2: Exciton diffusion towards the interface. Process 3: Exciton dissociation to form the free carriers. Process 4: Charge carrier transportation towards the electrode.

separated free polarons move toward the respective electrode producing the photo-current (PC). The PCE of OPV depends on the efficiency of the above-mentioned four processes: absorption, diffusion, dissociation, and transport. Details of the photovoltaics' I-V characteristics under illumination will be explained in Chapter 2 section 2.9.

1.5 Organic Light Emitting Diodes

Organic light emitting diodes (OLED) use the organic layer as an emissive electroluminescence layer sandwiched between the electrodes. Interest in OLED was initiated by Tang and Vanslyke in 1987 [25] where they used Alq_3 as the organic layer. Later, polymer LEDs were introduced [3] and consistent efforts aimed to optimize the device working condition and maximize electroluminescence quantum efficiency. Typical device structure and the working processes are shown in Figure 1.5. Instead of injecting photons to produce the excitons as in OPV, electrical current is injected from the electrodes in OLED. The device structure is similar as in OPV, except that an emissive layer replaces the organic BHJ layer. Materials for anode, cathode, and carrier transport layers are selected by matching the HOMO/LUMO of the semiconductor and the work-function of the metal electrode. Carrier injected through the electrodes enters the emissive layer where it transports by hopping [26] between the discrete localized LUMO levels, since the energy levels do not form the band due to defects, distribution of chain length, and the kinks. Holes and electrons injected in the polymer may form the following three different species: (i) polaron pairs formed by oppositely charged carriers in adjacent chains bounded by coulombic interaction, (ii) bipolarons formed by same charged pairs in the segment of the chain, and (iii) excitons formed by the two closely

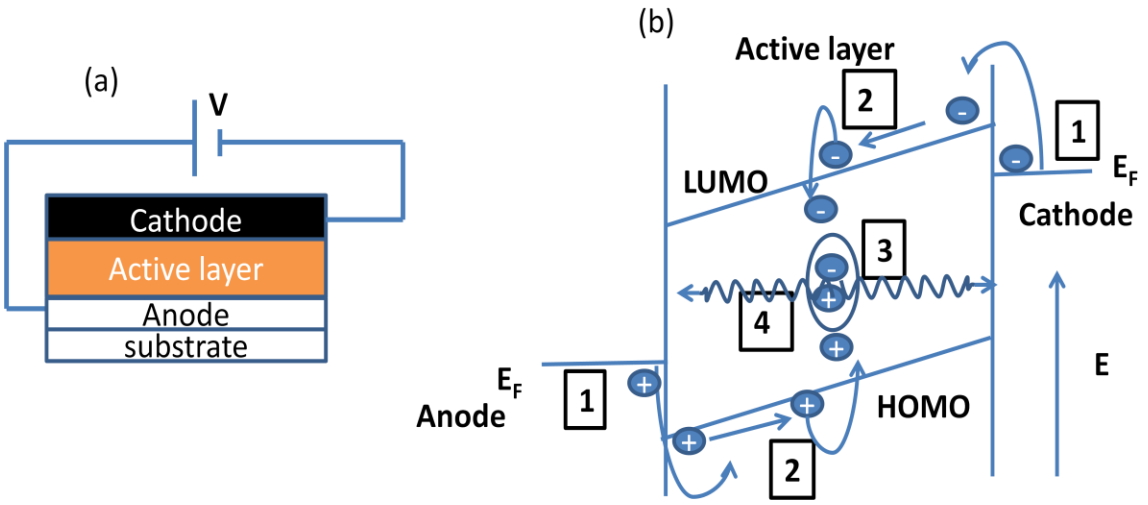

Figure 1.5. Organic light emitting diode. (a) Device structure. (b) Working scheme: 1. Charge carrier injection. 2. Charge carrier transport. 3. e-h pair, and then exciton formation. 4. Exciton decay (light emission).

separated oppositely charged carriers on the same chain due to coulombic interactions. Singlet excitons within the coulomb capture radius $r_{c,}$ given by Eq. (1.8) will recombine and emit light.

$$r_c = \frac{q^2}{4\pi\epsilon_r\epsilon_0 KT} \tag{1. 8}$$

The EL internal quantum efficiency, η_{int}, of the OLED is the product of the three factors [27]:

$$\eta_{int} = \eta_1\eta_2\eta_3 \tag{1. 9}$$

where η_1 is the fraction of excitons formed to the number of carriers injected, η_2 is the fraction of radiative singlet excitons to the total number of excitons, and η_3 is the quantum efficiency of fluorescence. EL external quantum efficiency (ELQE) is the product of η_{int} and the light output coupling factor, η_{ph}~20%. If all and only the singlet excitons are emissive, η_{int} approaches 25% and ELQE approaches 5%. Phosphorescent OLEDs [28] and delayed fluorescence [29] are intensively studied to harvest both singlets and triplets so that η_{int} reaches 100% and the ELQE limit increases to 20%.

The I-V and EL-V curve for the MEHPPV-based OLED is shown in Figure 1.6. At bias voltages lower than the built-in voltage, thermally generated carriers contribution is dominant, which follows the ohm's law of voltage-current relation. Upon increasing the bias voltage, injected carriers form a space charge layer near the injecting metal/organic interface due to their low mobility. The current flow, J, is then governed by space charge limited current (SCLC) defined by Child's law [30]:

$$J = \frac{9\epsilon\mu V^2}{8L^3} \tag{1. 10}$$

where ϵ is the electric permittivity, μ is the mobility and L is the thickness of the organic

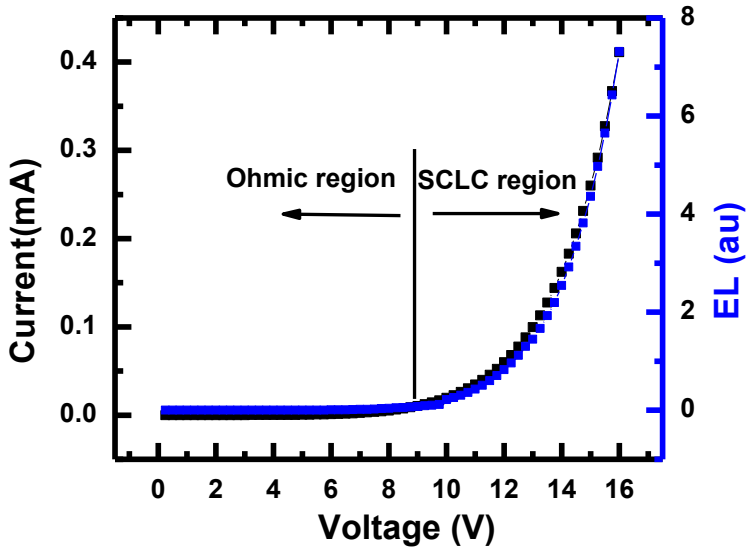

Figure 1.6. I-V and EL-V Characteristics of MEHPPV-based OLED.

layer. In the presence of traps, J is proportional to V^n on increasing the voltage before reaching the trap free regime [31]. In case of bipolar injection, μ is replaced by the $\mu_{eff,}$ which is given by,

$$\mu_{eff} = \frac{2}{3}[2\pi(\mu_e\mu_h(\mu_e + \mu_h)/\mu_0]^{\frac{1}{2}} \quad (1.\ 11)$$

where μ_0 is the recombination mobility [32].

1.6 The Magnetic Field Effect in Organic Semiconductors

Recently, there has been growing interest in the magnetic field effect (MFE) in organic semiconductors. Magnetic field can change PA in the polymer film, conductance/resistance (MC/MR), and luminescence in OLEDs. There are also comprehensive studies on organic spin valve devices where spin-polarized charge carriers are injected through the ferromagnetic electrodes into the organic layer explained on the basis of giant magneto-resistance [33] and tunneling magneto-resistance [34]. However, in this thesis, we will focus on the MFE on OLEDs and films with no ferromagnetic materials. Kalinowski et al. [35] demonstrated that electroluminescence and resistance can be modulated by a small magnetic field of the order~10 mT, the phenomenon is commonly known as magneto-resistance (MR). Magnetic field-induced change in the current, MC, defined by MC= (I(B)-I(0))/I(0) typically shows a Lorentzian ($B^2/(B^2+B_0{}^2$) or non-Lorentzian ($B^2/(|B|+B_0)^2$) response, and its sign depends on the device architecture and materials, operating voltage, temperature, etc. A typical response of MC and MEL of MEHPPV OLED will be discussed in Chapter 2 section 2.10. It is generally accepted that the underlying mechanism for the MFE in the organics is the magnetic field modulation of singlet and

triplet spin states that are mostly mediated by hyperfine interaction that affects their populations and dynamics. Several mechanisms for explaining MFE have been proposed: (i) spin mixing in polaron pairs [36] or bipolarons [37], (ii) difference in g-factor (Δg) of electron and hole [38], (iii) a number of mechanism involving triplet excitons: exciton charge interaction [39], triplet-triplet annihilation [40], and (iv) spin-orbit coupling in small molecules containing heavy atoms [41].

In the bipolaron model, bipolaron formation between opposite spins occurs at lower energy states, overcoming the coulomb repulsion. Bipolarons with parallel spins cannot form due to the Pauli exclusion principle. In transport, the magnetic field prevents the polarons from hopping through sites that have the same spin, and so forcing the charges to take another route and thereby changing the mobility. This causes the change in the current in response to the magnetic field and thus causes magneto-current response. In the triplet exciton model, Desai et al. proposed that triplet excitons in the active layer react with paramagnetic centers such as free charges forming triplet-charge pairs, which either scatters back to triplet and free carrier or dissociates into free carrier and excited ground state $(P + T) \overset{k_1}{\leftrightarrow} (P..T) \overset{k_2}{\leftrightarrow} (P + S_0^*)$.

In the 'polaron pair' model, the magnetic field mixes the spin singlet and triplet due to hyperfine interaction with the different rate after lifting the degeneracy of the triplet levels as shown in Figure 1.7 [42]. The conversion of singlet (S) to triplet occurs with entire triplet manifolds (T_+, T_0, T_-) and only with the triplet level T_0 in the absence and presence of magnetic field, respectively. Since dissociation and recombination rates for singlets and triplets are different, OMAR response is observed. If a finite exchange interaction between the pair is considered, then there will be excess spin mixing between

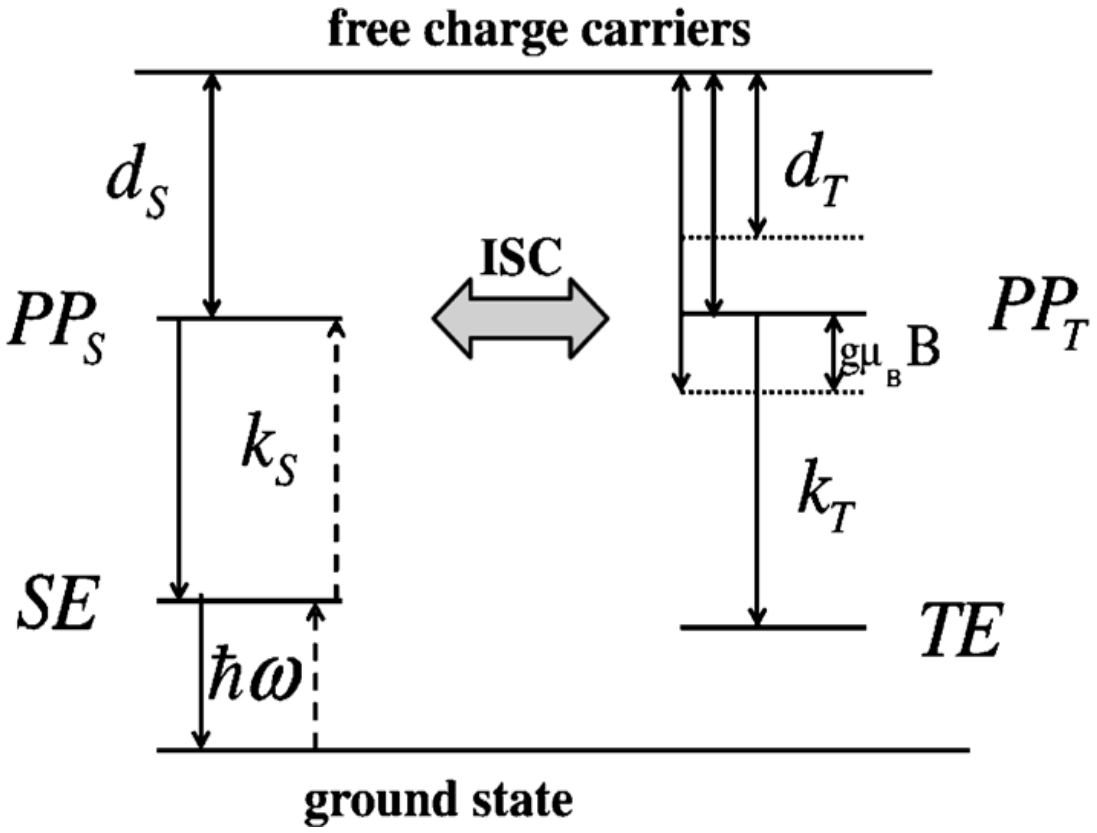

Figure 1.7. Polaron pair mechanism. Top to bottom: Injected negative and positive free charges form loosely bound shallow PP in either singlet PP_S or triplet PP_T configuration. There is substantial intersystem conversion (ISC) between singlet and triplet PP due to, e.g., the hyperfine interaction. d_S and d_T stand for the spin dependent PP dissociation rate back to free charges. k_S and k_T stand for the strongly bound singlet (SE) or triplet (TE) excitons generation rate. SE give rise to electro-luminescence with photon energy $\hbar w$. Bottom to top: A photon $\hbar w$ excites SE, which quickly charge separate into loosely bound PP (dashed arrows). The PP dissociate to free charges giving rise to electrical current. Figure adapted from reference [42].

singlets and triplets at a magnetic field that is equal to the exchange interaction (J). This effect is known as ‘level crossing’ (LC) and appears at ultra small magnetic field [43]. Finally in D-A blends, the electron and hole have different environment, and thus they possess different g-values. Under these conditions, the difference in spin precession frequency is $(g_1\text{-}g_2)\mu_B B/\hbar$; and this contributes to the PP spin-mixing mechanism at high magnetic fields, known as the Δg mechanism.

CHAPTER 2

EXPERIMENTAL TECHNIQUES

This chapter introduces the methods employed to study the photophysics of polymer films, as well as the fabrication and characterization procedures of OPV and OLED devices. Since the organic materials are susceptible to atmospheric degradation in air, our measurements have been carried out either in vacuum or in encapsulated devices that minimize the exposure to air (mainly oxygen and water vapor). Sample preparation and processing have been done inside a glovebox in nitrogen atmosphere.

2.1 Materials

All of the materials used in this thesis can be classified into two categories: small π-conjugated molecules and π-conjugated polymers. Small molecules have molecular mass of less than 1000 g/mol and do not contain repeat units, whereas polymers have very high molecular mass (say tens of thousands of grams/mole) and can be characterized by repeat units dubbed monomers or chromophores. Films from small molecules are grown by evaporation technique from the vapor phase, whereas the polymer can be easily dissolved in various organic solvents, and subsequently spin-coated on a substrate forming a rather ‘smooth’ film. These two types of materials differ in their synthesis, purification, and fabrication methods. Several materials used as active layers in organic

optoelectronic devices that are included in this thesis are shown in Figure 2.1 with their molecular structures. Table 2.1 summarizes the various materials and their usage. Most of the materials were commercially purchased or received from our collaborators, whereas DOOPPV is synthesized in our laboratory by the chemist Mr. Leonard Wojcik. Materials and the chemical reagents are used as received, without further purification.

2.2 Absorption and Emission Spectra

Absorption and emission spectra are the basic firsthand measurements for measuring the optical gap of the material, and determine the radiative excited states. The photon is absorbed from the ground state, S_0 to the excited state, S_1 of which transition probability depends on the coupling of the excited states to the ground state which includes parity, angular momentum, and oscillator strength.

The material absorption spectrum in the UV-visible and near infrared spectral range was measured using a CARY 17 spectrometer. The polymer solution is spin-coated onto a glass substrate, whereas the small molecule films are prepared by thermal evaporation onto glass or sapphire substrates. The 'substrate effect' in the absorption is canceled out by measuring the absorption of the clean substrate first and assigning this spectrum as the baseline for the sample absorption measurement. Scattering and reflection are supposed to be very small in organic films and no correction has been made to the transmission data. Absorption is calculated from the relation,

$$T = T_0 10^{-OD} \tag{2.1}$$

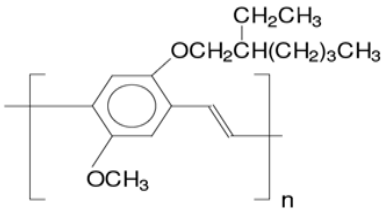

(a) Poly-[2-methoxy, 5-(2'-ethyl-hexyloxy)phenylene vinylene](MEH-PPV)

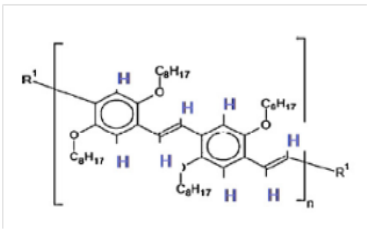

(b)Poly(dioctyloxy) phenylenevinylene (H-DOO-PPV)

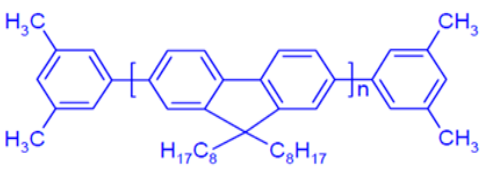

(c) Poly[2,7-(9,9-di{(*S*)-3,7-*dimethyloctyl*}*fluorene*)](*PFO*)

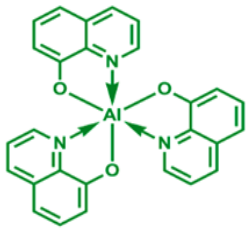

(d) Aluminum tris(8-hydroxyquinoline) [Alq_3]

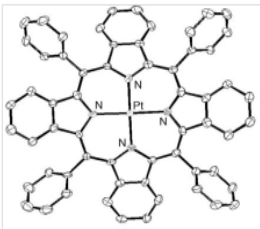

(e) PtII–tetraphenyltetrabenzoporphyrin [Pt(tpbp)]

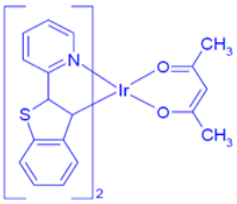

(f) Iridium (III) bis(2-(2'-benzo-thienyl) pyridinatoN,$C^{3'}$)(acetyl-acetonate)[$Ir(btp)_2acac$]

Figure 2.1. Molecular structures. (a) MEHPPV (b) DOOPPV (c) PFO (d) Alq3 (e) Pt(tpbp) (f) Ir(btp)2acac (g) P3HT (h) PTB7 (i) PDTP-DFBT (j) PC61BM (k) PC71BM and (l) Galvinoxyl.

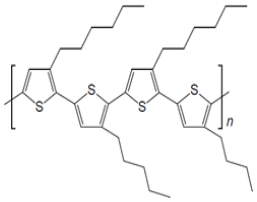

(g) Regio-Regular –Poly-(3-hexylthiophene) (RR P3HT)

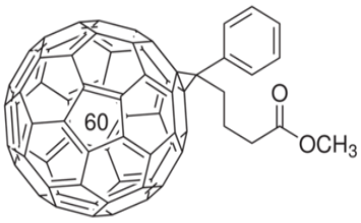

(j) [6,6]-Phenyl C61 butyric acid methyl ester ($PC_{61}BM$)

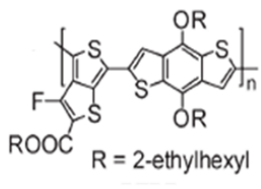

(h) Poly-thienothiophene-benzodithiophene 7 (PTB7)

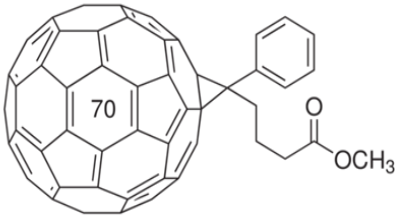

(k) [6,6]-Phenyl C71 butyric acid methyl ester($PC_{71}BM$)

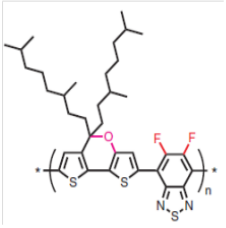

(i) Poly[2,7-(5,5-bis-(3,7-dimethyl octyl)-5H-dithieno[3,2-b:2',3'-d]pyran)-alt-4,7-(5,6-difluoro-2,1,3-benzothiadiazole)] (PDTP-DFBT)

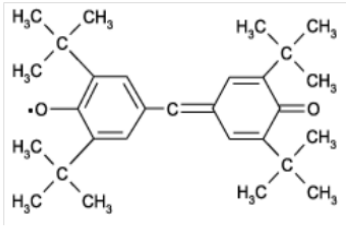

(l) 2,6-di-*t*-butyl-α-(3,5-di-*t*butyl-4-oxo-2,5-cyclohexadien-1-ylidene)-*p*-tolyloxy (Galvinoxyl)

Figure 2.1. Continued.

Table 2. 1. Organic materials and their usage.

Materials	**Used as**
P3HT, PTB7, PDTP-DFBT	Donor polymers in OPV devices
MEHPPV, Alq_3, PFO, DOOPPV	Active layer in OLED devices
PC61BM, PC71BM	Acceptor molecules in OPV cells
PEDOT:PSS	Hole transport layer in both OPV and OLED devices
TEMPO, BDPA, Galvinoxyl	Spin ½ additives in OPV cells
Pt(tpbp), $Ir(btp)_2acac$	Guest molecules in OLED devices

where T_0 and the T are the wavelength-dependent transmitted signal intensity before and after the sample, respectively. OD is the optical density which is the product of the absorption coefficient (α) and the thickness of the sample (d). Figure 2.2 (black curve) shows a typical absorption spectrum of DOOPPV polymer. The onset of the absorption indicates that the optical gap in this polymer is ~2.1 eV . There should be several replica bands due to transitions from the ground state to the vibrational levels 0, 1, 2,.. of the excited states, as shown in the Figure 2.2 inset. Since the measurement was done at room temperature, these vibrational bands overlap and cannot be resolved; hence they conspire to show a broader absorption spectrum.

For measuring the absorption spectrum in the mid-infrared spectral range, a Fourier transform infrared spectroscopy (FTIR) was used. In this method, a beam splitter splits the light from the source into two beams; one beam is reflected from the stationary mirror, and the other beam is reflected from the moving mirror. The two reflected beams are transmitted through the sample and the interference pattern is generated as a function of the mirror displacement. Fourier transform of this interferogram spectrum gives the absorption as the function of the wavelength in units of wavenumber (or cm^{-1}). In our measurements, we used FTIR to measure the charged excited states in the polymer after

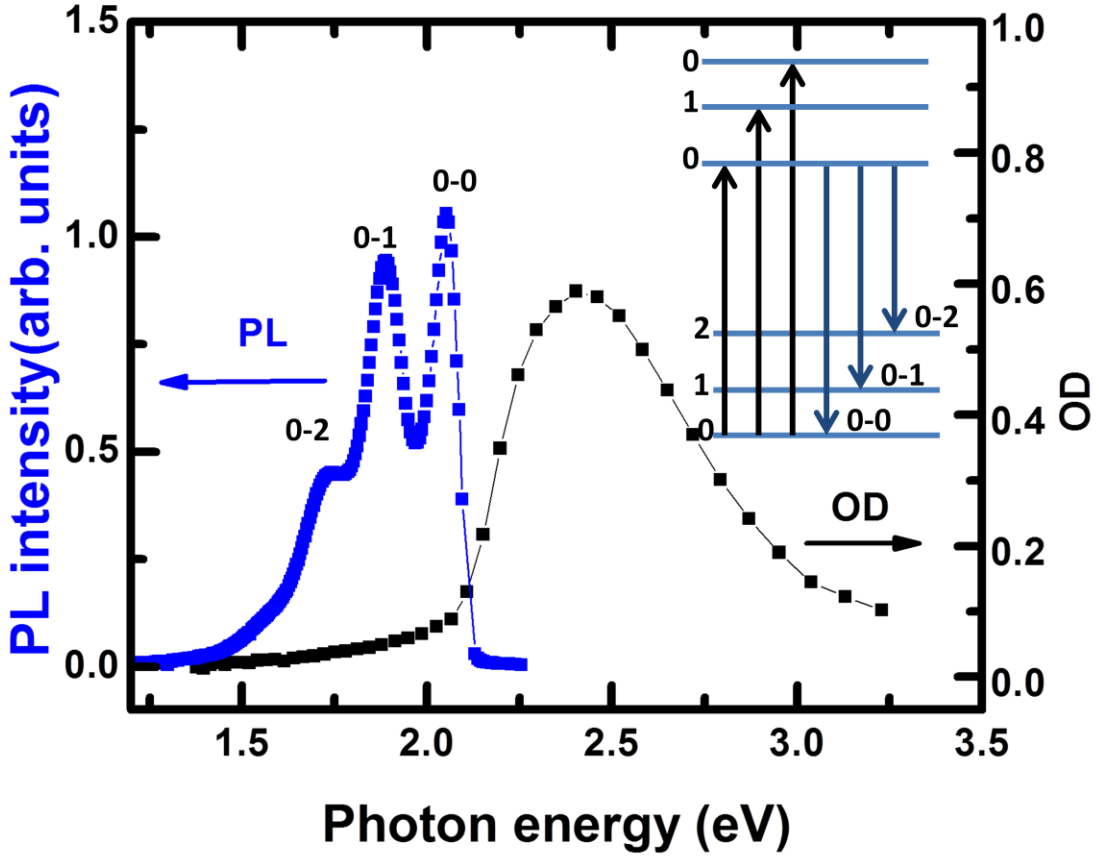

Figure 2.2. Absorption (black) and emission (blue) spectra of H-DOOPPV polymer film.

it is doped with some oxidizing agent; details are explained in section 2.4.

Once the electron is excited to a higher energy level, it decays to the ground state either radiatively in the form of fluorescence (FL) or nonradiatively in the form of heat. The radiative decay, where the excited state species emits a photon while reaching the ground state, can be measured using a photo-detector. For measuring the FL spectrum, a sample is deposited onto a sapphire substrate and kept inside a cryostat, since usually organic films are sensitive to the air. Appropriate pump energy that matches the material optical gap is used to excite the sample. Following Kasha's rule, the emission spectrum begins at the lowest vibrational level. Therefore, the FL emission is red shifted as compared to absorption, and depending upon the vibrational overlap, several phonon replicas can be observed as shown in Figure 2.2 (blue curve) for Hydrogenated-DOOPPV. In the plot, three distinct phonon bands 0-0, 0-1, and 0-2 are observed. These are the transitions from the lowest vibrational level (level 0) of the excited state to the vibrational levels 0, 1, and 2 of the ground state. The emission intensity depends on the overlap integral of the wave functions of the vibrational levels involved in transitions which is expressed in terms of Huang-Rhys parameter, S, determined by the exciton-phonon coupling strength. The relative intensity of the 0-0 band to the 0-1 band is quenched by the interchain aggregation formation in the polymer.

2.3 Photo-induced Absorption

Continuous wave (CW) Photo-induced Absorption (PA) is the method used to detect long-lived photoexcitation species. Unlike the PL, where the emission intensity is measured as the optical transition from the excited state to the ground state, in PA, we

measure the transition from the excited state to higher excited states. This is a kind of 'pump and probe' measuring technique, but using CW light sources. A CW Ar+ ion laser is usually used as the 'pump' beam to excite the sample, which is kept inside the cryostat provided with the closed cycle refrigerator for reaching cryogenic temperatures. The photogenerated species density is substantially higher at low temperature, because of increase in lifetime. Several diode lasers have been also used for the pump excitation in order to get a better signal to noise (S/N) ratio. For the probe beam, we have used a tungsten incandescent lamp with broad band emission from 4 micron to 0.4 micron. The probe light beam that passes through the sample is focused on a monochromator slit by a concave mirror as shown schematically in Figure 2.3. The monochromator grating, detector, and filters are adjusted according to the spectral range of interest, which spans from 450 nm to 4 μm. Proper combination of detectors and filters is shown in Table 2.2. Germanium (Ge) and Indium Antimonide (InSb) detectors are cooled by liquid Nitrogen to reduce the thermal noise as they have low bandgap. A combination of the filters, or band pass filter are used (the latter in case of low signal intensity). The signal from the detector is fed to a preamplifier, converted into voltage, and sent to a lock- in amplifier connected to a computer. Measurements are done as a function of temperature using a closed cycle cryostat that operates from 35K to room temperature. We used a mechanical chopper to modulate the pump intensity at frequency of 305 Hz.

Instead of measuring directly the absorption, transmission is measured and then the PA is calculated. The PA measurement consists of three different signals: (1) transmission intensity in the dark (T_D); (2) emission intensity (PL); and (3) difference between the transmission intensity when the pump is turned on, T_L and T_D (=ΔT). PL

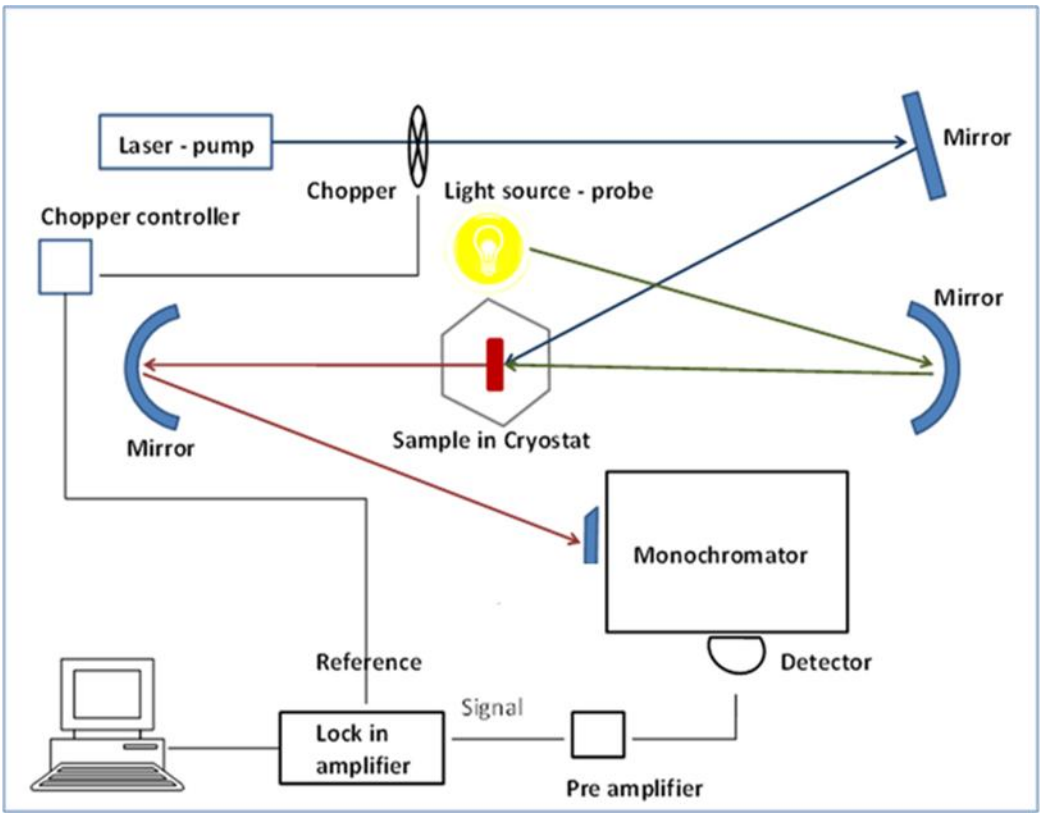

Figure 2.3. Experimental setup for PA measurement.

Table 2.2. Detector and filter combinations used for measuring PA spectrum in a broad spectral range.

Spectral Range(nm)	Detector	Filter
550-1000	Silicon (Si)	550 long pass
1000-1500	Germanium (Ge)	800 long pass
1300-2500	Indium Antimonide (InSb)	1300 long pass
2500-4200	Indium Antimonide (InSb)	2500 long pass

corrections were made wherever necessary. The number of excited species is directly proportional to the change in transmission as shown below.

$$\Delta T = T_L - T_D \tag{2.2}$$

$$T_L = T_D e^{-\Delta\alpha d} \tag{2.3}$$

From Eq. (2.2) and (2.3),

$$1 + \frac{\Delta T}{T_D} = e^{-\Delta\alpha d} \tag{2.4}$$

$$\Rightarrow \Delta\alpha d = -\ln\left(1 + \frac{\Delta T}{T_D}\right) \tag{2.5}$$

As $\Delta T << T_D$,

$$\Delta\alpha d = -\frac{\Delta T}{T_D} \tag{2.6}$$

Usually, PA spectrum contains both PA when $\Delta\alpha > 0$ and photo-induced bleaching PB, when $\Delta\alpha < 0$. In the case of PA, new transient photoexcitations are generated, whereas PB is due to depletion of the ground state optical transition by the pump.

Magnetic field induces changes in PA, which is dubbed magneto-PA(MPA); it is measured using the same setup as the PA. Electromagnet pole pieces are placed in plane to the sample across the cryostat. The PA spectrum with and without the magnetic field is measured and divided by the PA intensity without magnetic field to obtain the MPA (percentage), i.e,

$$MPA(B) = \frac{PA(B) - PA(0)}{PA(0)} \text{x } 100 \tag{2.7}$$

To obtain the desired magnetic field response of the PA spectrum in films, the monochromator was fixed at the desired wavelength where the triplet exciton PA or the polaron PA band were assigned, and the MPA is recorded while sweeping the magnetic field.

The PA is calculated from the negative fractional change in transmission, which is subjected to the relation:

$$-\frac{\Delta T}{T} = \Delta\alpha d = N_{ss}\sigma(E)d \tag{2.8}$$

where N_{SS} is the species steady state density, σ(E) is the photoexcitation optical cross-section, and E is the probe beam photon energy. Therefore, in a magnetic field, B, PA(B) is determined by the density $N_{SS}(B)$; which, in turn, is controlled by the photoexcitation species decay rate coefficient, k(B) [$N_{SS=}G/k$], where G is the generation rate. The X species (X may be a polaron pair, triplet or triplet-pair) has an excited state transition $X_0 \rightarrow X_1$, which is activated by the probe beam. For B ≠0, the X_0 level splits according to the relevant spin multiplicity, L (L=3, 4, and 9, respectively for the S=1 TE; PP composed of two S=½ polarons; and a pair of TEs). Consequently, through specific spin-mixing processes, the spin content of each sublevel N_{ss}, its decay rate k, and thus PA, all become B-dependent. Figure 2.4 shows a typical PA spectrum and MPA (B) response of a film of Deuterated DOOPPV.

2.4 Doping-induced Absorption (DIA)

CW PA spectrum reveals the long-lived species in the film. But, whether the particular PA band is due to polarons may be easily identified by DIA measurement. This is essentially absorption measurement where the sample is doped with the strong dopants to induce charges on the polymer chains. The difference in absorption before and after doping forms a band at the absorption peak of the induced charges.

$$DIA = \frac{OD_{doped} - OD_{undoped}}{OD_{undoped}} \tag{2.9}$$

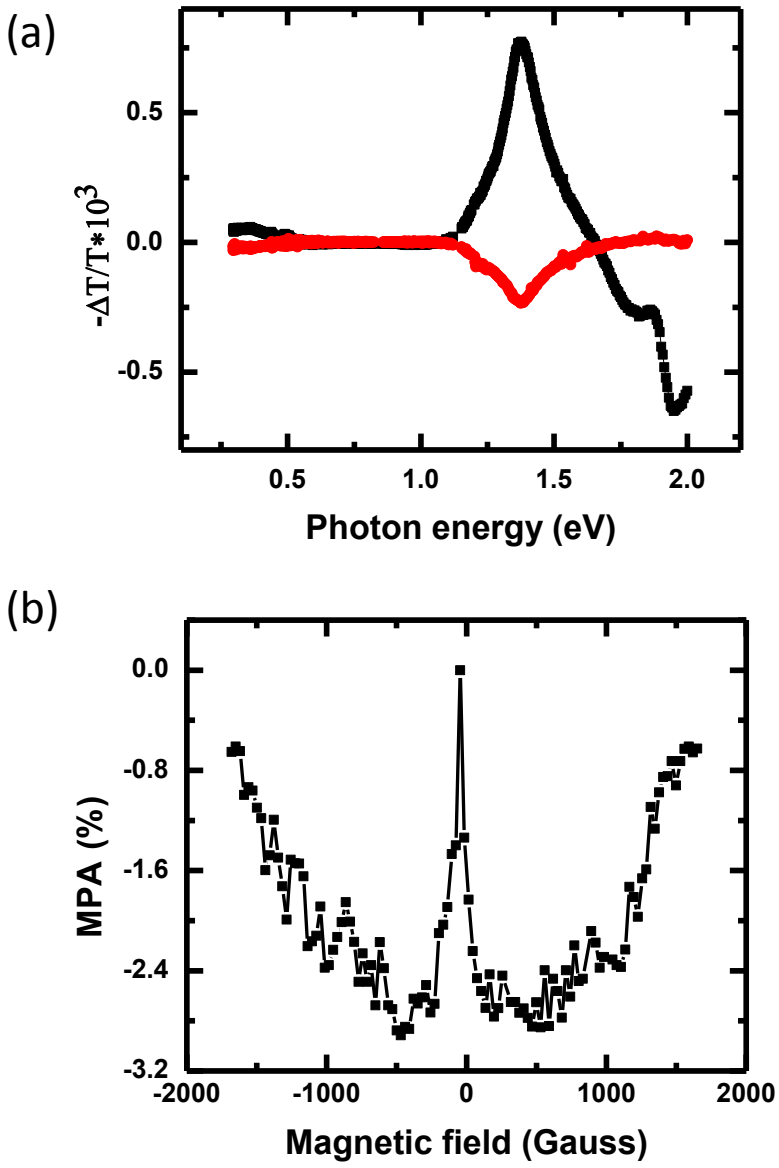

Figure 2.4. Photo-induced absorption in a polymer. (a) PA and (b) MPA at 1.4 eV band of Deuterated-DOOPPV film measured at low temperature.

The same instrument and method as in linear absorption are used for DIA measurement. We used two different kinds of dopants; these are iodine and $HAuCl_4$. In the case of iodine doping, the film is exposed to iodine vapor for ~1min and absorption is measured before and after doping. We used iodine doping in P3HT and PTB7 films. In the case of $HAuCl_4$ doping, $HAuCl_4$ is first dissolved in acetonitrile at 0.01M concentration and stirred overnight to mix uniformly. The film is then dipped in the solution for ~1min and the absorption is measured. Both iodine and $HAuCl_4$ serve as p-type dopant generating positive polarons in the film. The same spectrum as obtained when transmission with and without doping is measured is formed by photogenerated polarons in the PA setup. Figure 2.5 shows the doping-induced absorption of a PDTP- DFBT polymer film where the two polaron bands P_1 at 0.4 eV and P_2 at 1.2 eV are observed. The absorption in the lower energy (<0.5 eV) is measured with a FTIR spectrometer and normalized to match with the absorption data at high energy, which is measured using the CARY spectrometer.

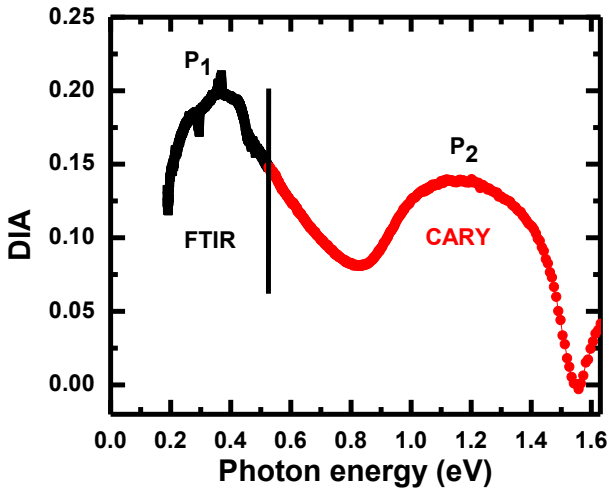

Figure 2.5. Doping-induced absorption (DIA) of PDTP-DFBT polymer. Red line is obtained using the CARY spectrometer, whereas the black line is obtained using the FTIR spectrometer.

2.5 Photoluminescence Quantum Efficiency (PLQE)

Photoluminescence quantum efficiency (PLQE) is the ratio of the number of emitted photons to the number of absorbed photons. In contrast to the PL measurement, where we get the emission spectrum, we determine the emission efficiency through PLQE measurement. In this type of measurement, by using a special instrument called an 'integrated sphere' (IS), we can collect all the emission from the sample and calculate PLQE. The IS contains three windows: one for the laser entrance, a second window for the sample, and a third window for the detector, as shown in Figure 2.6. A modulated laser travels through the first window into the IS and the light signal is monitored using the detector placed in the third window. Four categories of data are recorded by the lock in amplifier: (i) reflected laser intensity inside the IS when no sample is placed, I_L; (ii) reflected laser intensity with the appropriate filter which is later used to collect the PL emission, $I_{L,filter}$; (iii) PL intensity when a sample is placed inside in the path of the laser, I_{PL}; and (iv) scattered PL intensity when the sample is placed inside, but not in the laser

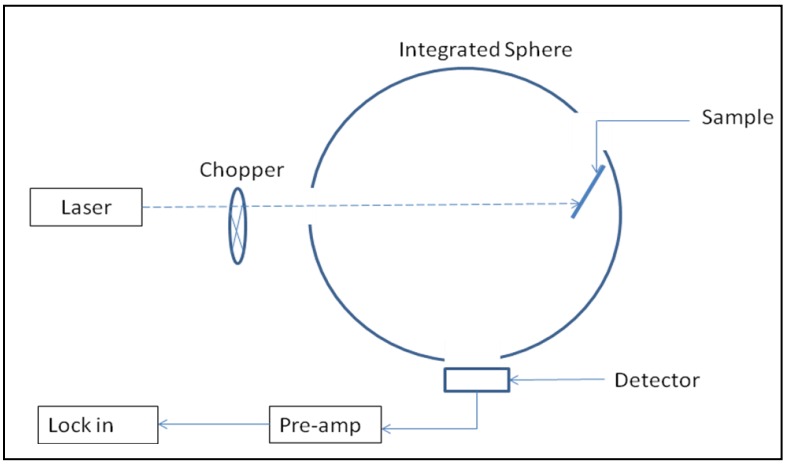

Figure 2.6. PLQE experimental setup using an integrated sphere.

path, $I_{PL,corr}$. PL peak energy(E_{PL}) and the optical density (OD) are measured prior to making the calculation. PLQE is calculated using the following formula,

$$PLQE = \frac{I_{PL} - (R+T)(I_{PL,corr} - I_{L,filter})}{\big((1-(R+T)\big)I_L} \frac{D_L}{D_{PL}} \frac{S_L}{S_{PL}} \frac{E_L}{E_{PL}} \frac{1}{T_F(PL)} \tag{2.10}$$

where R= substrate reflectivity; T = 10^{-OD} = transmittance of the sample; T_F(PL) is the filter transmission coefficient at PL peak; D_L,D_{PL},S_L,S_{PL} are the sensitivity of the detector and the sphere at the laser energy(E_L) and the PL energy(E_{PL}), respectively. ($I_{PL,corr}$-$I_{L,filter}$) is introduced to eliminate contribution to the collect light emission by additional photons that excite the sample indirectly through the reflection from the IS wall. If the lifetime of the singlet exciton, τ_{exc} is known along with PLQE, then the radiative lifetime of the singlet exciton can be calculated by using the following relation,

$$\tau_{rad} = \frac{\tau_{exc}}{PLQE} \tag{2.11}$$

and is usually of the order of one nanosecond.

2.6 Electroabsorption (EA)

In electroabsorption, an electric field is applied to the sample and the change in transmission is measured using the tungsten lamp for the visible region and the xenon lamp in the UV region. Additional energy states, which are not unraveled in the linear absorption measurement because of optical selection rules, can be observed in the EA measurement since the electric field, F, introduces a symmetry breaking that relaxes the optical transition restrictions. The external electric field perturbs the wavefunction and associated energies which are given by

$$\psi_j = a\left\{\psi_j^0 + \sum \frac{\langle\psi_l^0 \left|\vec{\mu}_{ij}.\vec{F}\right|\psi_j^0\rangle}{E_j^0 - E_l^0}\ \psi_l^0\right\} \tag{2.12}$$

$$\Delta E_j = \sum \frac{|\,\langle\psi_l^0|\vec{\mu}_{ij}.\vec{F}|\psi_j^0\rangle\,|^2}{E_j^0 - E_l^0}\ \psi_l^0 = p_j\frac{F^2}{2} \tag{2.13}$$

where ψ_j^0 is the zero-field wavefunction, $\vec{\mu}_{ij}$ is the transition dipole moment and p_j is the polarizability of the states resulting from the nonvanishing dipole matrix elements. In the case of π-conjugated polymers, the electric field-induced change in absorption (-ΔT/T) is proportional to the nonlinear susceptibility $\chi^{(3)}$ [44], and the EA spectrum is usually proportional to the derivative of the absorption spectrum with respect to the photon energy (dα/dE).

The experiment consists of applying an electric field to an interdigitated gold electrodes as shown in Figure 2.7(a). A 0.5 nm titanium and 150 nm of gold is RF sputtered on top of a 1 inch diameter sapphire substrate, and lithographically patterned with a gap of 40μm. A very thin polymer film is prepared by drop-casting, and the sample is mounted inside a cryostat equipped with electrical connections. A schematic of the setup is shown in Figure 2.7(b), which is in fact a modified version of the PA setup. Here, the electric field is used instead of the laser to access the excited states. An electric field of order of ~10^5V/cm is applied on the sample by using an AC field of 200-300V. The AC signal is generated using the signal generator at 500 Hz, and fed through the step up transformer whose output is connected to the sample electrode. AC modulation frequency is used as the reference to the lock in amplifier and detected at the second harmonic frequency since the conjugated polymer has mirror symmetry, and therefore the EA ~ V^2. Thus, they respond to a sinusoidal field of frequency f with an EA signals at 2f,

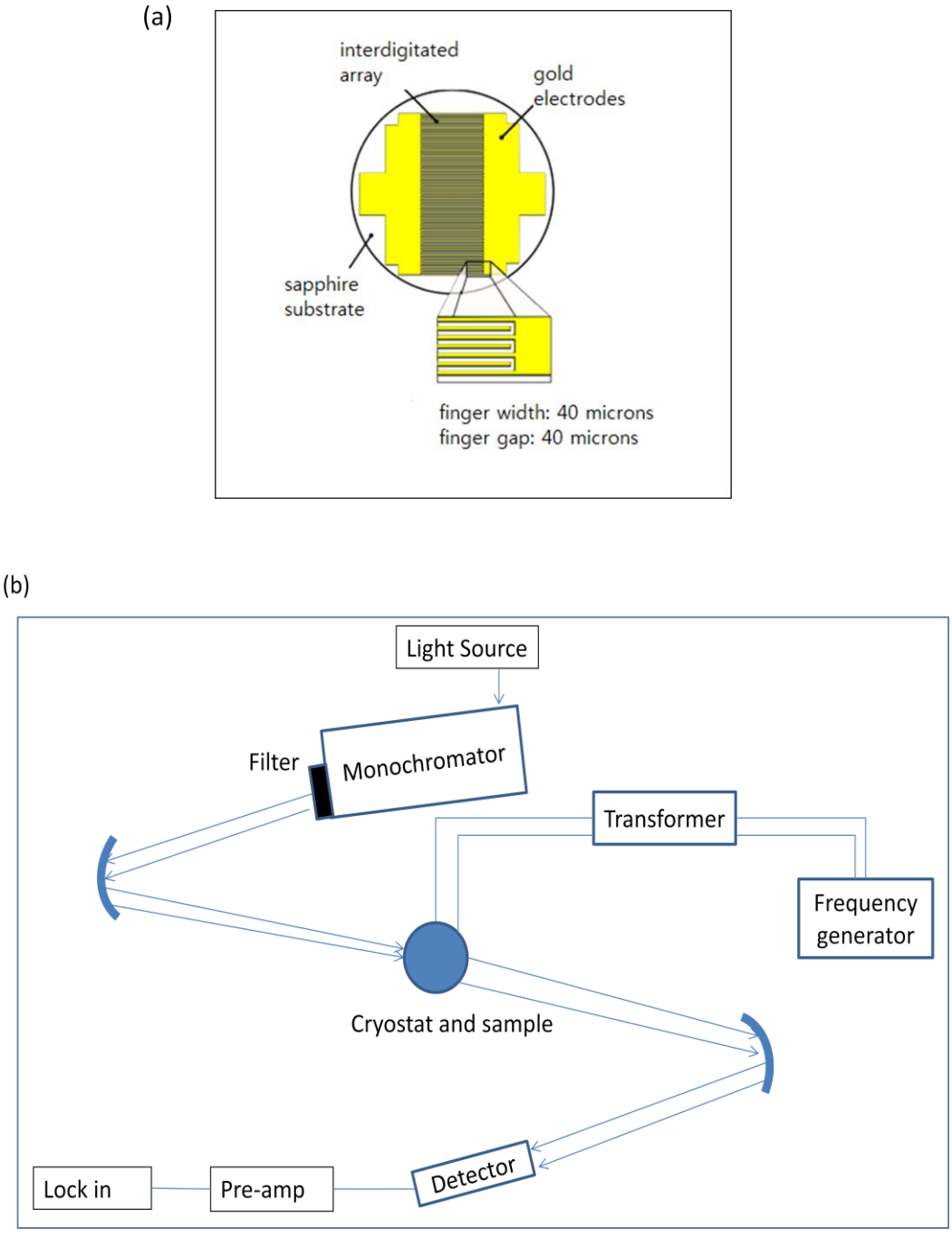

Figure 2.7. EA measurement. (a) EA susbstrate; (b) Experimental setup.

where the fundamental frequency is very much suppressed.

2.7 Optically-detected Magnetic Resonance (ODMR)

2.7.1 Theory

Electron spin resonance (ESR) uses microwave absorption to detect the spin character of the spin carriers on the sample. However, spin density in π-conjugated polymer is very low, so it is not the most effective technique. In ODMR, rather than observing the change in microwave absorption, in the order of ~meV, the change in the excited state transitions, in the order of ~eV, is monitored. Since most of the π-conjugated polymer has spin 0 at ground state, it is advantageous to detect the long-lived photoexcitations, which have spin 1 (triplet exciton) or ½ (polaron). The interaction between the electronic magnetic moment, $\vec{\mu}$, and the applied magnetic field, $\vec{B}$, is given by,

$$H_{zeeman} = -\vec{\mu}.\vec{B} \tag{2.14}$$

where,

$$\vec{\mu} = g\frac{e}{2m}\vec{S} = \gamma\vec{S} = g\beta\vec{S}/\hbar \tag{2.15}$$

Here, g is the lande g factor, γ is the gyromagnetic ratio, and β is the Bohr magneton. In the presence of the magnetic field, the spin energy levels split according to the spin projection values (m_s). Microwaves induce spin flip by promoting the electron to higher energy level if the photon energy is equal to the Zeeman splitting,

$$\hbar\omega = g\beta m_s B \tag{2.16}$$

Typically, for ~3GHz microwaves and g factor of ~2, B =1000 gauss is in resonance with the transition between m_s=1/2 to m_s=-1/2. In general, in addition to the Zeeman

interaction, hyperfine interaction, spin-spin interaction, spin-orbit interaction, etc. need be taken into account if they are relevant to the system under consideration. Basically, microwaves redistribute the population of the spin excited state, balancing the antiparallel spin density to the parallel spin density if they are initially unequal. In π-conjugated polymers, radiative decay from the antiparallel e-h polarons occurs much more quickly than the decay from the parallel e-h spin configuration. The population of the parallel spin is lower if the system starts with geminate pair. However, the population of the excited states may be the other way around, namely triplets if the system starts from the triplet states (distant pair model). Here, we have to note that the ground state population is governed by the Boltzman distribution, whereas the excited states population mainly depends on the generation and the recombination rate for different spin sublevels, because it is not in thermal equilibrium. It is for this reason that ODMR is usually measured at a low temperature, where the equilibrium thermalization is suppressed due to longer spin-lattice relaxation time.

In the case of triplet exciton (spin=1), it is necessary to consider the spin-spin interaction, for which Hamiltonian is given by,

$$H_{ss} = \vec{S}.\boldsymbol{D}.\vec{S} \tag{2.17}$$

where **D** is the zero field splitting (ZFS) tensor which is calculated from the magnetic dipole-dipole interaction of the spins, and $\vec{S}$ is the spin vector. For a pair of interacting spin particles separated by distance r,

$$H_{ss} = \left(\frac{g\beta}{\hbar}\right)^2 \left[\frac{\vec{S}_1.\vec{S}_2}{r^3} - 3\frac{(\vec{r}.\vec{S}_1)(\vec{r}.\vec{S}_2)}{r^5}\right] \tag{2.18}$$

After expanding the above Eq. (2.18) into the components of the total spin angular momentum S_x, S_y, and S_z and comparing with Eq. (2.17), we get,

$$\boldsymbol{D} = \begin{bmatrix} r^2 - 3x^2 & -3xy & -3zx \\ -3xy & r^2 - 3y^2 & -3yz \\ -3zx & -3yz & r^2 - 3z^2 \end{bmatrix} \tag{2.19}$$

Diagonalizing **D** gives the only two independent parameters named as D and E since the trace of this matrix is zero. Under these conditions, H_{ss} can be written as,

$$H_{ss} = D\left\{S_Z^2 - \frac{1}{3}S(S+1)\right\} + E(S_X^2 - S_Y^2) \tag{2.20}$$

Here, S is the modified spin vector on the basis that diagonalizes **D**. In this system, the triplet levels, X, Y, and Z are related to D and E by,

$$D = -\frac{3Z}{2} \;\; and \; E = \frac{Y - X}{2} \tag{2.21}$$

where *X*, *Y*, and *Z* are the spin 1 energy levels. The possible transitions in the triplet spin manifold are two, namely for Δm_s=1 (full field) and one transition for Δm_s=2 (half field) as shown in Figure 2.8(a). At magnetic resonance, the transitions form a triplet powder pattern, the average of all possible orientations of the principal axis of D tensor. Theoretical calculations [45] show the specific form of the resonance pattern predicting divergences, steps and the shoulders which can be used to calculate the values of D and E. We can, in principle predict the spin character of the excited state species just by looking at the presence (spin 1) or absence (spin ½) of the half field.

There are two techniques of doing ODMR: (1) detection of changes in PL, PLDMR, and (2) detection of changes in photo-induced absorption, PADMR. If the system has very strong luminescence emission, then it is convenient to measure PLDMR.

In PLDMR, excited state spin is flipped by the microwave photons, thus balancing the population distribution between parallel and antiparallel states, N_p and N_{AP}. PL intensity without (OFF) and with (ON) microwave resonance is given by

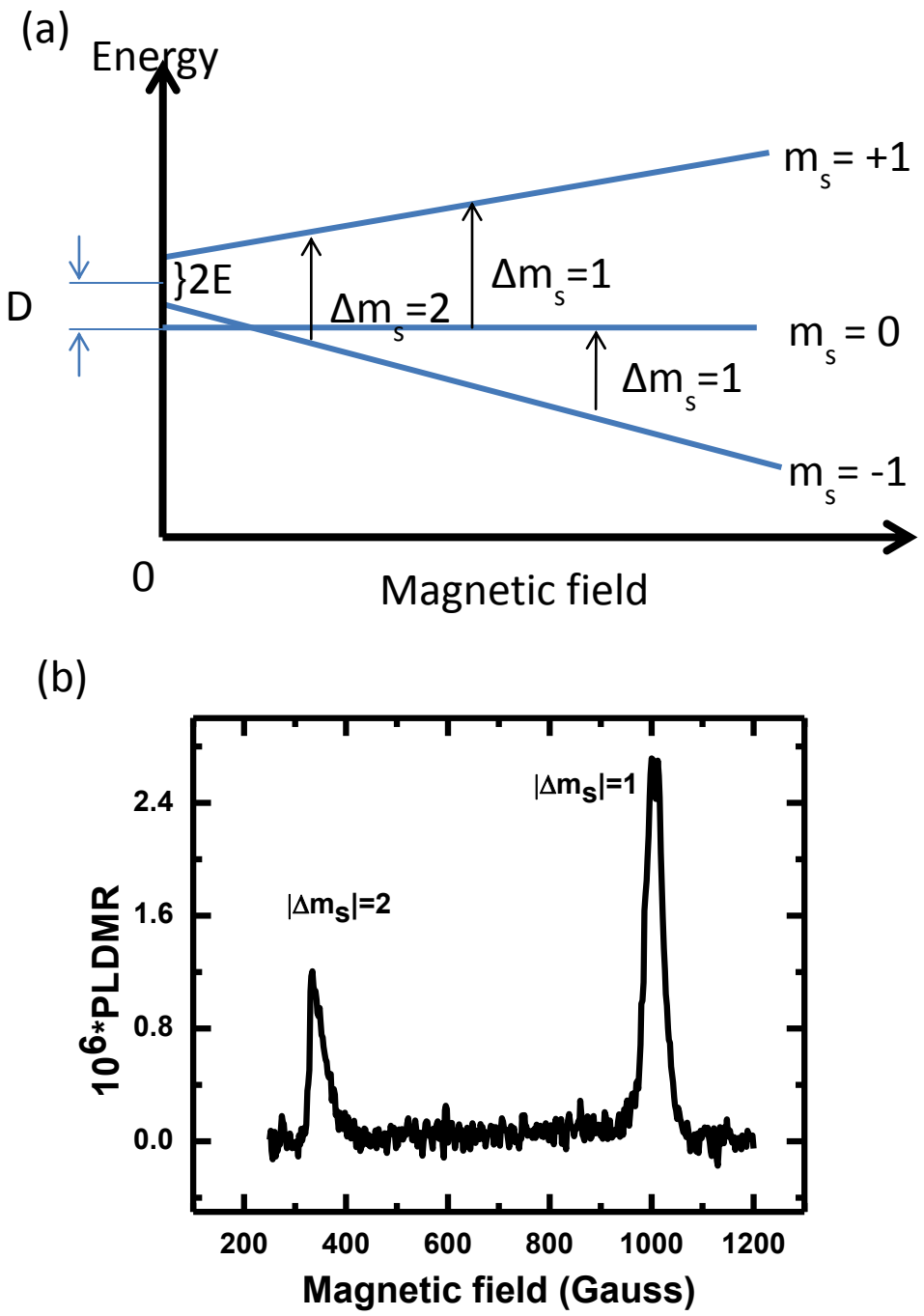

Figure 2.8. Triplet detection in ODMR. (a) Triplet splitting under the influence of a magnetic field and the associated spin 1 transitions. (b) PLDMR of MEHPPV showing spin ½ and 'half field' spin 1 resonances.

$$I_{OFF} = R_P^0 N_P + R_{AP}^0 N_{AP} \tag{2.22}$$

$$I_{ON} = R_P^0 \widetilde{N}_P + R_{AP}^0 \widetilde{N}_{AP} \tag{2.23}$$

which gives the change in PL emission as,

$$\frac{\delta I}{I} = \frac{I_{ON} - I_{OFF}}{I_{OFF}} = -\frac{R_{AP} R_P (N_{AP} - N_P)\left(\frac{R_{AP}^0}{R_{AP}} - \frac{R_P^0}{R_P}\right)}{(R_{AP} + R_P) I} \tag{2.24}$$

where R is the recombination rate, R^0 is the radiative recombination rate, and the tilde above N is the population density under microwave resonance conditions. A typical PLDMR transition of MEHPPV film is shown in Figure 2.8(b).

In PADMR, the change in excited states density, δN, due to magnetic resonance is given by,

$$\delta N = \widetilde{N} - N = \left(\widetilde{N}_P + \widetilde{N}_{AP}\right) - (N_P + N_{AP}) \tag{2.25}$$

Under microwave resonance, the number of parallel and antiparallel spins is equal. This will give,

$$\frac{\delta N}{N} = \frac{N_{AP} - N_P}{N} \frac{R_{AP} - R_P}{R_{AP} + R_P} \tag{2.26}$$

For the geminate recombination, the system starts with $N_P = 0$ and $N_{AP} = N$, and the Eq. (2.26) becomes,

$$\frac{\delta N}{N} = \frac{R_{AP} - R_P}{R_{AP} + R_P} > 0 \tag{2.27}$$

For the distant pair recombination, all the spin ½ pairs are randomly distributed, so, assuming, $G_{AP} = G_P$, we get,

$$\frac{\delta N}{N} = -\left(\frac{R_{AP} - R_P}{R_{AP} + R_P}\right)^2 < 0 \tag{2.28}$$

Thus, the sign of the PADMR signal gives the type of the recombination spin species.

2.7.2 Experimental Setup

The experimental setup for ODMR is shown in Figure 2.9; it is another modified version of the PA setup. The sample is mounted on the 3GHz coaxial microwave cavity, inside the liquid Helium cooled cryostat, between the poles of the superconducting magnet. The microwave cavity size has an inner radius of 0.627cm, outer radius of 2.2cm, and length of 9.9cm. The maximum power of the microwave is 100 mW, which produces electric field of 90V/cm and a magnetic field of 0.3G at the sample. The cryostat has an outer jacket for the vacuum to provide insulation, which is followed by Nitrogen, Helium, and the sample chamber into the interior. The temperature of the

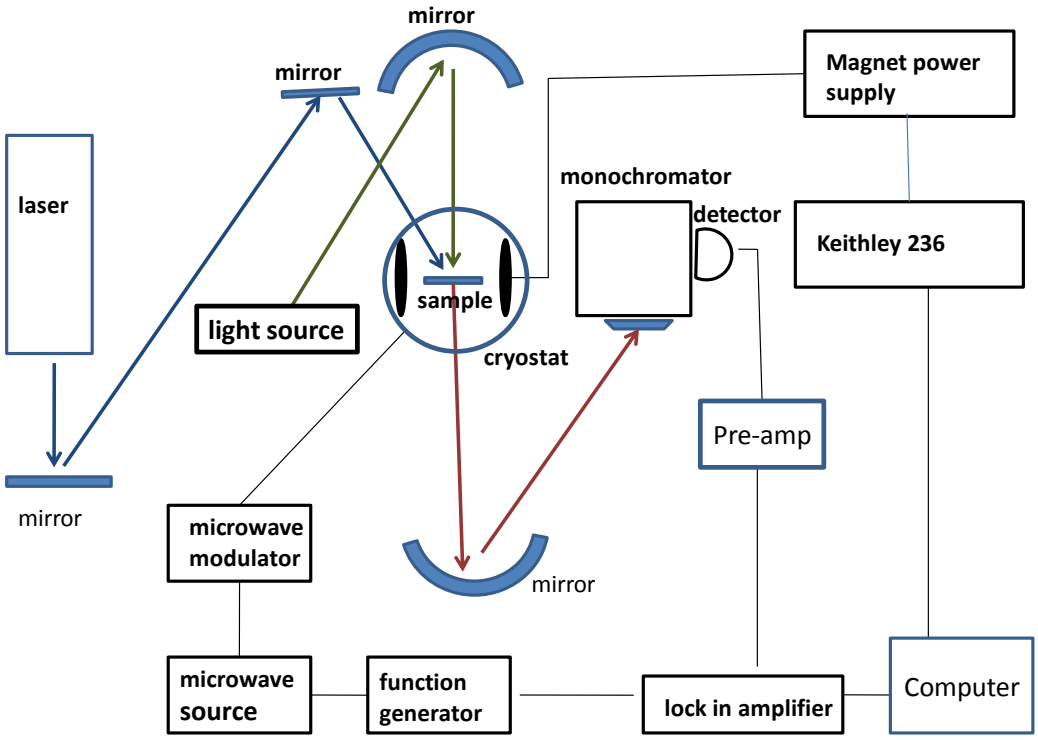

Figure 2.9. ODMR experimental setup.

sample chamber is controlled by the flow of Helium through the needle valve and the superconducting magnet is dipped into Helium in the Helium chamber. The superconducting magnet is driven by the dc supply by the keithley 236 voltage source, which is connected to AMI 400A programmer. The microwave is generated by the HP616B UHF high frequency generator, amplified, and then modulated by the pulse modulator, which is controlled by 200Hz square wave from a function generator. The sample is illuminated by the diode or CW Ar+ laser and probed by the tungsten lamp.

2.8 Device Fabrication

OPV and OLED devices are fabricated in the same way; the only difference is in the active layer of the organic semiconductor. The organic layer, usually a polymer or small molecule single layer for OLED and polymer/blend bulk heterojunction for the OPV, is sandwiched between two electrodes of the device. Indium Tin Oxide (ITO)-coated glass substrate with substrate resistivity 8-12 Ω/cm, purchased from Delta technologies, is used as the anode and the thermally evaporated Calcium and Aluminum is used as cathode. There are three main steps in fabricating the device; substrate cleaning, active layer deposition, and Cathode layer deposition. Before cleaning the ITO-coated glass, it is patterned in the 2mm or 1mm striped layer. Nail polish is used to cover the stripe and all other exposed portions are etched by immersing the substrate into 80% Hydrochloric acid and 20% water solution for 10-12 minutes. Then, the 75mmX25mm glass slab is diced to make 12.5mmX12.5mm pieces for each substrate. Substrates are ultrasonically cleaned with acetone, 2% micro-soap solution, de-ionized water and methanol for 10 minutes each. A thin layer—about 50nm thickness—of PEDOT:PSS is

spin-coated on the substrate which serves as the hole transport layer because its HOMO level lies between the ITO work function and the HOMO of the most of the polymer. The substrates are then transferred to the glove-box (<1 ppm oxygen) for the active layer deposition. The polymer and its blend are spin-coated on top of the substrate at different spin speed to vary the thickness. Small molecules such as Alq3 cannot be spin-coated as they are hard to dissolve in the solvent. Therefore, they are thermally evaporated inside the vacuum deposition system at high vacuum of 10^{-6} Torr. Polymers and the blend solution are prepared at different concentrations and with different solvents. The particular choice of the solvent or the concentration is experimentally optimized. After the active layer deposition, 25nm Calcium and 80nm Aluminum is thermally evaporated where Al serves as the capping layer to protect Ca from oxidization. Occasionally, the device is encapsulated with the microscope cover glass using the optically adhesive UV curable glue if the measurement needs to be performed in the air. Typical UV exposure time is ~45 seconds.

2.9 OPV Characterization

The OPV device is characterized by the I-V curve, which gives the useful parameters V_{oc}, J_{sc}, Fill Factor (FF), and PCE. For this purpose, the OPV device is illuminated by the simulated solar spectrum by using the xenon lamp and AM1.5 filter. The light intensity is calibrated to produce 100mW/cm^2 (P_{in}), appropriate to the solar intensity on the earth at sea level, using a calibrated silicon solar cell. Solar spectrum and the schematic of the experimental setup are shown in Figure 2.10. Device I-V characteristics are measured by the Keithley 236 Source-Measure unit under the

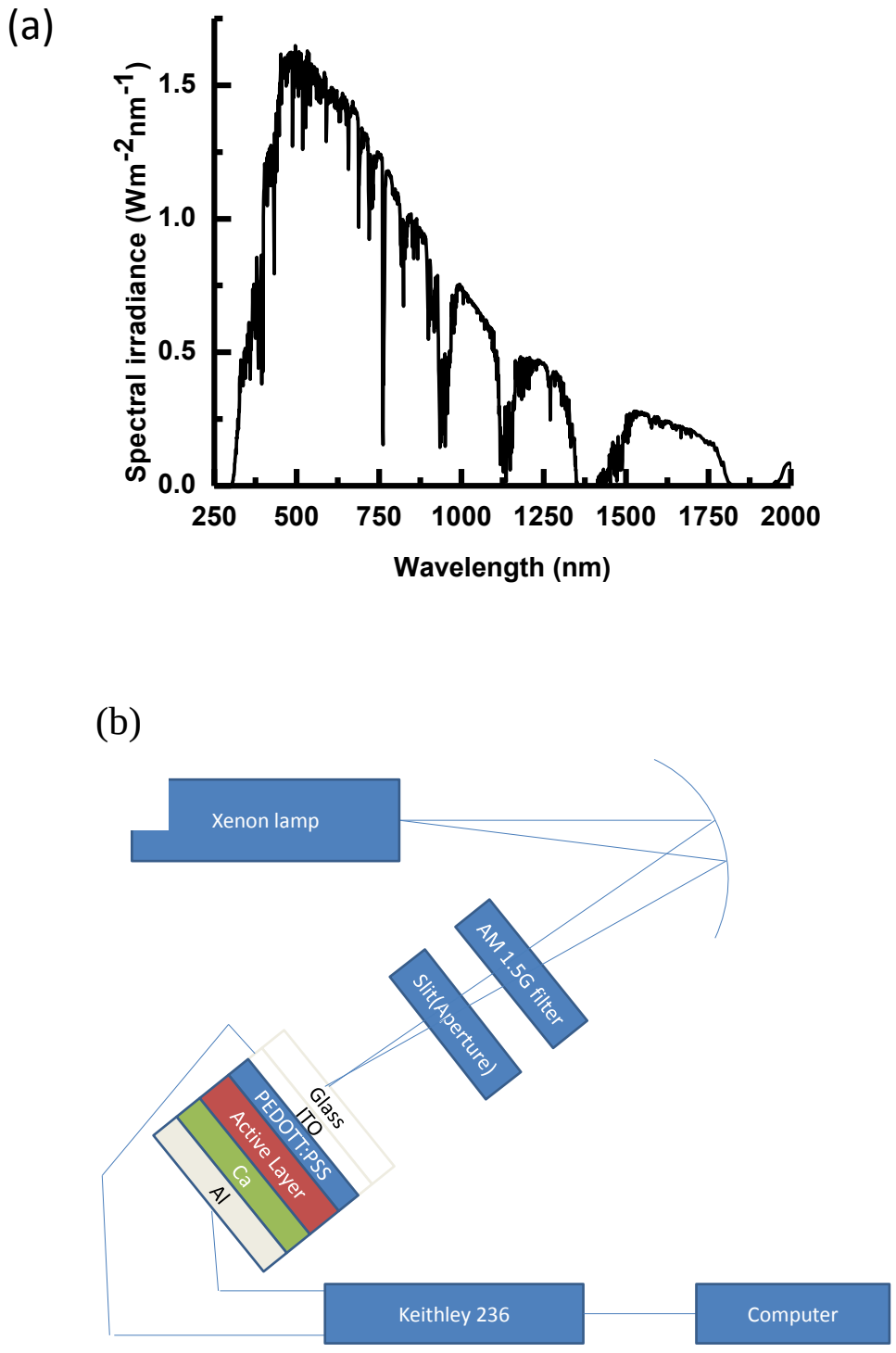

Figure 2.10. Organic photovoltaics. (a) Solar spectrum. (b) PCE measurement setup.

illumination. From the I-V, J_{sc} is calculated by dividing the zero-biased current with the device area, V_{oc} is the voltage at zero current and FF is the ratio of P_{max}, the maximum power obtained (shaded portion in Figure 2.11) to the maximum possible output power, i.e.,

$$FF = \frac{P_{max}}{J_{sc}V_{oc}} \tag{2.29}$$

Then, PCE(η) can be calculated as,

$$\eta = FF\frac{J_{sc}V_{oc}}{P_{in}} \tag{2.30}$$

2.10 OLED Characterization

In this thesis, OLEDs are characterized by the I-V dependence followed by MC and MEL. The device is mounted on the closed cycle He-cooled cryostat with proper electrical connection and the measurement is done both at room temperature and at low temperature, controlled by the temperature controller unit. Keithley 236 is used as the source to provide bias on the device, and a silicon photo-detector with the preamplifier, or the ocean optics spectrometer, is used to measure the electroluminescence. A typical I-V and EL-V characteristics of an OLED is described in Chapter 1. Magnetic field is applied using an electromagnet up to ~2000 Gauss, and the current for MC and the EL for MEL are scanned by sweeping the magnetic field in plane to the device. MC is defined as,

$$MC = \frac{I(B) - I(0)}{I(0)} \tag{2. 31}$$

And MEL is defined as,

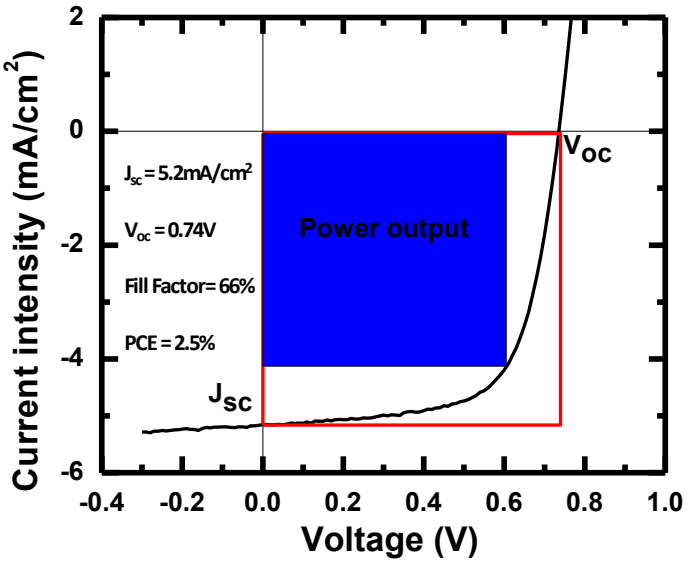

Figure 2.11. OPV I-V characteristics of H-DOOPPV/PCBM device.

$$MEL = \frac{EL(B) - EL(0)}{EL(0)} \tag{2. 32}$$

Typical MC and MEL response in MEHPPV device at 10K is shown in Figure 2.12. Full Width Half Maximum (FWHM) is believed to be dependent on the spin flip process caused by the hyperfine interaction or another intersystem crossing (ISC) mechanism in the polaron pair, excitons or exciton-polaron interaction. The hyperfine strength is typically <100G which is similar to observed FWHM in the MEL and MC response of the device.

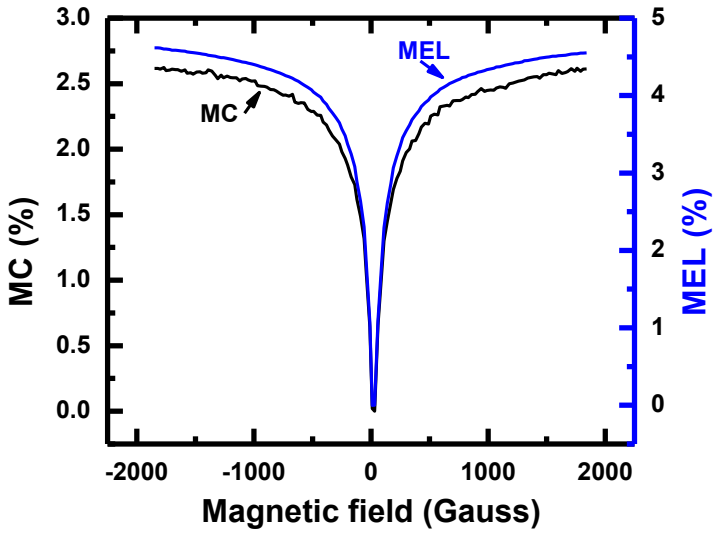

Figure 2.12. Typical MC (black) and MEL (blue) responses of an OLED.

CHAPTER 3

ORGANIC LIGHT EMITTING DIODES

3.1 Isotope Effect in the Spin Response of Aluminum Tris(8-hydroxyquinoline)-based Devices

3.1.1 Introduction

Aluminum tris(8-hydroxyquinoline) (Alq_3) [see molecular structure in Figure 3.1(a) inset] is a common active molecular layer used in organic light emitting devices (OLED), due to its efficient electro-luminescence (EL) emission and high electron mobility [25, 46, 47]. It is thus not surprising that magnetic field effects (MFE) in Alq_3-based OLED devices such as magneto-electroluminescence (MEL) and magneto-conductance (MC) have been extensively studied in the last few years [35, 39, 48-52]. As a result, several basic models were originally proposed to explain the obtained magnetic-field effect response, MFE(*B*). Basically, all models agree that the underlying mechanism for the MFE is the magnetic field dependence of spin sublevel mixing; but there is no agreement as to the basic excitation where the spin mixing occurs. The competing models include: (i) spin mixing in oppositely charged polaron-pairs (PP) and in pairs of same-charge polarons (or bipolarons, BP) by the hyperfine interaction (HFI) [35, 37, 49, 53]; (ii) spin mixing within triplet-triplet annihilation (TTA) process [50]; and (iii) spin mixing during the process of triplet exciton quenching by spin ½ charge

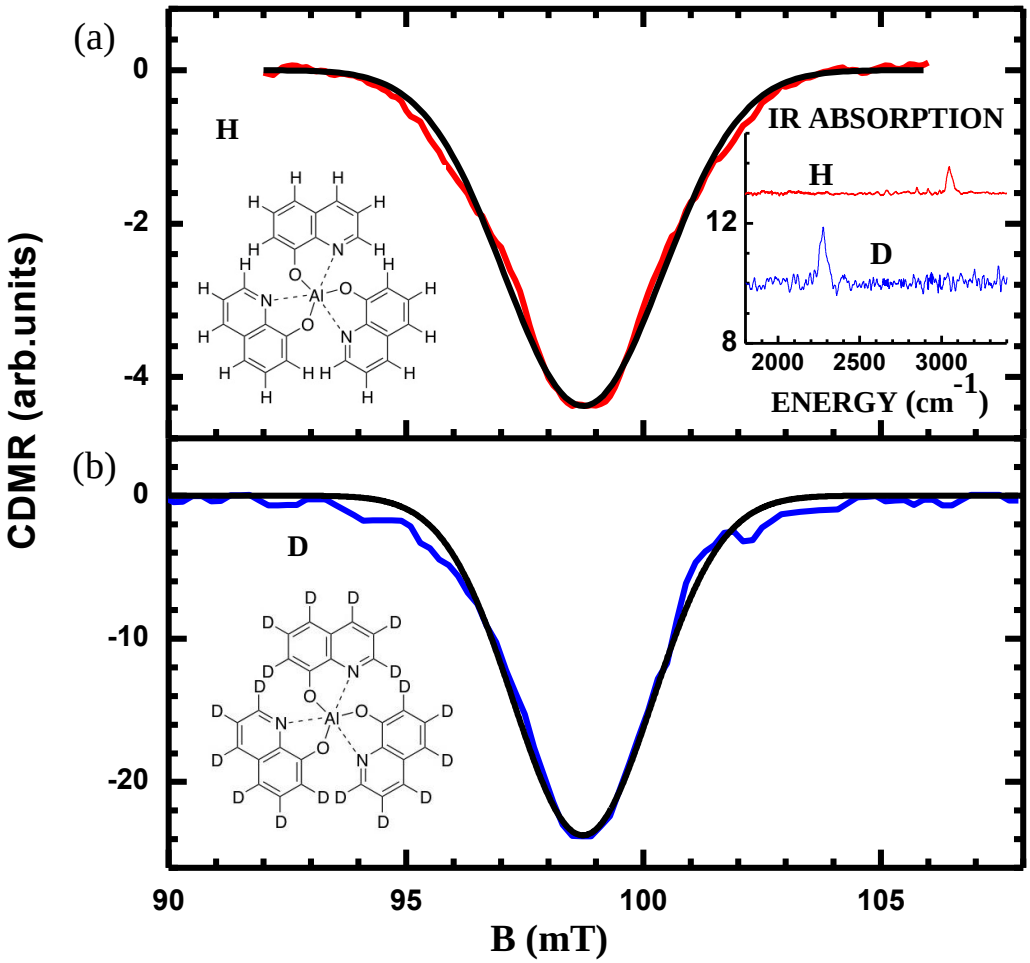

Figure 3.1. Spin ½ CDMR of (a) H_{18}-Alq_3 (red line) and (b) D_{18}-Alq_3 (blue line) measured at ~3 GHz and 10 K; the FWHM are 3.94 and 3.46 mT, respectively. The black lines are fits using inhomogeneous broadened (Gaussian profile, FWHM=3.4 mT) hyperfine split resonance, with a_{HF}=3 mT and 0.46 mT, respectively, for H-Alq_3 and D-Alq_3. The molecules' chemical structures are shown in the left insets. The right inset in (a) shows the molecules' infra-red absorption spectra, where a red-shifted C-H stretching mode occurs upon deuteration, namely ν_{CH}=3050 cm^{-1} and ν_{DH}=2276 cm^{-1}; i.e. within 2% of the square root C-D/C-H reduced mass ratio.

polarons [39]. Importantly, the HFI proposed models should differ substantially from the other models in the response to isotope exchange in the Alq_3 molecule active layer, where all hydrogen atoms (nuclear spin I_H=½, nuclear g-factor g_H=5.586) are exchanged by deuterium atoms (I_D=1, g_D/g_H=0.154). This should happen since the HFI constant, a_{HF}, scales with the nuclear g-factor [54], whereas the other proposed interactions are isotope insensitive. Consequently, the isotope exchange effect on the MFE(*B*) response of Alq_3-based OLED was recently studied and claimed to be minimal, since both MC(*B*) and MEL(B) responses appeared to be isotope insensitive [51]. It was thus concluded that the MFE in Alq_3-based OLED is not dominated by PP or BP species since the HFI does not play an important role in determining the obtained MC(*B*) and MEL(*B*) responses. These measurements and conclusions are surprising, because similar MFE measurements in devices based on a common π-conjugated polymer, namely poly(dioctyloxy) phenyl vinylene (DOO-PPV), have shown a substantial isotope effect [43, 55]. It is thus important to investigate in more detail the influence of the isotope exchange on the MFE and magneto-transport in Alq_3-based devices in order to identify the underlying spin-exchange mechanisms.

In this work, we present a detailed study of the MFE response and magneto-transport in protonated (H-) and deuterated (D-) Alq_3-based OLED and spin-related devices. These studies include spin ½ conductivity-detected magnetic resonance (CDMR) in organic diodes, magneto-resistance (MR_{SV}) in organic spin valves (OSV), and MC and MEL responses in OLED devices. We found that the spin ½ CDMR is isotope sensitive. It shows a narrower resonant line in D-Alq_3 compared to H-Alq_3 devices, and therefore, the polaron excitation in Alq_3 is definitely influenced by the HFI. This indicates that spin-

related effects based on polaron excitations should be isotope sensitive here. Indeed, we measured superior MR_{SV} response in D-Alq_3 OSV devices, which indicates larger spin diffusion length due to the reduced HFI of the deuterium isotope. Moreover, a clear sizable isotope-dependent MEL(*B*) response in OLED was also observed at low fields (*B*<~20 mT). This shows that HFI-induced spin mixing of polaron-pairs spin sublevels plays a crucial role also in determining the MEL response in Alq_3-based OLED. However the MC(*B*) response at low fields was found to be less sensitive to the isotope exchange. In addition, at high fields both MEL(*B*) and MC(*B*) are isotope insensitive, and do not show the expected HFI-related saturation up to *B*~250 mT. These puzzling MFE characteristic properties can be understood taking into consideration that in addition to the HFI in PP (or BP) species, other spin-mixing mechanisms also participate in determining the MFE in Alq_3 diodes. We propose here that an isotope-independent collision of spin ½ polarons with triplet-state species (e.g. PP, BP or TE) is the main spin-mixing mechanism responsible for the low field MC(*B*) response.

3.1.2 Experimental

The active layers in our spin-related device studies are the two Alq_3 isotopes: $H_{18}Alq_3$ and $D_{18}Alq_3$, where all the hydrogen atoms in H-Alq_3 are replaced by deuterium [56]. Figure 3.1(a) and (b) (left insets) show the Alq_3 molecular structure and the H (D) atoms positions. We used both NMR spectroscopy and infrared (IR) absorption to verify that all hydrogen atoms were replaced by deuterium atoms in the D-Alq_3 molecules. The IR absorption spectrum of the two Alq_3 isotopes in the range of the C-H stretching vibration, ν_{CH}, shows a deuteration-related shift according to the expected mass ratio

(Figure 3.1(a), right inset). We measured ν_{CH}=3050 cm^{-1} and ν_{DH}=2276 cm^{-1}; their ratio is within 2% of the square root C-D/C-H reduced mass ratio. In particular, the lack of an absorption band at 3050 cm^{-1} in the IR absorption spectrum of D-Alq_3 indicates that there is no hydrogen atoms present in this molecule.

The OLED devices were fabricated using glass substrates coated with 40 nm of indium-tin-oxide (ITO) that were purchased from Delta Technologies. The conducting polymer poly(3,4-ethylenedioxythiophene)-poly(styrenesulfonate) (PEDOT) that was purchased from H C Starck was spin-coated onto the ITO used as the anode. The Alq_3 (sublimed, HW Sands Corp.) layer was then thermally evaporated onto the bottom electrode. Subsequently, a Ca cathode with an Al capping layer was deposited by thermal evaporation onto of the Alq_3 thin film. The complete device structure configuration was ITO/PEDOT(30nm)/Alq_3(70nm)/Ca(20nm)/Al(50nm) having an active area of ~2x2 mm^2 for all devices.

The OLED devices for the CDMR measurements were placed in a S-band (~3 GHz) microwave (MW) cavity in a cryostat at 10K equipped with MW throughput cables; the MW radiation was provided by a Gunn diode that delivered up to P_{MW} ~0.1 W power. The cryostat was placed inside a liquid He cooled superconducting coil that provided magnetic fields up to 3 Tesla, applied perpendicular to the device substrate. P_{MW} was modulated at frequency f~200 Hz and the changes ΔI in the current I were monitored using a lock-in amplifier at f. The magnetic field, B, was swept while monitoring ΔI. Resonance condition for spin ½ occurs when the MW photon energy is equal to the energy difference between the two Zeeman split spin sublevels at B~0.1 T for $g \approx 2$. To compare the resonance profile of the two Alq_3 isotopes, we measured $\Delta I(B)/I$

under identical conditions such as device structure, applied voltage, temperature, and microwave power.

For the MEL and MC measurements in the OLED, the devices were transferred to an optical cryostat with variable temperature that was placed in between the two pole pieces of an electromagnet that produced B in the range ±0.3 T with up to 10^{-5} T resolution; in all measurements, *B* was determined by a calibrated magnetometer. The devices were driven at constant voltage, *V*, or constant current, *I*, using a Keithley 236 apparatus, whereas the EL intensity was measured by a Si photo-detector, while sweeping *B* in both positive and negative directions.

The OSV devices were fabricated using the half-metal $La_{0.67}Sr_{0.33}MnO_3$ (LSMO) as the FM anode. The Alq_3, Co and Al layers were successively thermally evaporated onto the LSMO electrode similar to the OLED fabrication described above. The OSV device structure was LSMO(200nm)/Alq_3(40nm)/Co(6nm)/Al(50nm) with an active area typically of ~0.2x0.4 mm^2. All thermal evaporations were done in a high vacuum environment ($5x10^{-7}$ mbar). The thickness of the films was measured using thickness profilometry methods (KLA Tencor). The OSV magneto-resistance response MR_{SV} was measured in a closed-cycle refrigerator at temperatures, *T*, in the range 10-300 K using the 'four probe' method in a constant current mode using a Keithley 236 apparatus, while varying the external in-plane magnetic field. The magnetization properties of the FM electrodes were measured by the magneto-optic Kerr effect (MOKE); from these measurements, we determined typical low temperature coercive fields of the unassembled electrodes as B_{c1}~4.5 mT and B_{c2}~15 mT, for the LSMO and Co electrodes, respectively.

3.1.3 Results and Analysis

3.1.3.1 Conductivity-detected Magnetic Resonance

The CDMR spectra of H- and D-Alq_3 OLED devices (Figure 3.1(a) and 3.1(b), respectively) are negative under magnetic resonance conditions. CDMR in π-conjugated systems measures changes in the polaron pair (PP) density [57] under resonance conditions. Therefore, the CDMR spectra in Figure 3.1 show the effect of isotope exchange on the PP spin density. The resonance line of H-Alq_3 appears to be inhomogeneously broadened: the full width at half maximum (FWHM) is ~3.94 mT for the H-Alq_3 and 3.46 mT for the D-Alq_3, substantially larger than the FWHM of <2 mT obtained in spin ½ CDMR of devices based on the DOO-PPV polymer [55]. Using the same model presented earlier in reference [55], we show fits (black solid lines in Figure 3.1) to the measured CDMR line shapes of the H- and D-Alq_3 devices, using an inhomogeneously broadened hyperfine split resonance line with a_{HF}=3 and 0.46 mT, respectively. The smaller FWHM measured for the D-Alq_3 device is a strong indication that the HFI indeed plays an important role in the PP spin dynamics in this molecule.

3.1.3.2 Magneto-resistance in Organic Spin-Valves

Further evidence for the HFI importance for spin ½ polarons in Alq_3 is revealed in the magneto-resistance MR_{SV} measurements in OSV devices based on D- and H-Alq_3 interlayer (Figure 3.2). It is seen that MR_{SV} of D-Alq_3 (Figure 3.2(b)) is three times larger than that of H-Alq_3 (Figure 3.2(a)). The superior MR response of the D-Alq_3 OSV is maintained at various voltages (Figure 3.2(c)), showing that the spin diffusion length, λ_S, in the deuterated spin valve is substantially larger than that in the hydrogenated device. In

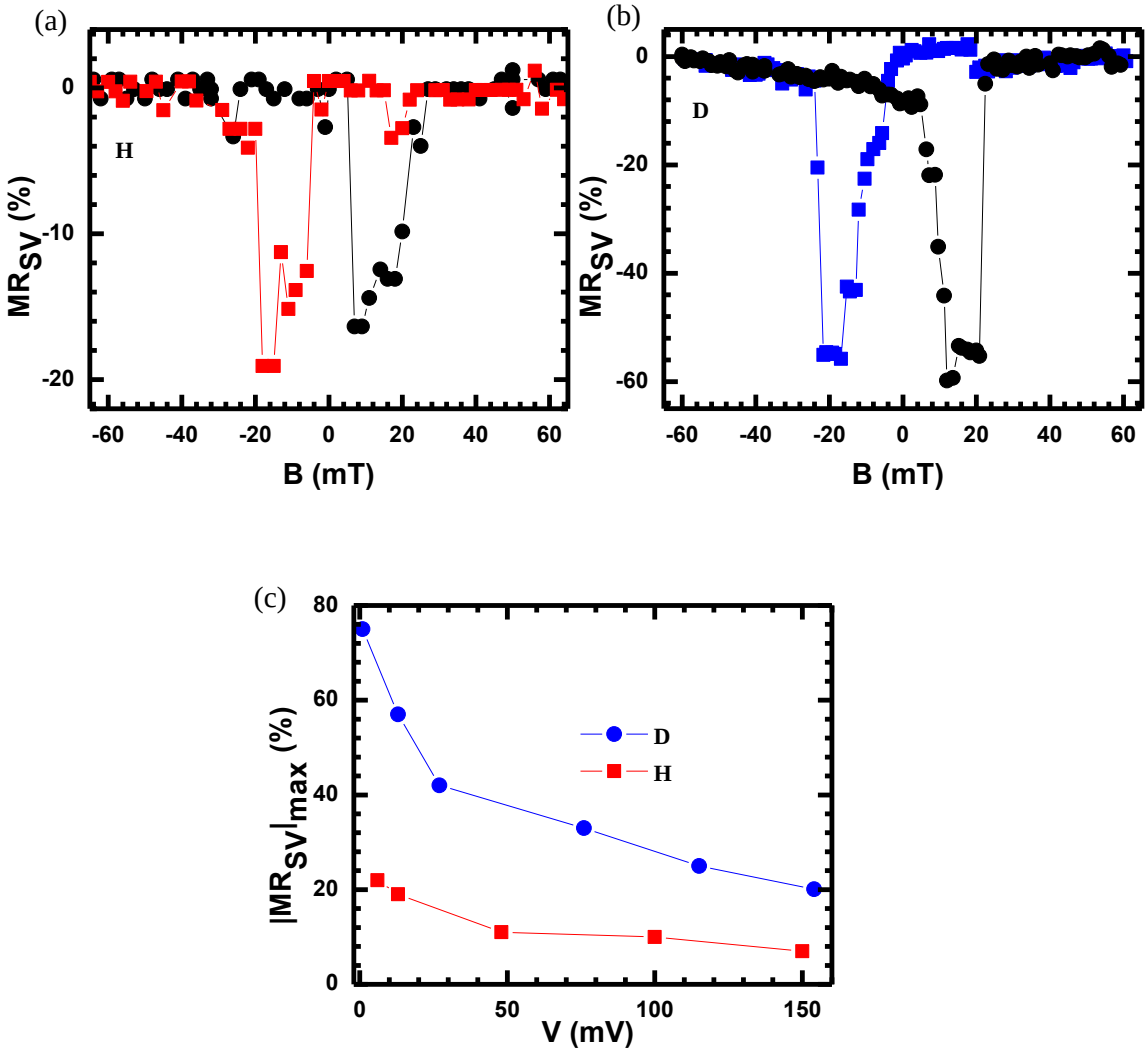

Figure 3.2. The spin valve magnetoresistance. MRSV(B) response of 40 nm thick OSV devices based on (a) H-Alq3 and (b) D-Alq3 for up (black) and down (colored) B-sweeps, measured at V=12 mV and T=10 K. (c) Voltage dependence of |MRSV|max for H-Alq3 (red squares) and D-Alq3 (blue circles).

OSV devices, λ_s increases with the spin relaxation time τ_s : (a) for carrier diffusion motion, $\lambda_s = \sqrt{D\tau_s}$, where D is the carrier diffusion constant which is proportional to the carrier mobility, μ, via the Einstein relation; (b) for carrier drift motion in an electric field F, $\lambda_s = \mu F \tau_s$. Assuming that carrier mobility is not influenced by the isotope exchange, we conjecture that the larger λ_S obtained in D- Alq_3 OSV is due to longer spin ½ relaxation time, and this also points to the importance of the HFI in the spin ½ polaron transport in Alq_3 devices.

3.1.3.3 Magneto-electroluminescence in OLEDs

3.1.3.3.1 The Low Field Regime

The MEL(B) response of H- and D-Alq_3 OLED are shown with various field resolution in Figure 3.3(a)-(c); a clear isotope-dependent response can be seen. First, as seen in Figure 3.3(b) and the inset of Figure 3.3(a), the width, ΔB, of the MEL(B) response in H-Alq_3 device is ~40% larger than that in D-Alq_3. This observation is in contrast to an earlier study in which no isotope dependence was reported [51]. Second, as seen in Figure 3.3(c), the MEL(B) response shows another feature at low fields (B~<2 mT): as |B| increases from B=0, MEL(B) is negative, reaches a minimum value at |B|=B_m, then increases crossing zero and monotonically increases thereafter. Clearly, B_m is isotope dependent: B_m=0.2 and 0.4 mT for D-Alq_3 and H-Alq_3, respectively. Similar features, dubbed ultra-small magnetic field effect (USMFE), were observed previously in DOOPPV-based OLEDs, where the isotope dependence has been shown to originate from the HFI in PP species [43, 55]. We therefore conclude that the HFI in PP species plays a dominant role also in the low field MEL response in Alq_3 devices. We note,

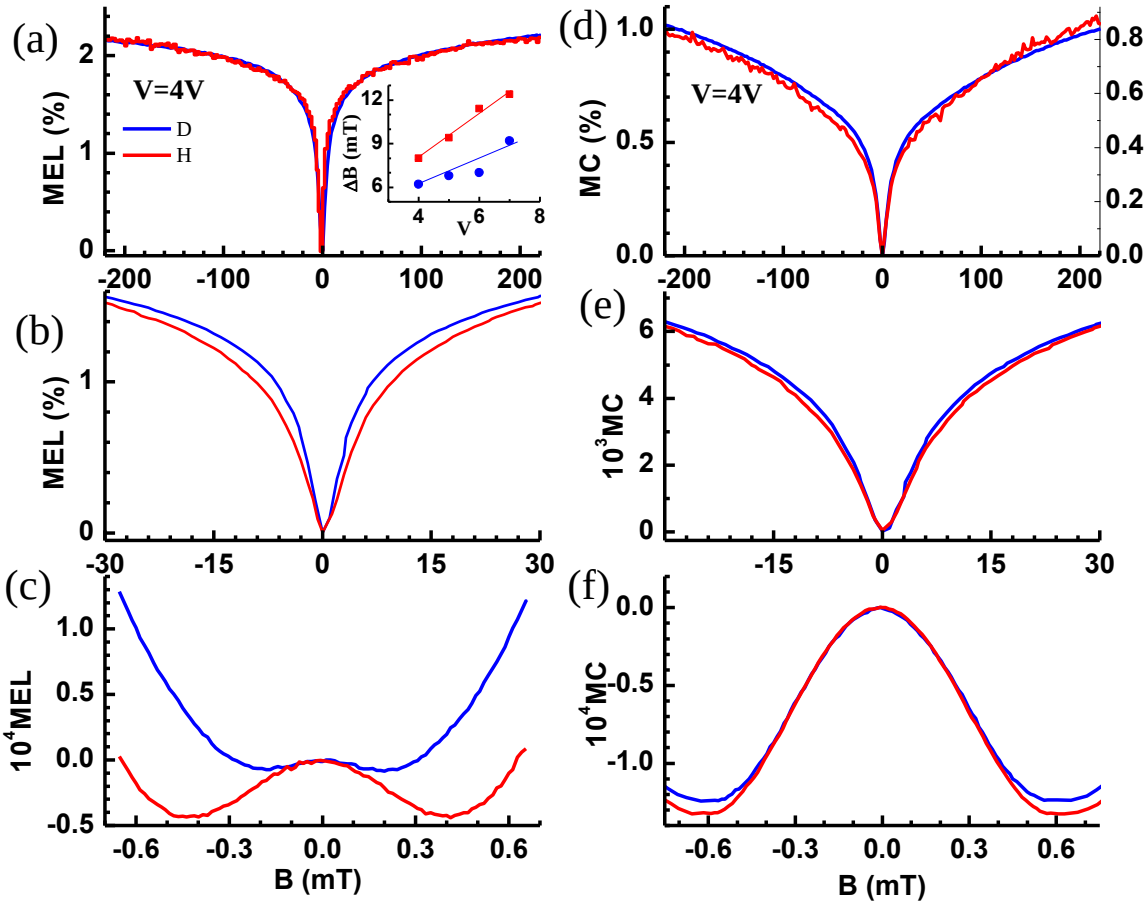

Figure 3.3. MFE response of OLEDs. (a)-(c) MEL(*B*) response of OLEDs based on H-Alq_3 (red line) and D-Alq_3 (blue line) measured at room temperature and bias *V*=4V, plotted at three *different B scales*. The D-Alq_3 response was normalized to that of H-Alq_3 at *B*~250 mT. Inset in (a): The full width, ΔB at MEL=0.8% plotted vs. *V* for H-Alq_3 (red) and D-Alq_3 (blue). (d)-(f) Same as in (a)-(c) but for the MC(*B*) responses measured on the same devices.

however, that the experimentally measured ratios $B_m(H)/B_m(D)\approx 2$ and $\Delta B(H)/\Delta B(D)\approx 1.4$ for the Alq_3 OLED are ~30-40% smaller than those measured in isotopes of DOO-PPV [55]. This observation indicates that in addition to the HFI, other interactions that are isotope insensitive have to be taken into account for explaining the detailed MEL response in Alq_3. An in-depth discussion of the isotope effect in the low field MEL response is presented in section 3.1.4 below.

3.1.3.3.2 The High Field Regime

At higher fields (|B|~50-250 mT), the MEL response does not level off but instead continues to increase, in contrast to what is expected for MFE response governed by the HFI [37, 55]. This characteristic behavior indicates that a different mechanism is dominant for the high field response of both MEL and MC. Alq_3 is known to have phosphorescence emission from triplet excitons (TE) and delayed fluorescence (DF) caused by triplet-triplet-annihilation (TTA) [58]. Therefore, it is likely that TE are involved in the MFE response at intermediate high fields. In order to examine this hypothesis, we exposed the Alq_3-based OLED devices to oxygen atmosphere, which is known to quench TE [59]. Figure 3.4 shows the MEL(*B*) response of oxygen-exposed OLED devices of both Alq_3 isotopes. The MEL response is similar to that shown in Figure 3.3, but with much clearer difference between the responses of the two isotopes: the MEL width, as defined in Figure 3.4, of H-Alq_3 OLED is now two times larger than that of D-Alq_3 OLED. This shows that the intermediate high field MEL response seen in unexposed devices comes from TE, which is insensitive to isotope exchange. When this component is quenched by exposure to oxygen, then the HFI-dominated component

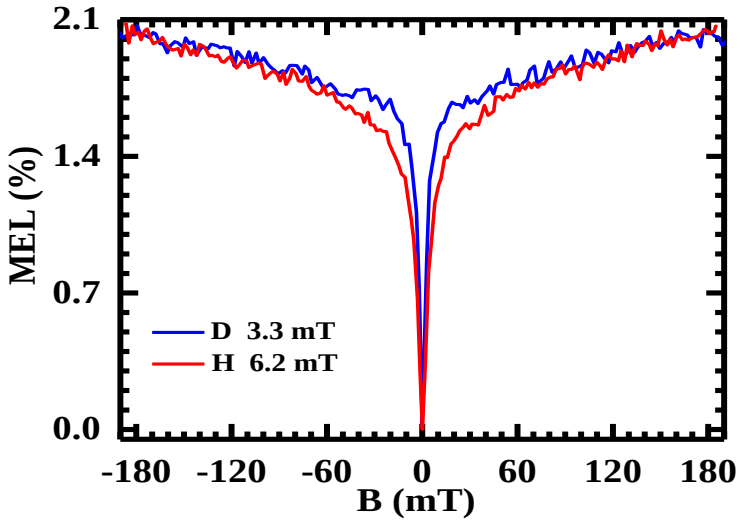

Figure 3.4. MEL(*B*) response of OLEDs based on H- and D-Alq_3 saturate exposed to oxygen, measured at *V*=4V and room temperature. The full width ΔB measured at MEL=1% is 12.4 mT (6.6 mT) for the H-Alq_3 (D-Alq_3) device. The response of D-Alq_3 was normalized to that of H-Alq_3 at B=200 mT.

prevails, and consequently, the isotope-dependent response becomes clearer.

3.1.3.4 Magneto-conductance in OLEDs

Figures 3.3(d)-(f) show the MC(*B*) response measured on the same OLED devices in which the MEL(*B*) response was measured (shown in Figure 3.3(a)-(c)). Although the MC(*B*) responses seem to be similar to MEL(*B*), the isotope dependence is different. Figure 3.3(f) shows that at low fields, $B_m(H) \approx B_m(D) \approx 0.6$ mT for the MC response, whereas the obtained ratio is $B_m(H)/B_m(D) \approx 2$ for the MEL response. Also when the D- and H- MC responses are normalized (Figure 3.3(e)) at the maximum measured field of $B_{max} \approx 220$ mT, the two responses appear to be much less isotope sensitive than the MEL responses (Figure 3.3(a)). This indicates that a mechanism *other than the HFI* dominates the MC(*B*) response at low fields (|B|<20-30 mT).

3.1.4 Discussion

3.1.4.1 The Polaron-pair Mechanism: Isotope-sensitive MEL Response

As argued in section 3.1.3, the low field MEL(*B*) response should be described by the PP mechanism, with the HFI as the main spin-mixing mechanisms. Since the measured MEL(*B*) shows significant isotope effect, the spin orbit coupling and/or the exchange interaction contributions are relatively small here. For completeness, we now present the PP mechanism model which is based on the time evolution of the PP spin sublevels in a magnetic field, and is closely related to the well-known "radical-pair" mechanism [60, 61]; versions of this model were described in more details previously [42, 55]. We note that the isotope dependence of the MEL(*B*) response can be also explained by the BP model [37].

The basic PP spin Hamiltonian, H_0, includes the Zeeman, HFI and exchange terms:

$$H_0 = H_{Zeeman} + H_{HF} + H_{ex} \quad (3.1)$$

In Eq. (3.1), H_{HF} is the HFI term,

$$H_{HF} = \sum_{i=1}^{2} \sum_{j=1}^{N_i} a_{ij} \vec{S} . \vec{I}_{ij} \quad (3.2)$$

where a_{ij} is the isotropic HFI describing the interaction between polaron spin S_i (=½) and N_i neighboring nuclei, each with spin I_{ij}. For protons in organic molecules, the HFI constant is of the order of a(H)~0.3 μeV (or $a/g\mu_B$~3 mT) [54]. The electronic Zeeman interaction term is

$$H_{zeeman} = \mu_B \left(g_1 \vec{S}_1 + g_2 \vec{S}_2 \right) . \vec{B} \quad (3.3)$$

where g_i (~2) is the respective g-factor of each of the polarons in the PP, and μ_B is the Bohr magneton. The exchange interaction is written as

$$H_{ex} = 2\mu_B B_{ex} \vec{S}_1 . \vec{S}_2 \quad (3.4)$$

where B_{ex} measures the strength of the exchange interaction (we chose here for simplicity scalar HFI, g-factors, and exchange interaction). In the absence of the spin orbit interaction, the configuration space of H_0 is of dimension:$M = 4\prod_{i=1}^{2}\prod_{j=1}^{N_i}(2I_{ij}+1)$. We did not include specifically the spin orbit interaction in Eq. (3.1), but it could in principle be calculated for the Alq_3 molecule.

When the MEL (and/or MC) originates from spin mixing within the PP species, then it is controlled by the relative PP singlet and triplet fractions, and their spin-dependent decay processes such as fusion into excitons or dissociation into free charges. These decay processes are not contained in the spin Hamiltonian, Eq. (3.1) as H_0 is a Hermitian operator that conserves energy. A convenient way to include the spin-dependent decay kinetics is to add non-Hermitian decay (relaxation) term [61, 62] to H_0:

$$H_R = -\frac{i\hbar}{2}\sum_{\alpha}\gamma_\alpha P^\alpha \quad (3.5)$$

where α designates the 4 singlet and triplet states: α=*S*, T_0, $T_{\pm1}$, P^α and γ_α are the state projection operator and decay rate constant, respectively. The time evolution of the decaying density operator is now expressed in terms of the total Hamiltonian, $H=H_0+H_R$,

$$\sigma(t) = \exp(-iHt/\hbar)\,\sigma^0 \exp(iHt)\,/\hbar\,) \quad (3.6)$$

where $H^\dagger$ is the Hermitian conjugate of H , and the t=0 density matrix σ^0 is determined by the *PP* generation process. The time-dependent singlet or triplet fraction may now be written as,

$$\rho_\alpha(t) = Tr\left(P^\alpha \sigma(t)\right) = \frac{4}{M}\sum_{n,m} P^\alpha_{nm}\sigma^0_{nm}\cos(\omega_{nm}t)\exp(-\gamma_{nm}t) \quad (3.7)$$

where $E_n = \hbar(\omega_n - i\gamma_n)$ are the (complex) eigenvalues of *H*, $\omega_{nm} = \omega_n - \omega_m$; $\gamma_{nm} = \gamma_n + \gamma_m$, the double summation (*n*,*m*) is over all M states. Eq. (3.7) expresses the fact that the singlet (or triplet) time evolution contains both a coherent character (through the $cos(\omega_{mn}t)$ factor) and an exponential decay factor. The measured MFE (that is MC and MEL) may directly be calculated using Eq. (3.7). For the MEL response, the final expression depends on the radiative recombination of the SE and the detailed relaxation route from *PP* to form SE. We denote the effective SE generation rate from the PP^α configuration by $k_{\alpha,\mathrm{SE}}$. Consequently, we define the "SE generation yield", $\Phi_{SE} = \sum_\alpha \Phi_{\alpha,SE}$ where $\Phi_{\alpha,SE}$ is given by

$$\Phi_{\alpha,SE} = \int_0^\infty k_{\alpha,SE}\rho_\alpha(t)dt = \frac{4}{M}\sum_{n,m} P^\alpha_{nm}\sigma^0_{nm}(0)\frac{k_{\alpha,SE}\gamma_{nm}}{\gamma^2_{nm} + \omega^2_{nm}} \quad (3.8)$$

The contribution of the PP mechanism to the *MEL(B)* response is then given by,

$$MEL_{PP}(B) = \frac{\Phi_{SE}(B) - \Phi_{SE}(0)}{\Phi_{SE}(0)} \quad (3.9)$$

In Figures 3.5(a) and 3.5(b), we show the simulated MEL_{PP} response, using Eq. (3.9) for two HFI cases that correspond, respectively, to H- and D-Alq_3: (i) I=½ and $a_{HF}/g\mu_B$=2.5 mT, and (ii) I=1 and $a_{HF}/g\mu_B$=0.4 mT. In both cases, the exchange and SOC strengths were chosen to be approximately 0.2 mT. Comparing the simulation to the MEL data presented in Figure 3.3(b) and 3.3(c), we conclude that the isotope-dependent width and USMFE minima are captured by the PP mechanism with the HFI as the main spin-mixing process.

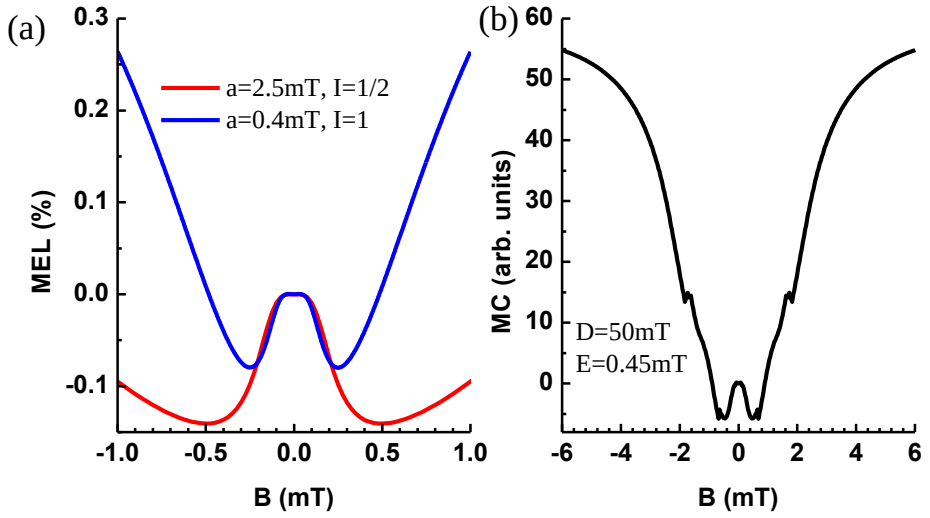

Figure 3.5. Model simulation for the low field MEL and MC responses of Alq_3. (a) PP mechanism for MEL(B) of H- and D-Alq_3: red line, $a/g\mu_B$=2.5 mT, I=½ (H); blue line, $a/g\mu_B$=0.4 mT, I=1 (D). A finite exchange interaction of strength B_{ex} =0.02 mT was used for both responses. (b) Polaron/PP triplet scattering model for the isotope-independent MC(B). The line shown is for $D_P/g\mu_B$=50 mT, $E_P/g\mu_B$=0.45 mT.

3.1.4.2 Collision of Spin ½ Polaron with Triplet-state Polaron-pair:

Low Field MC Response

Unlike the MEL response discussed in the preceding section, the experimentally measured MC(B) response does not show much isotope effect due to HFI, indicating the dominance of a different spin-mixing mechanism. In this section, we introduce a novel, isotope-insensitive mechanism that affects the MC response but does not affect the MEL response.

The many PP that are produced from the injected free carriers do not have a fixed interpolaron distance, d_P, but rather form a distribution of d_P's. As the PP fuse to form excitons, d_P gradually decreases while the singlet and triplet states PP, namely PP_S and PP_T, separate in energy until the appropriate values for the SE and TE in the material are reached. In the intermediate state, where spin mixing between PP_S and PP_T has already been diminished due to their large energy separation, PP_T still evolves with B because of its non-zero spin. PP may interact with spin ½ carriers via magnetic spin-spin interaction. Such an interaction may be described by a collision process by which a spin ½ carrier ("polaron") is temporarily paired with a close PP_T neighbor which causes magnetic field-dependent carrier density that generates a finite MC(B) response. This mechanism does not contribute to MEL, and is insensitive to isotope exchange. The contribution to MC(B) comes from the direct PP_T dissociation, thus leading to isotope-independent MC response. Similar triplet-doublet interaction has been considered before in connection with TE quenching by free radicals [63] and for mobilization of trapped charge carriers in molecular crystals [64].

Similar to the triplet-doublet collision model [63], we envision the above carrier-

PP collision event as a process by which the S_1=1 PP_T and S_2=½ charge carrier are temporarily paired together (forming a PP_T-P pair), evolve with time in a magnetic field, and then dissociate to free carrier and PP_T, respectively. The PP_T-P species may be either in a quartet ($S=S_1+S_2=3/2$) or doublet ($S=S_1-S_2=½$) spin states. The PP_T-P species spin Hamiltonian in a magnetic field may be written as,

$$H_P = H_{PPT} + J_P \vec{S}_1 . \vec{S}_2 + H_Z + H_R \tag{3. 10}$$

where H_Z is the Zeeman energy term given by Eq. (3.3) with g_1 (g_2) as the PP_T (free carrier) g-factor, J_P is the PP_T-P spin-spin interaction constant, and H_{PPT} is the PP_T triplet term given by

$$H_{PPT} = \vec{S}_1 . \tilde{\tau} . \vec{S}_1 \tag{3. 11}$$

where S_1=1 is the PP_T spin and $\tilde{\tau}$ is the triplet [65] symmetric traceless tensor of rank 2. In the triplet principal reference frame: $H_{PPT} = D_P \left(S_{1z}^2 - \frac{2}{3} \right) + E_P (S_{1x}^2 - S_{1y}^2)$, where D_P and E_P are referred to as the PP_T zero field splitting (ZFS) parameters. The decay of the quartet and doublet states (with decay constants γ_{Qr} and γ_{Db}, respectively) is represented by the non-Hermitian relaxation term [61, 62] H_R in Eq. (3.10) similar to Eq. (3.5). Following the procedure outlined in section 3.1.4.1 above, we may now calculate the magnetic field-dependent density of free polarons dissociated from the PP_T-P pairs. Denoting the dissociation rate from the $(PP_T\text{-}P)^{\alpha}$ (α=quartet, doublet) configuration by d_α, the free polaron yield and its contribution to MC are given by Eqs. (3.8)-(3.9), with d_α in place of $k_{\alpha,SE}$. The decay and dissociation constants (γ_α and d_α) determine mainly the magnitude of the MFE, whereas the triplet parameters D_P and E_P determine the overall width and the behavior at low fields (for $E_P << D_P$), respectively. In Figure 3.5(b), we

show a simulated MC(*B*) response for $D_P/g\mu_B$=50 mT and $E_P/g\mu_B$=0.45 mT. The simulated response is isotope insensitive, and features the sign change and minimum observed at *B*<1 mT as in the experiment (Figure 3.3(f)). It is important to note that in addition to this proposed mechanism, other triplet-based mechanisms (e.g. polaron collision with TE) exist in the literature, and may be also responsible for the high field MFE response.

3.1.5 Conclusions

Using the spin ½ CDMR and MR in OSV devices based on H- and D- Alq_3, we showed that the HFI is indeed a significant spin relaxation mechanism for spin ½ polarons in Alq_3. Moreover, the HFI provides an important spin-mixing mechanism for polaron-pairs in Alq_3 that may explain the MEL(B) response. The reduced HFI in D-Alq_3 with respect to H-Alq_3 is clearly observed in a variety of spin ½-related experiments. We obtained: (a) narrower spin ½ CDMR resonance line in D-Alq_3; (b) longer spin diffusion length in OSV based on D-Alq_3; (c) narrower MEL(*B*) response and smaller B_m in OLEDs based on D-Alq_3. In contrast, the MC(*B*) response is much less sensitive to isotope exchange and thus the HFI-based spin-mixing mechanism here is overwhelmed by another, isotope-insensitive spin-mixing mechanism. To explain the low field behavior of MC in Alq_3, we offer an isotope-independent interaction between free carrier with S=½ and triplet-state PP.

3.2 Energy Transfer in a 'Host-Guest' System Comprised of MEHPPV and Pt(tpbp); Electroluminescence Quenching in OLEDs

3.2.1 Introduction

Organic light emitting diodes (OLEDs) have attracted much attention in recent years both for commercial applications, and for better understanding the physics of organic films [25, 66-70]. Light is emitted in organic materials when bound electron hole pairs or excitons decay by emitting photons [71]. Singlet excitons with zero spin can radiatively recombine, whereas triplet excitons do not undergo radiative recombination due to spin selection rules in the presence of very weak spin-orbit coupling (SOC) in the organics. Since the charge recombination statistics generates 1:3 singlet to triplet excitons ratio [72] in OLEDs, harvesting the triplet excitons in such devices is crucial for better performance of these devices. One way of achieving triplet exciton emission, i.e. phosphorescence, is by incorporating a heavy molecule [73] which has large SOC, along with the luminescent polymer in the device. Emission from the triplet is necessary not only to enhance the luminance but also to produce the necessary broad white light emission (WOLED devices). Several methods to generate such a broad spectrum and harvest light from the triplet exciton exist. Some of these techniques include using a blue emitters OLED [74, 75], materials having dimer or excimer emission [76], blended [66] single layer or multilayer devices [77], or using high efficiency diodes with delayed phosphorescence [29]. Solution processed materials are increasingly considered as a promising route to cost-effective, large-scale manufacturing of highly efficient OLEDs [67].

In this work, we studied the photo-physics and electrical characteristics of a solution processed, blend film of poly-[2-methoxy, 5-(2'-ethyl-hexyloxy)phenylene vinylene] (MEH-PPV) and PtII–tetraphenyltetrabenzoporphyrin (Pt(tpbp))(molecular structures in Figure 3.6 insets) and their OLED to see both the singlet and triplet emission bands. MEHPPV is a widely used luminescent polymer [78] which has emission at ~ 2 eV and the Pt(tpbp) is a phosphorescent molecule [79, 80] that has an emission band at ~1.7 eV. In electro-phosphorescent OLEDs, electrons and holes are initially injected into the organic host transport material, and then the excitation is transferred to the phosphorescent emitter via the Forster/Dexter energy transfer mechanism [81, 82]. We expect to have high energy transfer in this host-guest system due to the spectral overlap of the emission band of the host with the absorption band of the guest. To compare the population of singlet in the host and triplet in the guest, we have monitored the emission and PA spectra of the blend, and their magneto-PA(MPA) response. We identified the pathway for populating the host triplet state, as well as the possible cause of the lower external quantum efficiency (EQE).

MEHPPV has PL and EL yellow emission band which overlaps with the absorption spectrum of Pt(tpbp). A small percentage of the Pt(tpbp) is sufficient to induce transfer of excitons from the host to the guest in the blend. Once we excite the blend film, the photogenerated singlet excitons may radiatively decay to the ground state or transfer to the singlet of the guest which, after converting to the triplet state, either radiatively decay to the ground state or transfer to the host triplet. The emission efficiency could be enhanced if all the triplets radiatively decay, but due to the triplet energy level of MEHPPV, ~1.27eV [83, 84], being lower than the triplet level of the

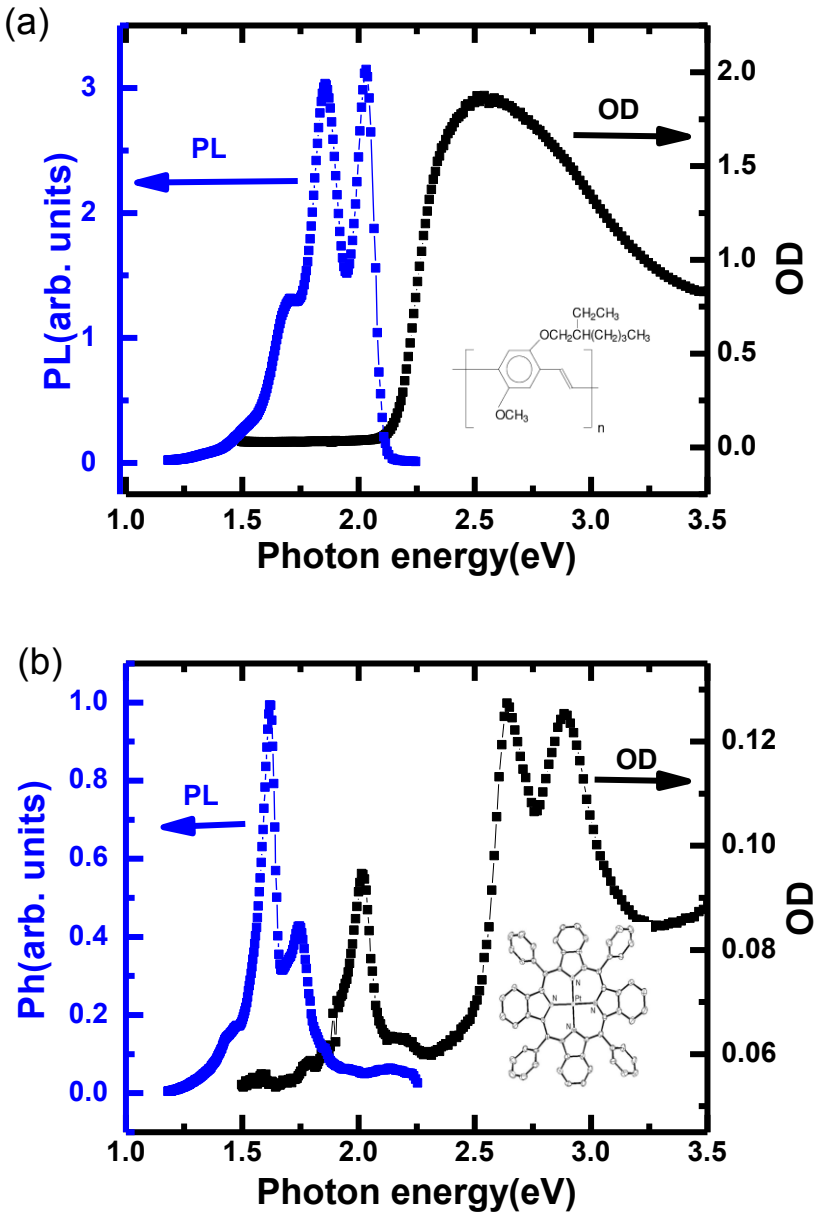

Figure 3.6. Absorption(black) and emission(blue) spectra of (a) pristine MEHPPV film (b) Pt(tpbp) film prepared in 2% polystyrene(PS) matrix. The insets in (a) and (b) show the molecular structure of MEHPPV and Pt(tpbp), respectively.

Pt(tpbp), ~1.62eV [85], we will show that another route for the transfer of the guest triplets to the host triplets dominates. PA measurement of the film is a reliable method to measure the density of triplet excitons in the host.

Magnetic field effect (MFE) measurements in OLEDs is widely studied and explained by several models [36, 55, 86, 87] while MFE on film is less studied [88]. Mobility-dependent MFE explanation [37, 39] for the OLEDs does not contribute to the MFE in films where charge carriers do not produce any current. A magnetic field may induce the triplet sublevels mixing [88] at low triplet concentration and Triplet-Triplet Annihilation (TTA) mechanism prevails at high triplet density. Therefore, the indication of the TTA component on MPA is the confirmation of high triplet density.

3.2.2 Experimental

For the optical studies, samples were prepared in Toluene at the concentration of 10 mg/ml. MEHPPV or the MEHPPV blended with different percentage of Pt(tpbp) were stirred overnight and drop-casted on the sapphire substrate. Subsequently, the films were placed in a cryostat and cooled down to 50K by a closed cycle refrigerator. We used a cw Ar^+ laser at 488 nm and a 405nm diode laser as the excitation pump and a tungsten lamp as the probe. Change in the transmission with and without the probe was recorded by a phase-sensitive technique via a lock in amplifier of which reference was a light modulation by the mechanical chopper at 310 Hz. PL emission was measured by illuminating the sample with the laser, and PA was obtained by the relation $-\Delta T/T$, where ΔT is the change in transmission with pump on and off. For the MPA measurement, the same setup for PA was used with the magnetic field applied parallel to the surface of the

film using the electromagnet which could produce a field up to 1800 Gauss.

For the OLED device, the same solution used for the optical studies was used to spin-coat a neat film on a cleaned ITO substrate. The device structure for the OLED is comprised of a thin ITO layer, 40 nm of PEDOT:PSS poly(3,4-ethylenedioxythiophene) and poly(styrenesulfonate) layer, an active layer of MEHPPV polymer or its blend with Pt(tpbp), and capped with Calcium and Aluminum electrodes. The device dimension was 2mm×2mm.

3.2.3 Results and Discussion

Figure 3.6(a) shows the optical absorption (optical density (OD)) and photoluminescence (PL) spectra of the MEHPPV polymer and Pt(tpbp) molecule. UV-VIS of the material was measured with a Cary 17 spectrophotometer at room temperature on the spin-coated sample. PL measurements were performed on the drop casted film at low temperature (50K) in the cryostat. Samples were prepared from a 10mg/ml solution of MEHPPV and 2% Pt(tpbp) in Polystyrene(PS) using toluene as the solvent in a nitrogen atmosphere in a glove box. In Figure 3.6(a) the OD of MEHPPV has a broad peak at ~2.54eV and PL spectrum has the 0-0 peak at ~2.03eV and several phonon replicas. Figure 3.6(b) shows the OD and PL of Pt(tpbp) where the OD peak at ~2.01eV overlaps with the PL band of MEHPPV. Therefore, there is the possibility of both Forster and Dexter energy transfer from MEHPPV host polymer to the Pt(tpbp) guest molecule because of the overlap of the emission band of MEHPPV with the absorption band of Pt(tpbp).

We fabricated an OLED device of the pristine MEHPPV and its blend with

Pt(tpbp). Figure 3.7(a) shows the EL spectra of the pristine MEHPPV(black), 3% (red), 5%(blue) and 7%(magenta) Pt(tpbp) as a guest in MEHPPV. As the additives concentration increases, the phosphorescence band is more pronounced and thus the EL spectrum contains emission from both guest and host. The EL onset for the blend is at smaller voltage than the pristine OLED, showing the more efficient current injection in the blend probably caused by the higher carrier mobility in the blend. However, the electro-luminescence quantum efficiency (ELQE) steeply decreases in the blend, and higher current density is required to obtain EL emission from the device. Figure 3.7(b) shows the ELQE of the OLED for the pristine MEHPPV (black), 5% Pt(tpbp)(red) and 7% Pt(tpbp)(blue); it is clearly seen that the ELQE decreases with increasing Pt(tpbp) weight percentage, while the pristine MEHPPV device has the highest ELQE compared to the host-guest blend devices.

We studied the photo-physics of films of the same materials that were used for the OLEDs fabrication. Figure 3.8(a) shows the PL spectra of MEHPPV blended with Pt(tpbp) at different percentages: 1%(black), 5%(red), 7%(blue), and 10%(magenta). Since MEHPPV has stronger absorption at the pump photon energy, mostly the MEHPPV polymer is excited while very little excitation of Pt(tpbp) occurs due to its low OD at the pump photon energy and its low concentration in the blend. However, due to energy transfer from MEHPPV to Pt(tpbp), both luminescence and phosphorescence can be seen in the blend emission spectra. At lower concentration of the guest, host emission dominates the PL emission spectrum. Increase in the concentration of the guest molecules increases the phosphorescence (Ph) intensity as is clearly seen for the 5% or 7% Pt(tpbp) PL spectra. Further increasing the guest concentration reduces the intensity of both PL

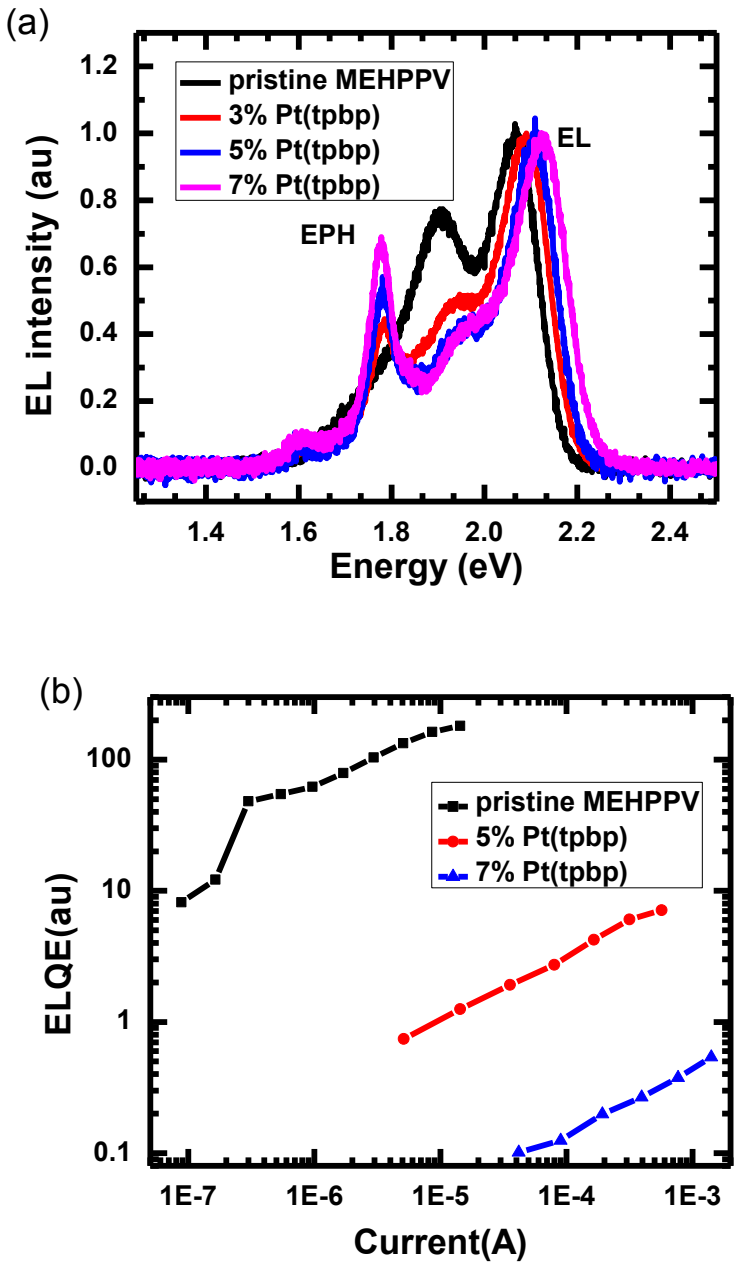

Figure 3.7. Electroluminescence of OLED. (a) EL spectra of pristine MEHPPV(black), 3%(red), 5%(blue) and 10%(magenta) Pt(tpbp) in MEHPP;(b) Electroluminescence quantum efficiency(ELQE) of OLEDs comprised of pristine MEHPPV(black), 5% Pt(tpbp)(red) and 7% Pt(tpbp)(blue).

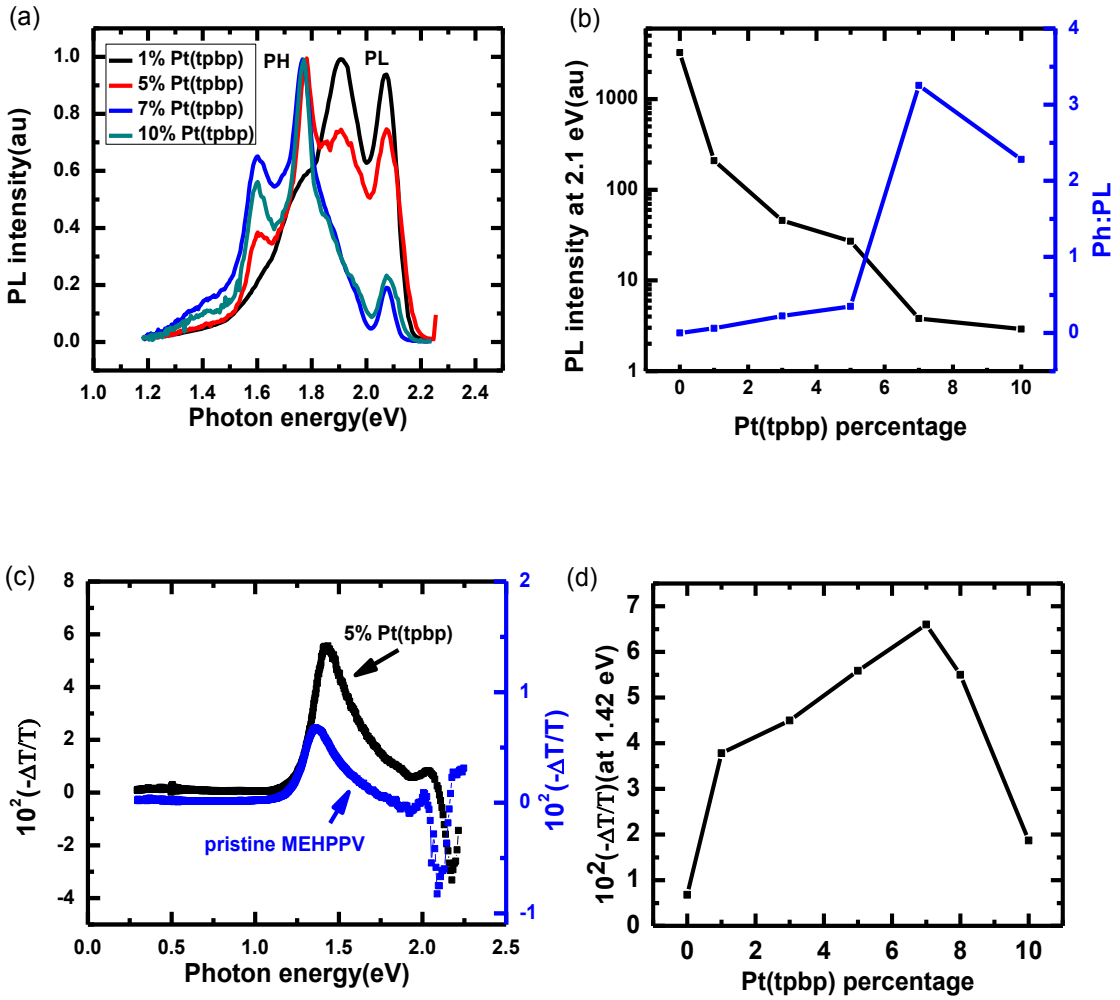

Figure 3.8. PL emission and PA spectra in films of various MEHPPV/ Pt(tpbp) blends. (a) PL spectra of 1%(black), 5%(red), 7%(blue) and 10%(magenta) Pt(tpbp) films; (b) PL intensity at 2.1 eV(black) vs Pt(tpbp) percentage; ratio of Ph intensity to PL intensity(blue)(c) PA spectra of pristine MEHPPV(blue) and 5% Pt(tpbp)(black) film;(d) PA intensity at 1.42 eV vs Pt(tpbp) percentage.

and Ph emissions. The overall emission is substantially reduced compared to pristine MEHPPPV emission intensity as shown in Figure 3.8(b)(black). The blue line in Figure 3.8(b) shows the ratio of Ph intensity to the PL intensity that increases with the guest percentage. However, at concentration over 7%, the Ph intensity reduces due to quenching of the emission influenced by the guest molecule aggregates at high concentration. Reduction in the overall emission intensity reveals that emissive singlet excitons are transferred to nonemissive triplet excitons. The PA spectrum is measured to see whether there is triplet density enhancement of MEHPPV induced by the molecule additives. Figure 3.8(c) shows that the 5% Pt(tpbp)(black) film has stronger PA signal than the pristine MEHPPV(blue) film. Here, PA= $-\Delta T/T = n\sigma d$, where, n= number density of the triplet species, σ is their opticalcross-section and d is the film thickness. Assuming σ and d are almost the same, n for 5% Pt(tpbp) is much higher than in the pristine film. Therefore, the Pt(tpbp) additives lead to the formation of large number of triplet excitons in the host, probably via polymer singlet- guest singlet- guest triplet- polymer triplet pathway (a 'ping-pong' like reaction sequence). Figure 3.8(d) shows the intensity of the PA signal at 1.42 eV as the function of Pt(tpbp) percentage. At an additive weight % >7%, quenching of the triplet excitons in the guest molecules also reduces the triplet exciton density in the host.

The scheme for the singlet and triplet energy transfer in the host/guest system of MEHPPV and Pt(tpbp) is shown in Figure 3.9. The pump excitation generates singlet excitons in the host (MEHPPV polymer) followed by the emission band at ~2.0 eV S_H of the host. The singlet excitons may, however, transfer either to the triplet excitons, T_H, in polymer through intersystem crossing or to the singlet of the Pt(tpbp), S_G, through Forster

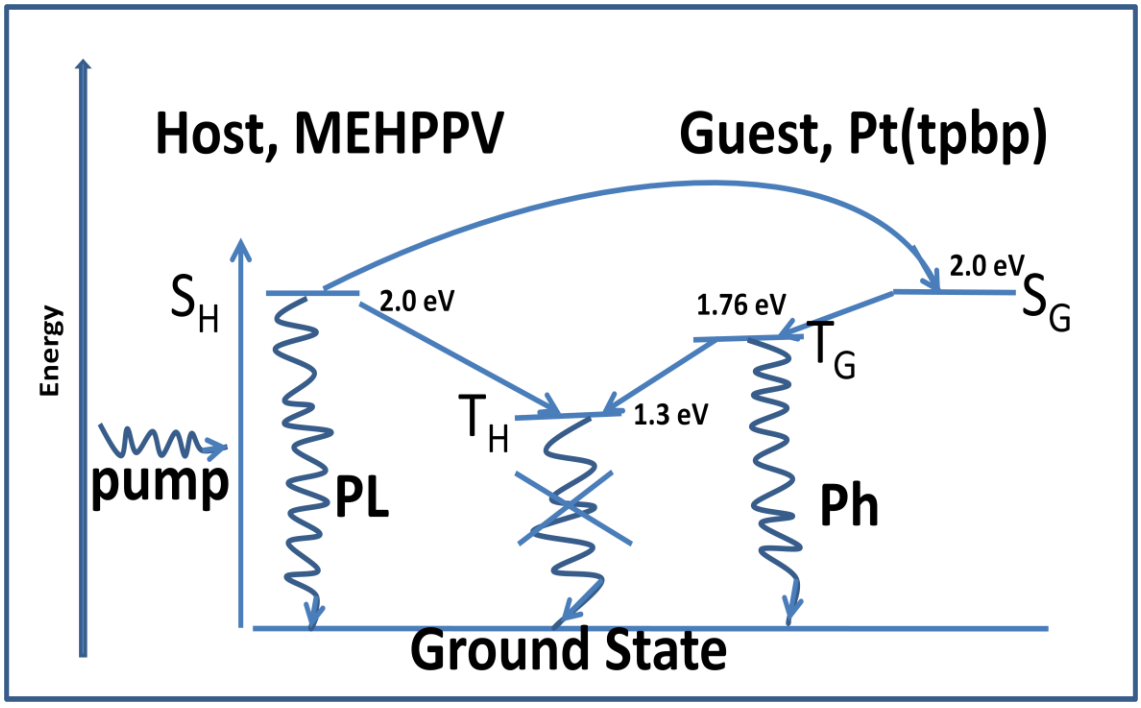

Figure 3.9. Schematic of the relevant energy levels in the MEHPPV/(Pt(tpbp) host/guest system, and the 'ping-pong' type energy transfer reaction sequence.

and Dexter energy transfers. Singlet excitons in Pt(tpbp) immediately convert to the triplet state, T_G, due to the strong SOC in this molecule, that consequently radiatively decay to the ground state yielding phosphorescence emission. Since the triplet energy level of Pt(tpbp) is higher than the triplet in MEHPPV, the triplet excitons in the guest molecule decay to the triplet exciton in the host polymer. Therefore, the triplets in MEHPPV act as energy sink because they decay nonradiatively to the ground state. Hence, most of the excitons in the guest transfer to the triplet excitons in the MEHPPV, thereby reducing the emission efficiency of the host/guest system.

To check this scenario, we measure the magnetic field effect (MFE) of the triplet excitons in the blend system. Upon photon absorption, singlet excitons are generated in the picoseconds time domain and subsequently undergo intersystem crossing to the triplet manifold in the nanosecond time domain. Subsequently, the triplet excitons population changes upon applying an external magnetic field, because the magnetic field removes the degeneracy of the triplet excitons by splitting into triplet sublevels via the Zeeman interaction. Figure 3.10(a) shows the MPA response of pristine MEHPPV film at low laser power of 10mW where Triplet-Triplet annihilation (TTA) is absent. This is in agreement with our previous work [88]. Upon increasing the laser power (Figure 3.10(b)), we get two components MPA response, which is typical for TTA [88]. Figure 3.10(c) and 3.10(d) shows the MPA response for the 5% Pt(tpbp) film at low (10mW) and high (75 mW) laser power , respectively. The MPA response for the blend is similar to that in the pristine MEHPPV, but the TTA occurs at substantively lower laser power. This supports the assumption that the triplet density is enhanced in the blend.

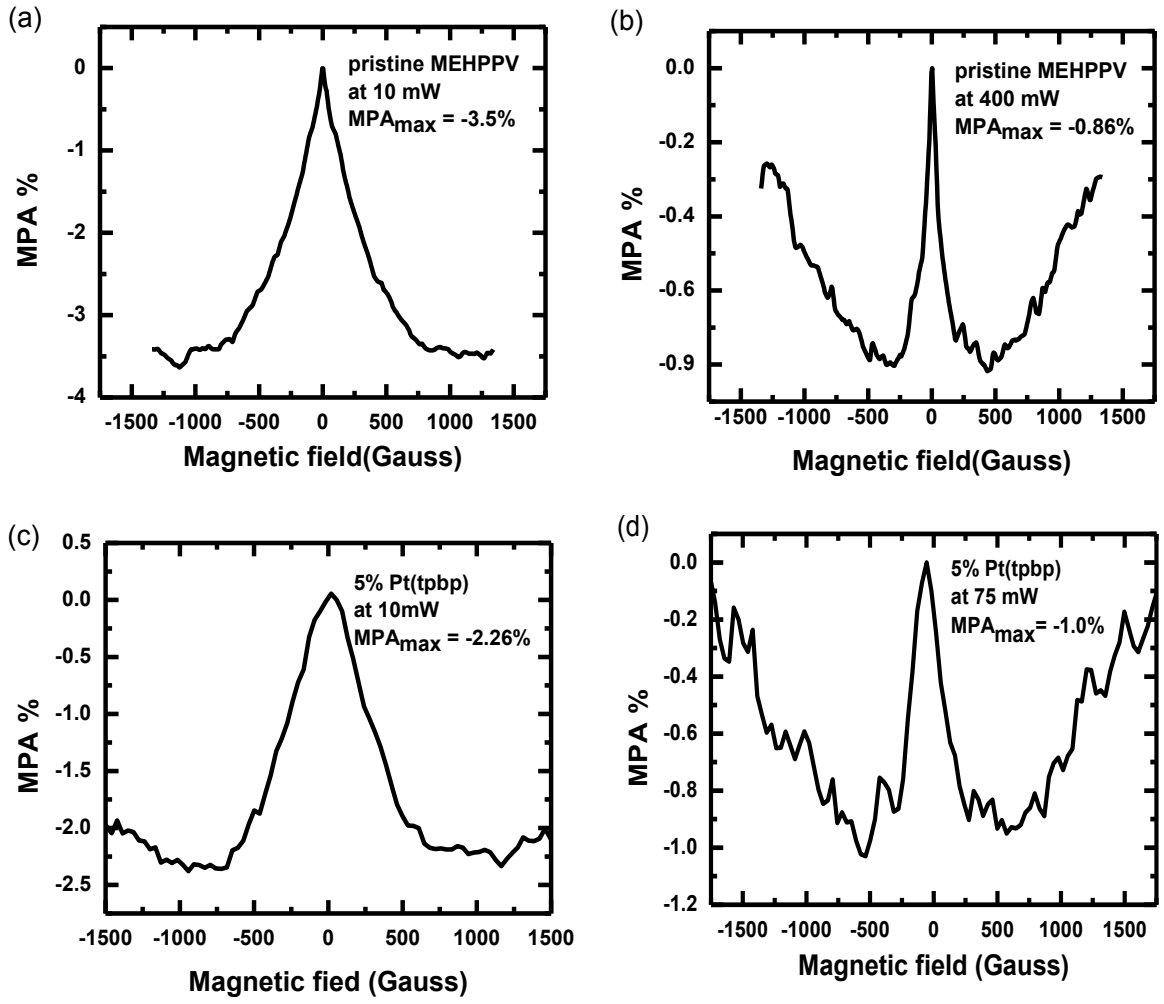

Figure 3.10. MPA(B) response at different laser power; pristine MEHPPV film at (a) 10 mW and (b) 400 mW; and 5% Pt(tpbp) film at (c) 10 mW and (d) 75 mW.

3.2.4 Conclusions

In summary, we studied the optical, electrical, and magnetic properties of the blend system where MEHPPV acts as the host polymer and Pt(tpbp) acts as the guest molecule. Our study shows that the host triplet exciton density in the blend is significantly enhanced and the emission intensity is highly reduced for both EL emission in OLEDs and PL emission in films. The underlying mechanism of this curious behavior is the triplet level of MEHPPV. It is lower than the emissive triplet level of the Pt(tpbp). Therefore, the triplet excitons in the guest find another energy transfer pathway to the triplet excitons in the host, making it unavailable for emission in the guest. This 'ping-pong' type reaction sequence is unique to this host/guest blend. Furthermore, the MPA and MPL responses in the blend show that the TTA MFE response occurs at lower laser power in the blend verifying the presence of large number of triplet excitons in the blend system.

3.3 Magnetic Field Effect in Electroluminescence; Color Manipulation

3.3.1 Introduction

It is known that the current density control in the OLED induces changes in the emission color. This happens in the host-guest OLED system where the guest triplet emission is saturated at high current, whereas the host emission continues to increase with increasing current density [28]. Therefore, the emission color is blue shifted due to the enhanced host emission. Here we report the magnetic field-induced color control in white light emitting diodes (WOLED) based on a host-guest blend system.

Organic magneto resistance (MR), or equivalently, magneto conductance (MC) is defined as MC = (I(B)-I(0))/I(0) where I(B) is the current on applying magnetic field B and I(0) is the current through the OLED device at B=0. The reason for MC is believed to be induced change in the spin correlations between the charge carriers upon the application of an external magnetic field. These correlations are affected by the randomly oriented hyperfine fields produced by the hydrogen nuclei [53]. Magnetic field effect (MFE) in OLEDs is widely studied and explained by several models, e.g., bipolaron [37, 89], polaron pair [90], excitons charge interaction [39], triplet-triplet annihilation (TTA) [91], Δg [38] etc. These models mainly focus on the magnetic field effect on the charge carrier densities or on charge transport. Mobility-dependent MFE explanation [37, 39] in OLEDs does not apply for MFE in general since it is observed also in the optical studies of the film [88], such as MPA and MPL (see the section above). Here we study MEL in the different regions of the EL spectrum in the host/guest type OLED where we observed modulation of the EL color that can be explained by the polaron pair model, where magnetic field changes the singlet-triplet polaron pair densities.

3.3.2 Experimental

We used two different host/guest blends; one is the Poly(9,9-dioctylfluorene)(PFO) as the host and Iridium(III)bis(2-(2'-benzothienyl)pyridinatoN,$C^{3'}$(acetylacetonate)($Ir(btp)_2acac$) as the guest; and the other is MEHPPV as host and Pt(tpbp) as guest (similar to that of the section 3.2 above). The luminescent organic active layers were prepared in Toluene at the concentration of 10 mg/ml for the host and 1 mg/ml for the guest. Isolated films in polystyrene were prepared

at 2% concentration. Solutions were stirred overnight to allow homogeneous mixing. For the PL studies, we prepared drop-casted films on sapphire substrates that were placed in a low temperature cryostat and cooled down to 50K by a closed cycle refrigerator. We chose a cw Ar^+ laser at 488 nm and a 405 nm diode laser as the excitation sources, depending on the absorption spectra of the investigated materials.

For the OLED devices, a thin film was prepared by spin-coating at the rate of 600 rpm to 5000 rpm on a cleaned ITO substrate. The device structure for the OLED is comprised of thin ITO layer, 40 nm of PEDOT:PSS poly(3,4-ethylenedioxythiophene) and poly(styrenesulfonate) layer, the active layer of the host polymer or the host- guest blend, capped with Calcium and Aluminum for the top electrode. The anode ITO substrate was cleaned by ultrasonic treatment with Acetone, 2% micro-90 soap, de-ionized water, methanol, and propanol each for 10 minutes. PEDOT:PSS was spin-coated onto the ITO substrate and the substrates were transferred to a glove box. The anode substrate was baked for half an hour at 100°C to remove water content and the active layer of pristine polymer or the blend was spin-coated. Device fabrication process was finalized with the deposition of Ca and Al layer using thermal evaporation technique. The OLED device dimension was 1mm×1mm.

3.3.3 Results and Discussions

Figure 3.11(a) shows the absorption (in terms of optical density (OD)) and PL spectra on the pristine PFO film. PFO has absorption onset in the UV and strong blue emission; the absorption peaks at ~3.2eV and the emission peaks at ~2.8eV with several phonon replicas at lower energies. Figure 3.11(b) shows the absorption and emission for

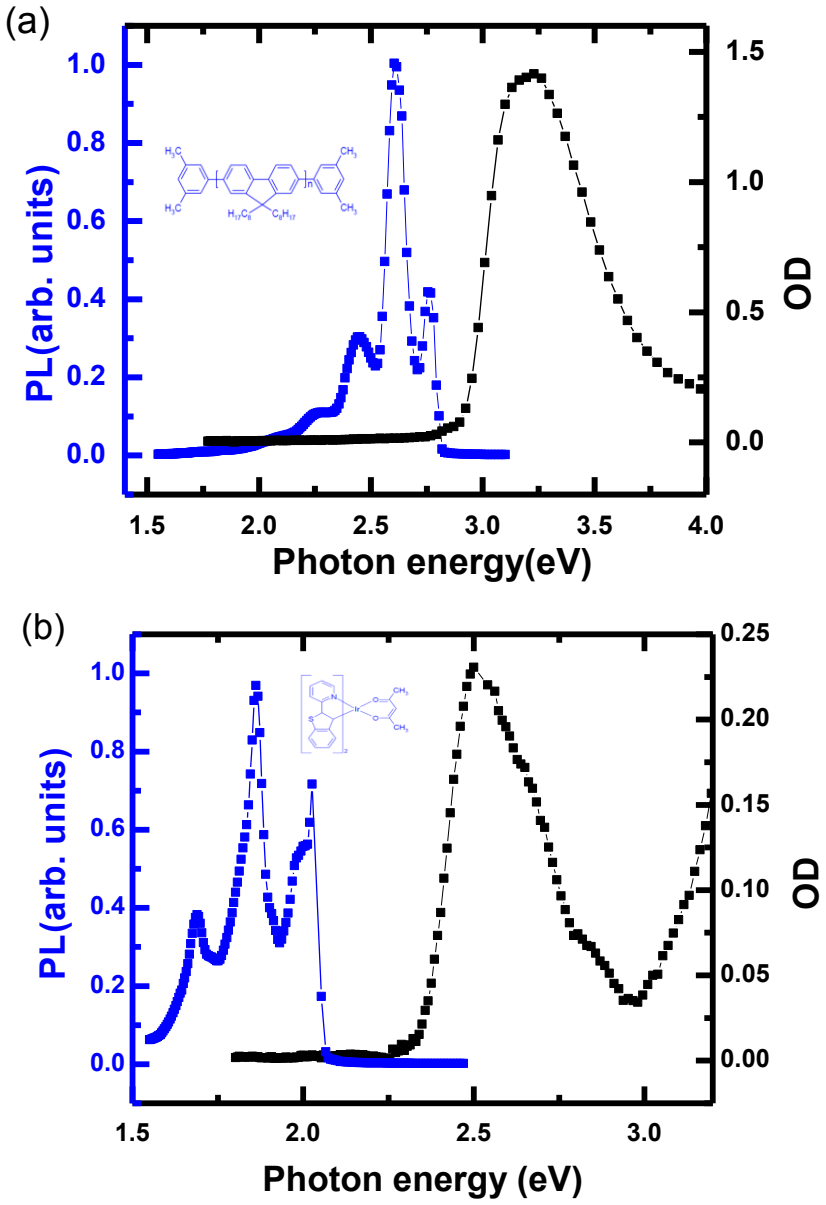

Figure 3.11. Emission (blue) and absorption (black) spectra of (a) PFO (b) $Ir(btp)_2acac$ film. The insets show the molecular structure of (a) PFO (b) $Ir(btp)_2acac$.

isolated Ir(btp)2acaac in polystyrene film. It has an absorption peak at ~ 2.5eV and red emission that peaks at ~2.01eV with phonon replica at 1.86eV and 1.68eV, respectively. We note that the PL emission of the PFO peaks at 2.5eV that perfectly matches the absorption band of Ir(btp)2acac . We chose these materials for the efficient energy transfer from host to guest since the overlap of host emission with guest absorption is prominent. Figure 3.11 insets show the molecular structure of these materials. PFO emission is red-shifted depending on the beta (ordered) or alpha (glassy) phases, which depends on the film preparation process and morphology [92, 93].

We prepared different solutions of varying Ir(btp)2acac weight percentage in the PFO solution, and measured PL emission of these blends. Figure 3.12(a) shows the PL emission from 5% $Ir(btp)_2acac$ mixed in the PFO; we can clearly see the emission from the both PFO and the $Ir(btp)_2acac$. This particular blend has strong luminescence emission both at room temperature and low temperature (Figure 3.12(a), black and blue lines, respectively). Though the concentration of the guest is not sufficiently high to effectively absorb the photons directly from the laser excitation, the emission peak of the guest is pronounced because of the efficient energy transfer from host to guest. At smaller percentage of the guest, host emission is stronger as compared to the guest emission and the guest emission intensity is increased with increasing the guest concentration. However, above 5% guest, the overall emission is quenched due to bimolecular recombination in the guest materials. We compared the phosphorescence of the guest to the host PL emission intensity ratio vs. the guest percentage as shown in Figure 3.12(b). Relative emission intensity of the guest is maximum at 5% concentration at both low and room temperature.

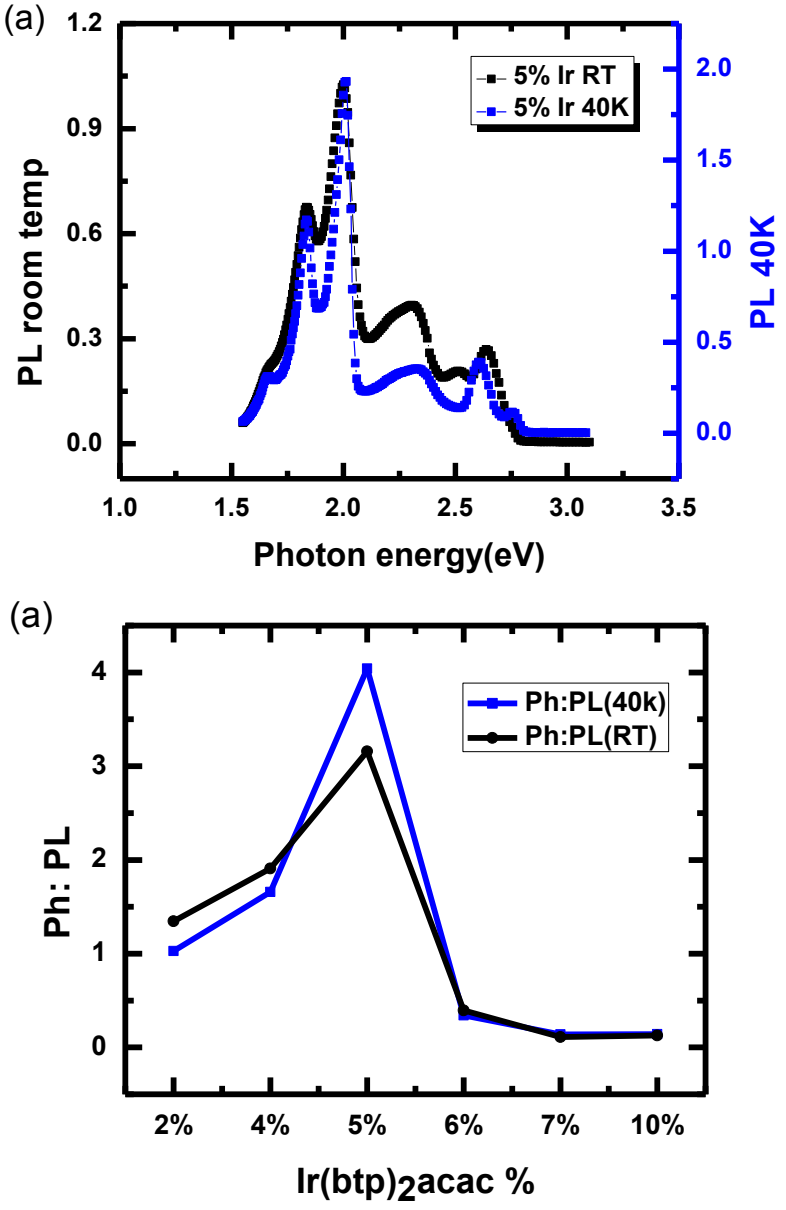

Figure 3.12. PL emission in the film. (a) PL spectra of the 5% $Ir(btp)_2acac$ in PFO at two different temperatures. (b) Phosphorescence to PL intensity ratio in the host-guest blends versus the guest percentage.

From the absorption and emission spectra, it is clear that there is sufficient energy transfer from the host to the guest, and optimization of the guest percentage enables us to see a broad spectral emission. Fabricating an OLED from such a blend gives white light emission, which is of great interest for practical applications. In this work, we fabricated OLEDs with different guest concentration to reach white light emission condition. Since we apply the external electric field to inject carriers and also drive them inside the active layer, it is easy for the carriers to find the guest, and thus most of the EL emission occurs from the guest because it has lower first excited state energy level. Therefore, unlike the PL measurements, for EL in OLED, we had to decrease the guest percentage to be able to also see the host emission band. In Figure 3.13, we show the EL emission spectrum of the OLED device at different guest percentage. At guest weight percentage greater than 1%, we see the $Ir(btp)_2acac$ peaks only. At 0.1%, there are weak bands arising from the PFO and these become clearer at 0.05 % (Figure 3.13(d)). The fact that a tiny amount of $Ir(btp)_2acac$ is sufficient to see its emission shows that this host-guest combination has very efficient energy transfer.

After achieving white light OLED (WOLED) spectra, we tried to manipulate the emission color. There are two ways of changing the color in a device: the first is changing the device current density, and the second is applying an external magnetic field. Figure 3.14(a) and (b) show the EL spectra of the 0.05% Ir(btp)2acac in PFO OLED at various current at temperatures 10K and 100K, respectively. As the current increases, the guest emission saturates but the host emission continues to increase which forms blue shift in the device EL emission color. We see a relatively weak PFO emission at low current, while the PFO emission is more intense at higher current. This is more

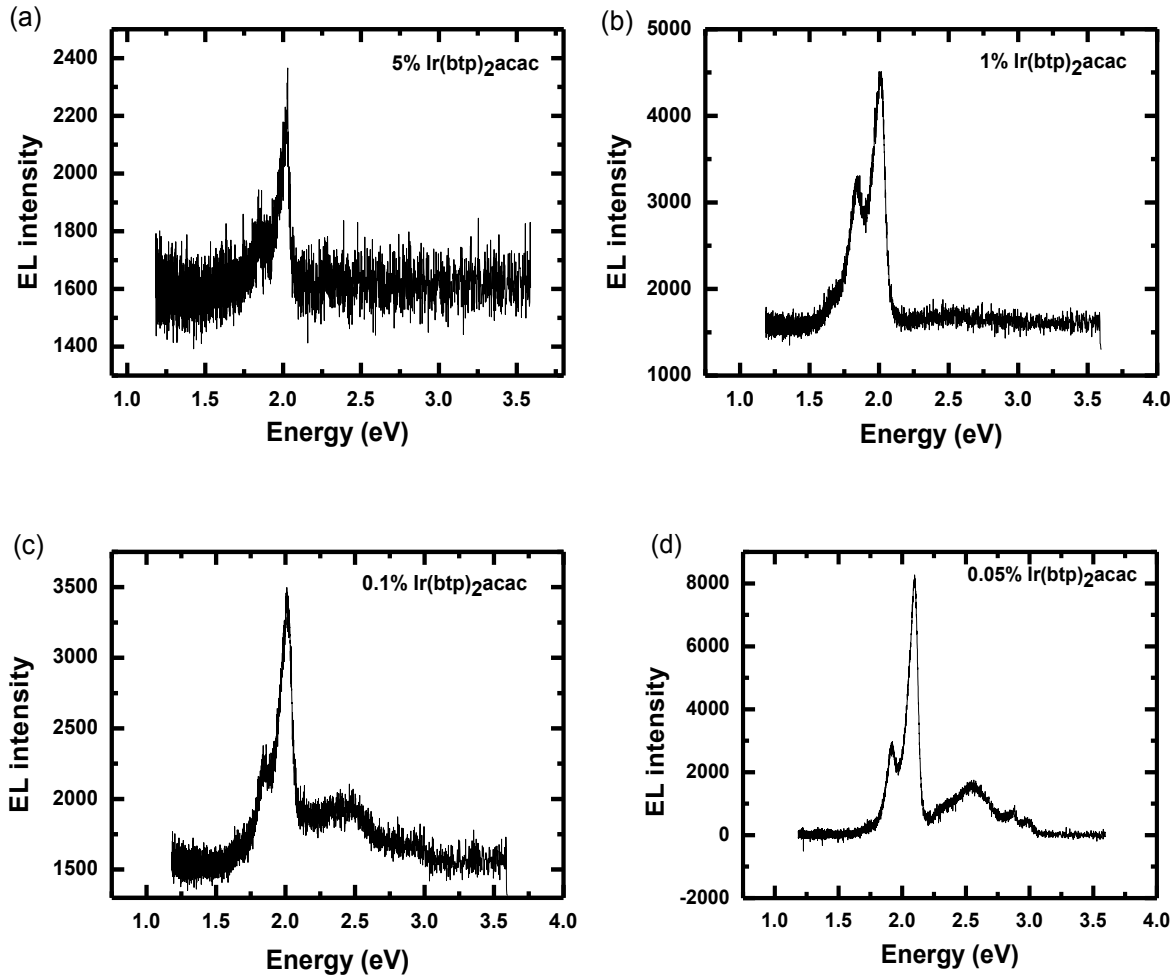

Figure 3.13. EL spectra at (a) 5% (b) 1% (c) 0.1% (d) 0.05% Ir-complex in PFO. The emission band at 2 eV is from the guest molecule, whereas the PFO emission is in the UV. The emission band at 2.6 eV is from an excimer that forms in the host polymer.

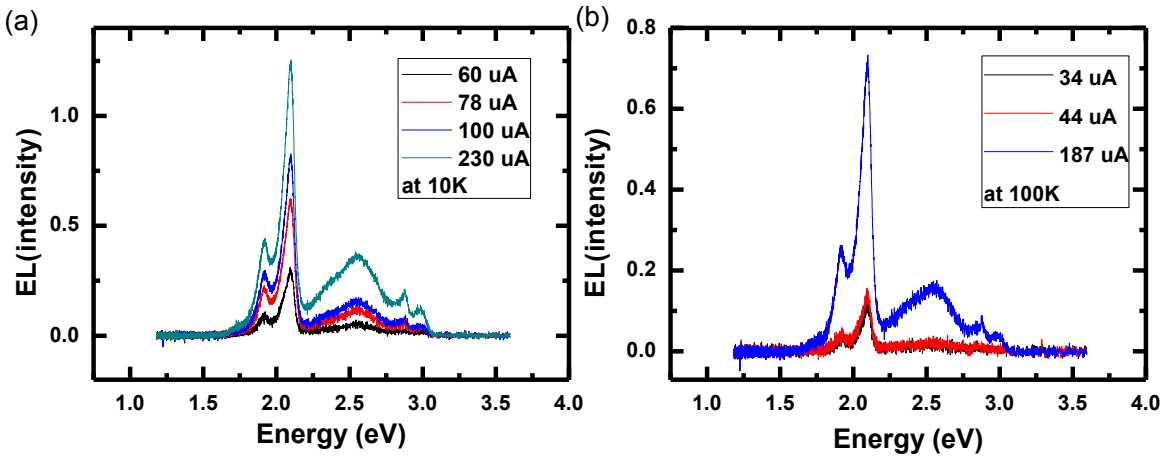

Figure 3.14. EL spectra of 0.05 % of the Ir complex in PFO at different currents at temperatures (a)10K and (b)100K.

clearly seen at 100K (Figure 3.14(b)) that there is almost no emission peak from the host at a current of less than 50 μA, whereas it is significantly pronounced at higher current of 187 μA.

Next, we studied the magnetic field effect in the host-guest device where the guest concentration is 0.02% which enables us to see all the color from PFO, Ir-complex, and the green band ('X') centered at ~2.5eV (Figure 3.15(a)). The origin of 'X' band is still debated in the literature; this EL emission may be due to excimers [94, 95], aggregates [96], or intrachain defects [97, 98]. In any case, it belongs to the PFO host, since it also occurs in pristine PFO-based OLEDs (Figure 3.16(a)). We studied the magnetic field effect at each emission band, as the magnetic field changes the intensity at different peaks by different amounts. The PFO emission band is increased by 2.38% (Figure 3.15(b)), whereas the Ir- band is increased by only 1.58% (Figure 3.15(c)). At the same time, we noticed that the 'X' band has MEL of intermediate value, 2.03% (Figure3.15 (d)). MC(B) of the device also has similar response to that of MEL(B), and its magnitude is 1.90% (Figure 3.15(e)). We therefore conclude that the magnetic field changes the emission intensity by different amount at different regions of the emission spectrum, and this enables emission color control.

To check whether this phenomenon also occurs in OLED based on pristine PFO we measured the MEL in such a device. Figure 3.16(a) shows the EL spectrum of the pristine PFO OLED where PFO emission appears at ~2.8eV and the green broad X-band appears at ~2.5eV. MEL_{max} at ~2.8eV, ~2eV, and ~2.5eV are 1.57%, 1.51%, and 1.59%, respectively (Figure 3.16(b), (c) and (d)). Here, MEL_{max} is approximately the same at different spectral regions of interest, namely, PFO peak, Ir-peak, and 'X' peaks positions

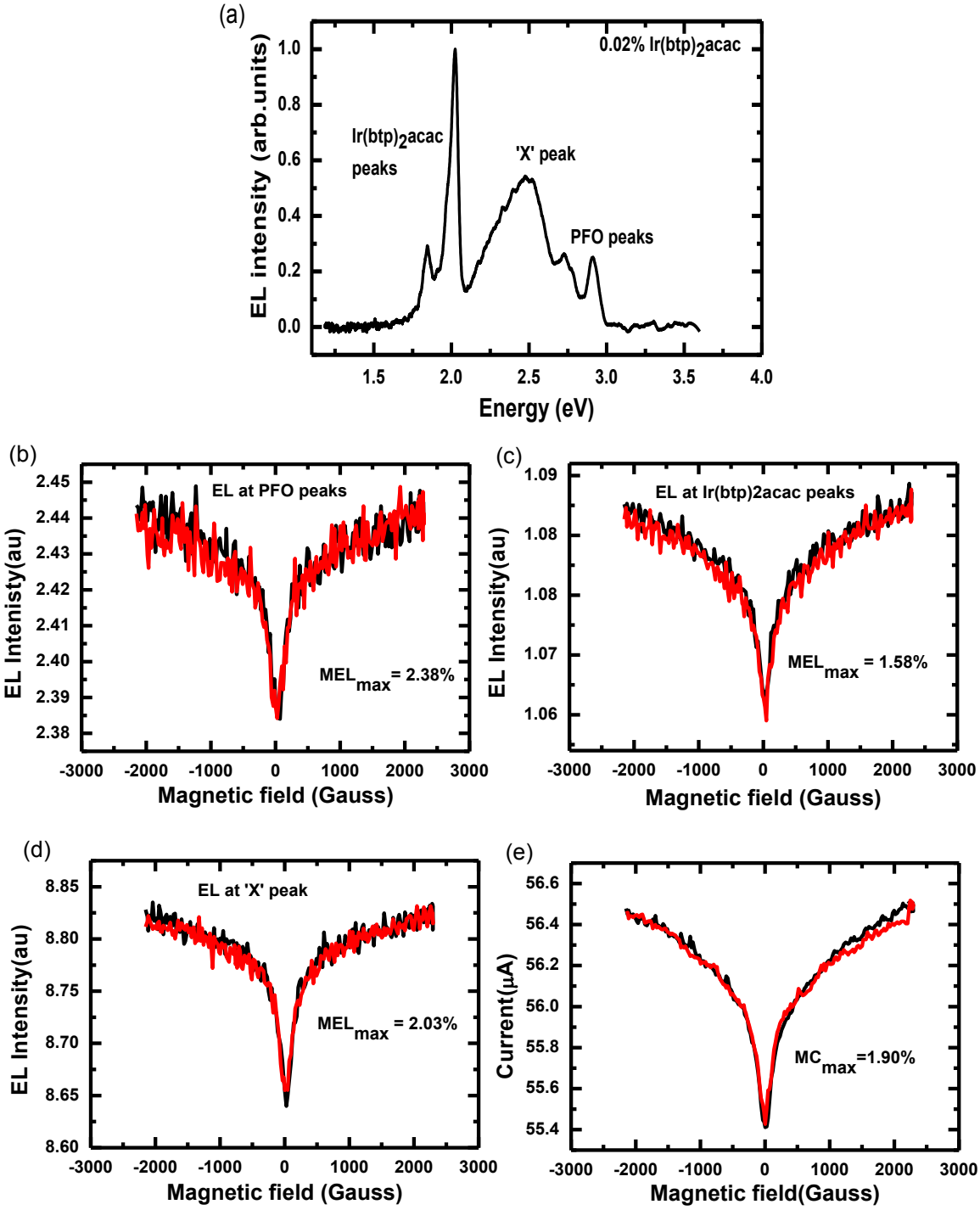

Figure 3.15. Electroluminescence in 0.02% Ir(btp)2acac in PFO device. (a) EL spectrum. MEL(B) response at (b) PFO band; (c) Ir-complex band; (d) 'X' band, and (e) MC(B) response of the device.

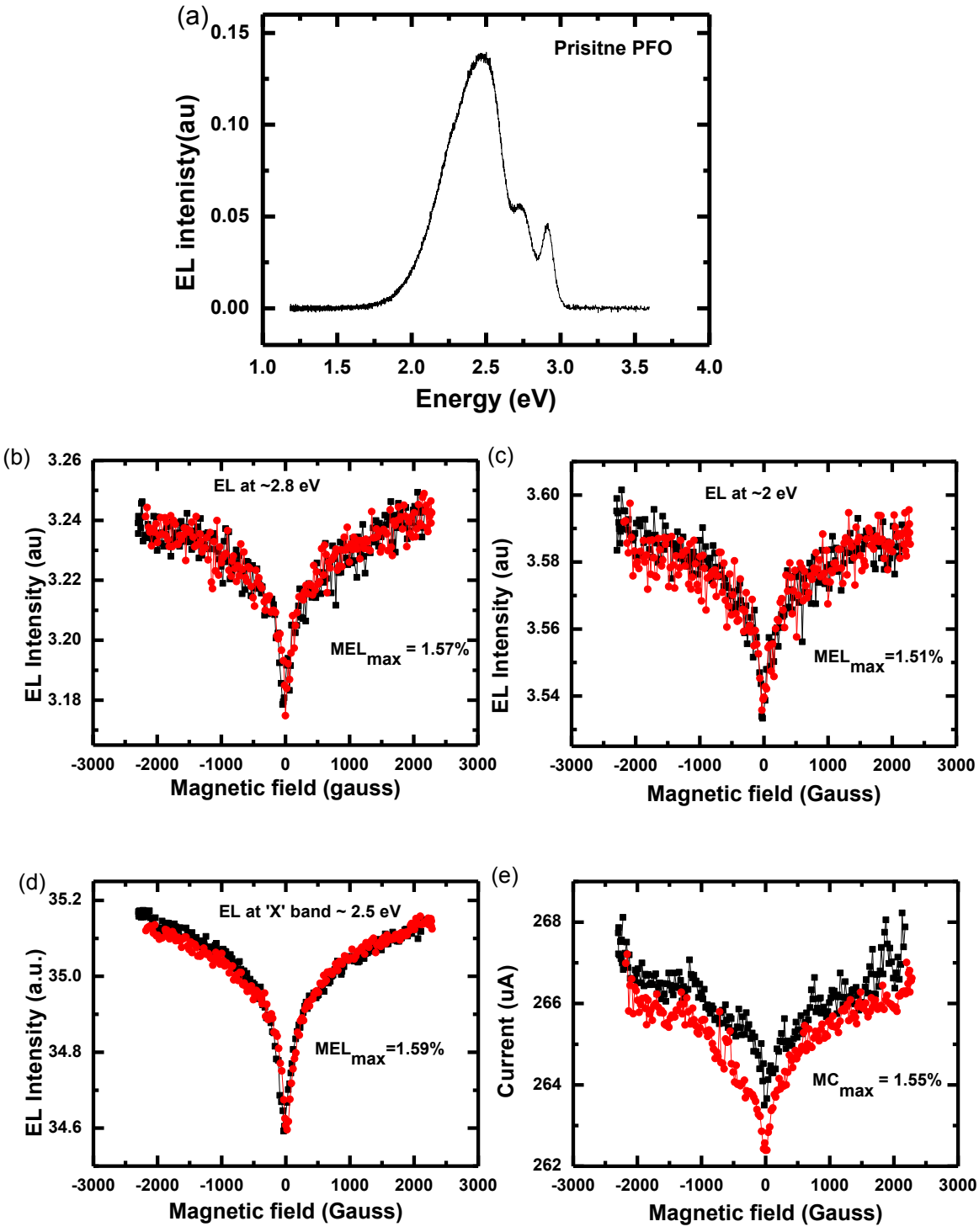

Figure 3.16. Electroluminescence in pristine PFO device. (a) EL spectrum. MEL(B) response at (b) PFO (c) Ir-complex and (c) 'X' band positions; (d) MC(B) response.

which were different in the blend device. We therefore conclude that unlike the blend device, magnetic field does not change the color in the single polymer device. Also, the MC of the device is reported in Figure 3.16(e), and is very close to the percentage change of the EL.

Based on the above MEL and MC response on the blend and the pristine device, we propose the mechanism of magnetic field effect in OLEDs, which is schematically shown in Figure 3.17. In the device, the blue emission is due to EL of singlet excitons in the PFO host, a broad green emission band 'X' is also from the host, and the red band is due to the Ir- complex triplets. At the low guest concentration, triplets of the Ir-complex molecules are populated via Forster and Dexter energy transfer from host excitons S_H and T_H to guest excitons S_G and T_G(S and T stand for singlet and triplet, respectively), whereas the 'X' state is populated directly from the polaron pairs (PP) of the host either in singlet (PP_S) or triplet(PP_T) spin configuration. Singlet excitons in the guest, $S_{G,}$ are converted to triplet excitons in the guest, T_G, via intersystem crossing with a rate $K_{ISC}(G)$. Since the MEL_{max} for different regions in the pristine device is approximately the same and they are different in the blend device, we infer that MEL has two contributions; the first contribution is from the current change via MC(B), whereas the second contribution is from the B-dependent interplay between PP_S and PP_T states in the host. We note that MC is caused by different recombination and dissociation rates(χ_S, $\chi_{T,}$ d_S and d_T) for singlet and triplet polaron pairs. Singlet emission intensifies at the expense of the triplet polaron pair conversion to singlet through MFE, whereas the green emission is not influenced the same way because it contains contributions from both singlet and triplet polaron pairs. Reduction in the number of PP_T causes reduction in the number of T_G

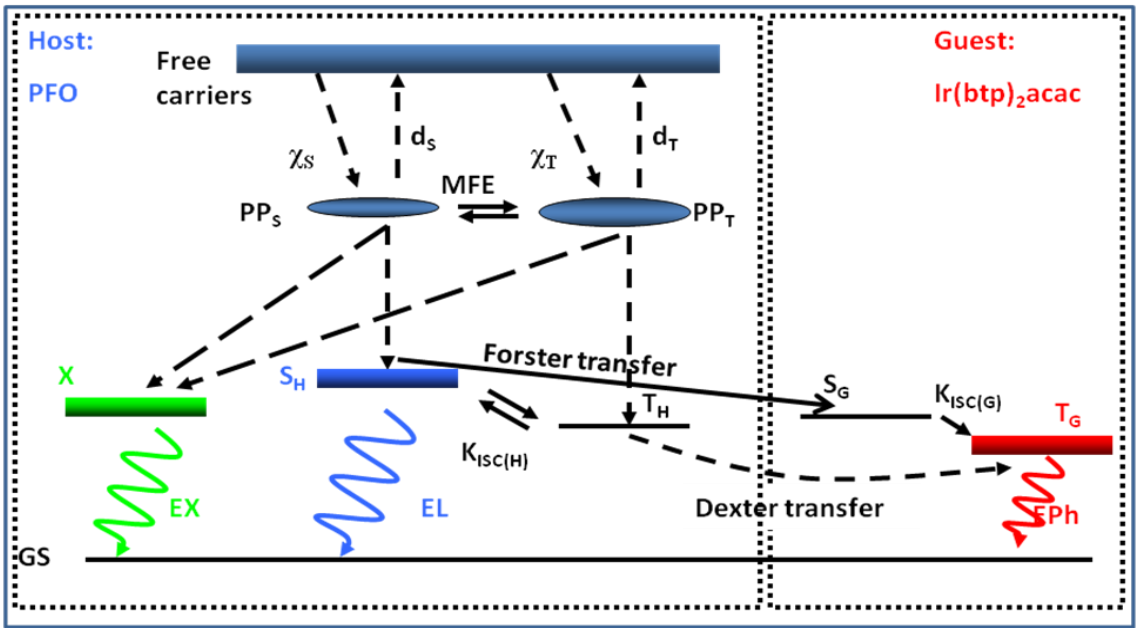

Figure 3.17. Schematic representation of the energy levels and energy transfer pathways in the Ir-complex/PFO blend.

formation that originates from the Dexter energy transfer process. Hence the magnetic field induces PP_T to PP_S conversion *that more directly enhances the fluorescence while diminishing phosphorescence*. This is reflected in our experimental results for a host-guest device where the PFO EL emission band is enhanced respect to the MEL of band X on the expense of the EPH Ir- emission.

We generalize this result of polaron pair mechanism of MFE in OLED in another host-guest system, namely MEHPPV and Pt(tpbp). The EL spectra of the new host guest pair are shown in Figure 3.18. MEHPPV has yellow emission peak at ~2eV and Pt(tpbp) has the red emission at ~1.8eV. Figure 3.18(a) is the pristine MEHPPV and 3.18(b) is the 5% Pt(tpbp) EL spectra. Though the peak at 1.8eV has contribution from MEHPPV vibronic emission, we believe there is large contribution from the Pt-complex because the MEHPPV 0-1 vibronic transition is at ~1.9eV and the MEHPPV emission is falling faster at lower energies. We monitored the MEL at these two different peaks. Figure 3.19(a) is the MEL(B) response response of MEHPPV peak which has MEL_{max} =2.27%, whereas the Pt-peak (Figure3.19 (b)) has a smaller MEL_{max} =1.26%. This difference can be well explained by the above proposed mechanism, where the applied magnetic field increases the PP_S density at the expense of PP_T density which in turn leads to an increase in the MEL value for singlet exciton emission in the host and in parallel decreases the MEL value for triplet emission in the guest. We also note that MC = 0.65% in Figure 3.19(c) causes equal increase in both MEL and MPH in addition of changing their intensities due to interplay between PP_S and PP_T states. We also did the control experiment to determine if this change has contributions from spectral change in MEHPPV after applying magnetic field. Figure 3.19(d)-(f) shows that the magnetic field does not change the PL

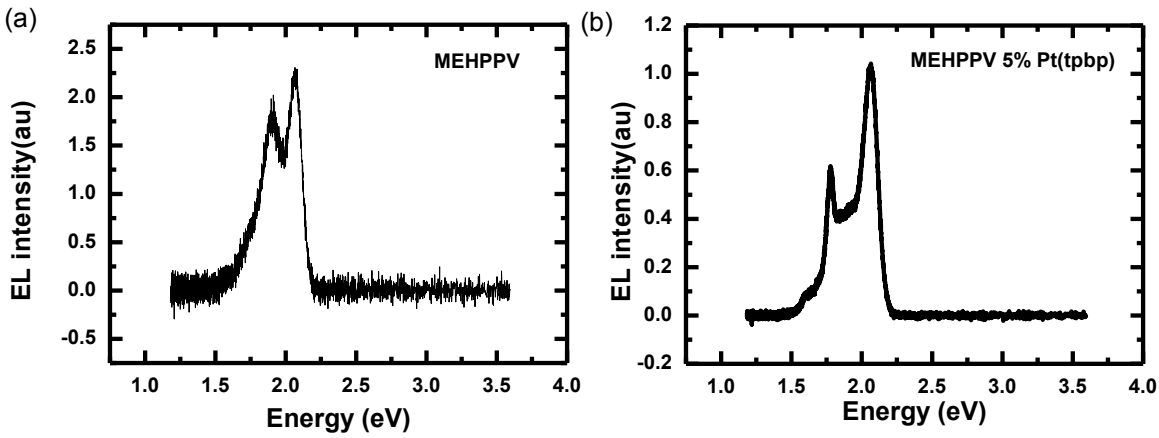

Figure 3.18. EL spectrum of (a) MEHPPV; (b) blend of 5% Pt(tpbp) in MEHPPV.

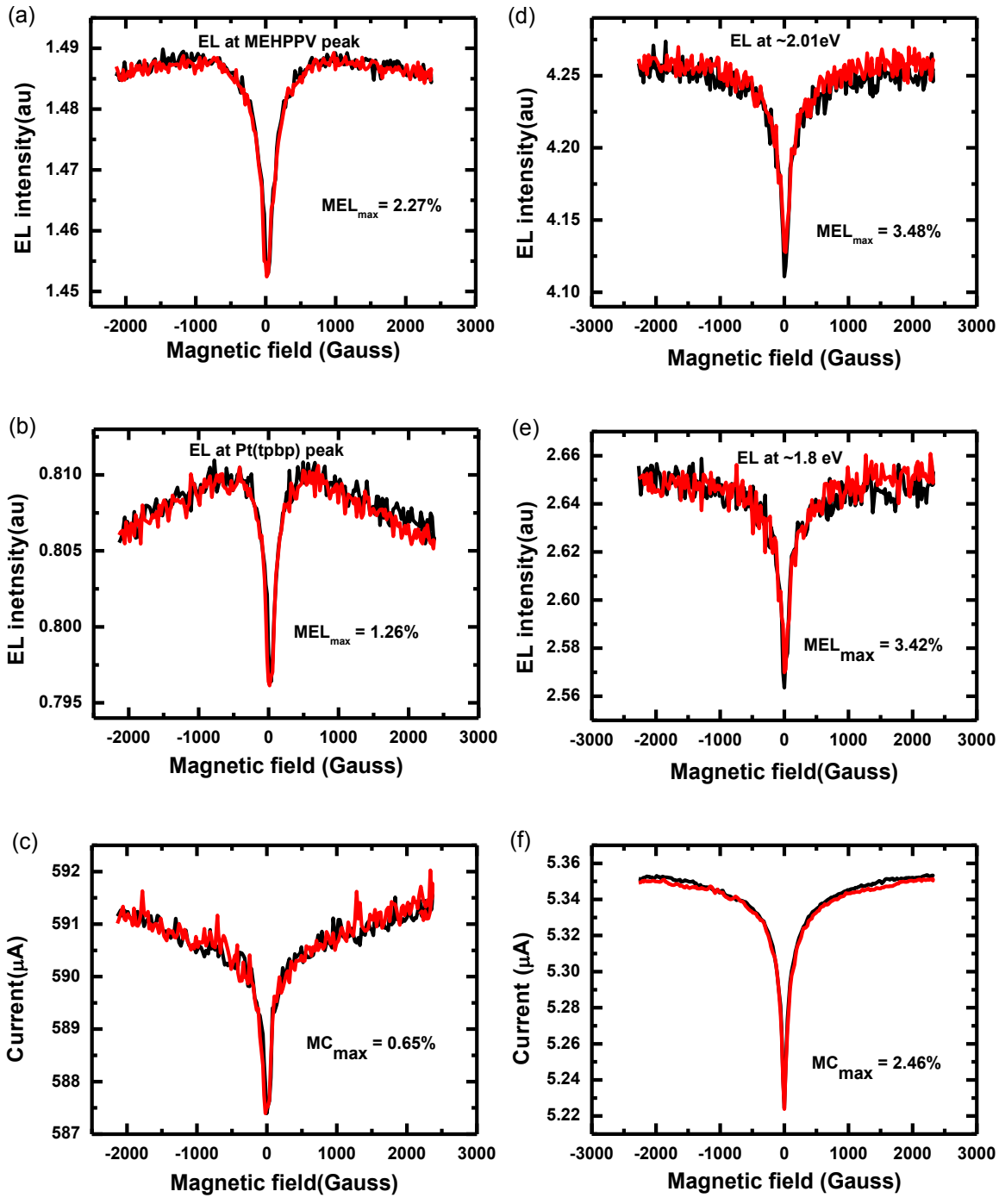

Figure 3.19. MFE(B) response in OLED based on MEHPPV/Pt(tpbp) blend. (a) MEL at 2.1 eV; (b) MEL at 1.8 eV; (c) MC(B) response of MEHPPV/Pt(tpbp). (d)-(f) MFE(B) response in OLED based on pristine MEHPPV.

emission spectrum for pristine MEHPPV; all the various EL emission bands equally increase by ~3.45%, as is shown in Figure 3.19(d) and 3.19(e). We see a positive value of 2.46% for MC in Figure 3.19 (f) which is similar to the MEL maximum value, as expected.

Similar to PFO-Ir complex, the MEHPPV-Pt complex also shows color manipulation by an external magnetic field in the blend system. The magnetic field reduces the triplet polaron pair densities that results in an increase of the singlet polaron pair densities. Reduction of the triplet pair density is observed in the phosphorescent emission of the additive molecules, which are populated via energy transfer from the host. We cannot observe it in OLED based on pristine polymers since we cannot directly detect the triplet densities because the triplet emission is forbidden (unless there is strong SOC that mixes the triplet and singlet characters).

3.3.4 Conclusions

Host-guest blend OLED devices have the advantage of generating broad band white light as compared to single polymer OLED. Here, with the suitable combination of the materials (i.e. matching the emission spectrum of the host to the absorption spectrum of the guest), we showed white OLED in a single layered device. Moreover, we have explored the possibility of color tuning in such blended devices via the magnetic field effect, in addition to the current-induced color change. Furthermore, we showed that the underlying mechanism of this color change is the polaron pair mechanism of MFE in OLEDs.

3.4 Room-temperature Magnetically-modulated Electroluminescence from Hybrid Organic/ Inorganic Spintronics Devices

3.4.1 Introduction

Organic semiconductors research has largely been motivated by optoelectronic device applications which include OLEDs [27, 99] , light emitting field effect transistors [100], and photovoltaic cells [101]. Recently, organic spintronics devices such as organic spin valves (OSV) [6] and spin-OLED [102] have been demonstrated at low temperatures. In spite of this interest surge in spin-related organic devices [33, 55, 103-105], the quest of spin manipulation that results in electroluminescence (EL) control at room temperature (RT) has not been achieved yet, although it has been consistently tried. The main obstacles in realizing this goal are the large resistance mismatch between the ferromagnetic (FM) electrodes and the organic layer in such a device, the shortcoming of carrier spin diffusion length, and limitation of spin-polarized carrier injection from suitable FM electrodes at RT. For example, by inserting an insulator buffer layer (i.e. Al_2O_3) between the FM electrode and organic layer in an OSV, a very small transport magneto-resistance, MR (~0.15%) was obtained at RT [106]. Although tunneling MR (TMR) using an OSV with very thin organic interlayer has been successful (showing TMR up to ~6% at RT) [107], this device is passive, namely it lacks electro-luminescence (EL) emission, which is one of the main reasons that organic spintronics has been intensively studied so far. The same problem applies to inorganic magnetic tunnel junctions (MTJ), which show a significant magneto-resistance at RT

(MR>80% [108-111]), but, on the other hand, these devices do not exhibit EL emission.

In parallel with the recent advances in organic spintronics devices, the magnetic field effect (MFE) such as magneto-conductance (MC) and magneto-EL (MEL) in nonmagnetic OLEDs has been also intensively explored [48, 112]. The organic MFE poses a significant scientific puzzle since it is one of only few known examples of large bulk MR in nonmagnetic materials at RT; thus its underlying mechanism has been intensely debated [37, 38, 49, 64, 90, 113, 114]. However, the organic MFE response is controlled by the internal spin interactions in the active layer, and apparently is enhanced when the organic layer is subjected to UV light illumination, or electron beam bombardment [87]. The latter conditions are detrimental for OLEDs operation at high EL intensity. In addition, the sign of MFE in OLEDs may change unexpectedly according to the device 'history' of operation [86].

In the present work, we introduce an approach that leads to giant MR and MEL in organic devices at RT, based on hybrid organic/inorganic spin-OLED (dubbed here h-OLED). The h-OLED device combines the advantages of an inorganic MTJ device having high MR at RT that can be easily integrated with an OLED having efficient EL emission, flexibility, and low production cost. This method is universal, meaning it can be applied to many OLEDs based on small molecules, polymers, or blends, giving electro-phosphorescence (EPH) or EL emission, respectively. These hybrid devices show significant (up to ~80%) MEL at RT that covers the entire visible spectral range, namely red, green, blue, as well as white emission.

3.3.2 Experimental

Figure 3.20 shows the hybrid device architecture and its operation scheme. The h-OLED device contains two sections: the inorganic MTJ and OLED components, respectively, which are connected in series; these components may be close to each other, or far apart. The devices for the MTJ component were fabricated using a shadow mask technique via DC magnetron and ion beam sputtering onto thermally oxidized silicon substrates. We used a MgO tunnel barrier in between CoFeB and CoFe ferromagnetic (FM) electrodes, where the CoFe electrode is deposited onto a thin CoFeB layer, and an IrMn layer which is an antiferromagnet (AFM). This type of MTJ yields the best TMR performance at RT (~ 50% to 600%), with an extended *B*-interval of antiparallel electrode magnetization directions [108-111]. In turn, the OLED component is a traditional device composed of indium tin oxide (ITO, purchased from Delta Technologies)/hole transport layer (PEDOT:PSS)/organic semiconductor chromophore/calcium (Ca)/aluminum (Al). The organic interlayer chromophore may be based on any molecule, polymer, or polymer/molecule (host/guest) blend with high EL emission yield. The π-conjugated polymer polyfluorene (PFO) and poly[2-methoxy-5-(2-ethylhexyl-oxy)-1,4-phenylene-vinylene] (MEH-PPV) were purchased from American Dye Source, Inc. The deuterated poly(dioctyloxy)phenylvinylene (D-DOO-PPV) was synthesized in house [55]. The π-conjugated small molecule tris-Alq_3 was purchased from Sigma Aldrich. The red dopant molecule "Bis(2-(benzo[b]thiophen-2-yl) pyridine-N,$C^{3'}$)(acetylacetonate) iridium(III)" ($Ir(btp)_2acac$) was purchased from Rubipy Scientific Inc. The polymer film thickness was varied by using different concentrations of the solution (5–20 mg/ml) and spin casting speeds (2000 to 8000 rpm). The molecule layer

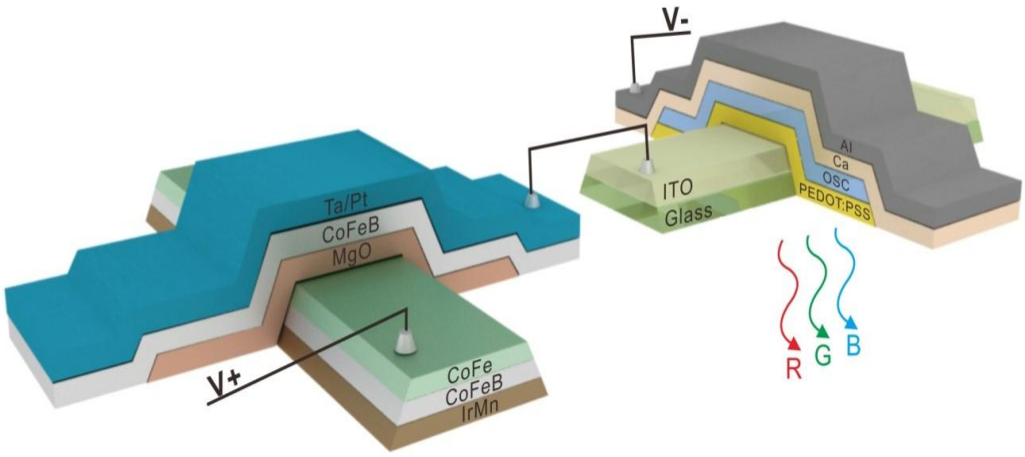

Figure 3.20. Hybrid organic/inorganic spintronics device structure and operation scheme. The hybrid device is composed of two components: the inorganic magnetic tunnel junction (MTJ; left) and OLED (right).

was grown by thermal evaporation in a vacuum deposition chamber with base pressure of 10^{-6} Torr, followed by a Ca cathode (25 nm) capped by an Al film (80 nm). Typical device area was $1\times1mm^2$, and typical thickness varied between 50-200 nm. During operation, the h-OLED device was biased at constant voltage, *V*, and an in-plane sweeping magnetic field, *B*, was applied to the MTJ. Upon sweeping *B* the MTJ resistance R_1 switches from 'low resistance' (P) to 'high resistance' state (AP) (and vice-versa when sweeping *B* in the other direction), thus changing the current density in the OLED component. This, in turn dramatically modulates the EL emission intensity, even though the OLED resistance is much larger than that of the MTJ. We define the MEL(*B*) response by the relation: MEL(*B*)≡[EL(*B*)-EL(AP)]/EL(AP), whereas the MC(*B*) response is obtained from: MC(*B*)≡[I(B)-I(AP)]/I(AP)).

3.3.3 Results and Discussion

A typical TMR(*B*) response of the MTJ device at *V*= 65 mV at RT is shown in Figure 3.21(a). TMR(*B*) exhibits an abrupt resistance change at the coercive field B_{c1}~1 mT of the top (CoFeB) FM electrode, and at $B_0=J\pm B_{c2}$~50 mT for the bottom electrode (CoFe/CoFeB/IrMn), where *J* is the anisotropy exchange coupling between the AFM and the FM layers [108, 109]. The obtained TMR maximum, TMR_{max} [= $(R_{AP}-R_p)/R_P$] is ~75%, and depends weakly on *V*. Importantly, we note the MTJ Ohmic *I*-*V* response at small bias voltage used here, which is determined by the small voltage drop on the MTJ section (~65 mV). Figure 3.21(b) shows the *I*-*V* and EL-*V* typical responses of a MEH-PPV-based OLED obtained at RT. The OLED *I*-*V* response contains two voltage regimes: an Ohmic regime with constant resistance $R_2\approx600$ MΩ, and a space-charge-

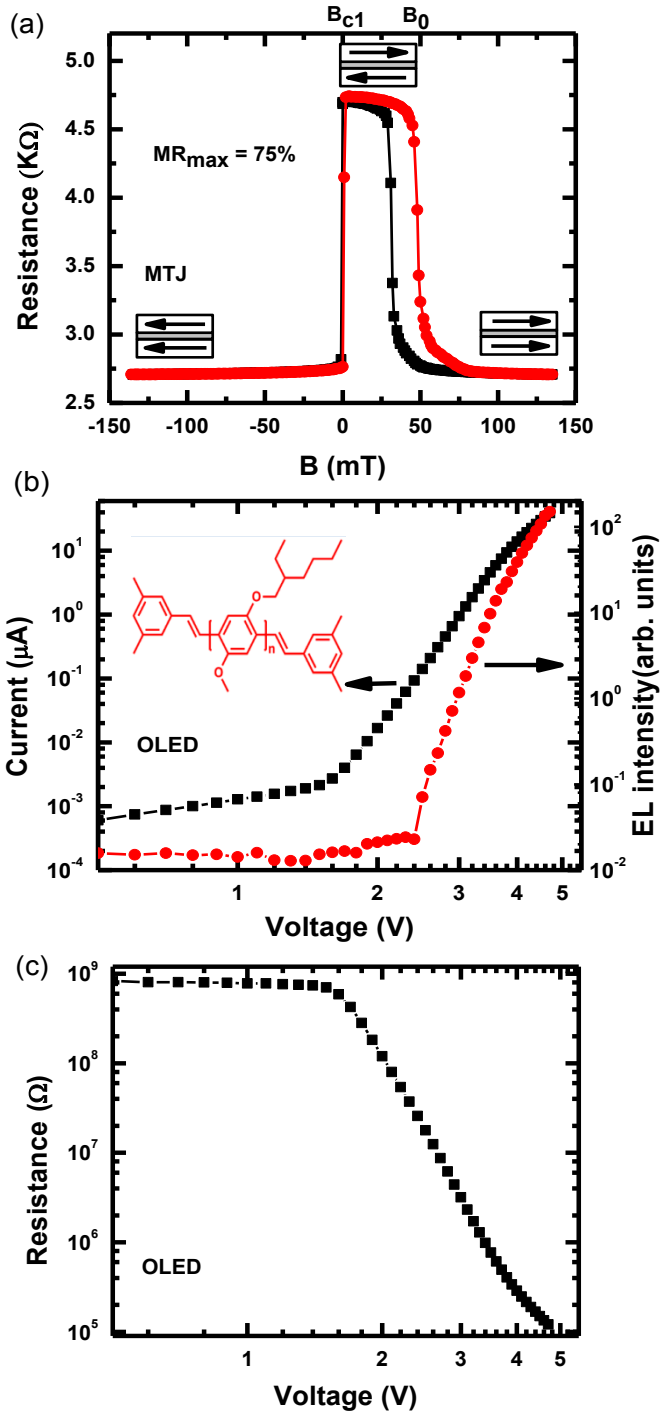

Figure 3.21. Inorganic MTJ and OLED. (a) Tunnel magneto-resistance (TMR(B)) response of the MTJ at V=65 mV and RT. The red (black) line denotes TMR upon increasing (decreasing) B. The respective parallel (P; for $B>Bc_1$, B_0) and antiparallel (AP; for $Bc_1<B<B_0$) electrode magnetization configurations are shown. (b) Typical I-V and EL-V responses of a MEH-PPV-based OLED plotted on logarithmic scales. The inset shows the MEH-PPV polymer repeat unit. (c) The OLED R-V response plotted on logarithmic scales.

limited current (SCLC) regime. In this SCLC regime,

$$I = aV^n \tag{3. 12}$$

$$R_2 = \frac{V}{I} = \left(\frac{1}{a}\right) V^{-n+1} \tag{3. 13}$$

where, 'a' is a constant and n ≥ 2 is the power dependence of the current with the voltage. Fitting this equation in Figure 3.21(c) gives n = 5.8. Here, device resistance, R_2, drops as a power law in V ($\sim V^{(n-1)}$) down to ~120 kΩ at ~ 4.7 Volt (Figure 3.21(c)). The three orders of magnitude drop in the OLED resistance is very significant, and points to the advantage of realizing relatively large MR values in bipolar OSV devices in the SCLC regime, as recently demonstrated for a spin-OLED [102].

When the two device components, namely the MTJ with resistance R_1~4.7 kΩ and OLED with resistance R_2~120 kΩ are connected in series at 4.7 Volt, it seems that the TMR change, ΔR_1 = 2 kΩ (from R_P of 2.7 kΩ to R_{AP} of~4.7 kΩ; Figure 3.21(a) achieved with *B* applied on the MTJ component would barely affect the total resistance of the hybrid device, because of the large ***resistance mismatch*** between R_1 and R_2 at this operating voltage. Indeed, if the OLED were Ohmic, we would expect maximum magneto-current, $MC_{max} = \Delta I/I = -\Delta R_1/(R_1+R_2) \approx 1.6\%$ at V~4.7 Volt. However, as seen in Figure 3.22(a), we obtain $MC_{max} = \Delta I/I \approx 8.8\%$ for this h-OLED, which is a factor of ~5 larger than anticipated. This 'MR amplification' comes about because the OLED resistance, R_2 is not constant, but depends on V (or I) due to the nonlinear I-V response of the device. In this case, for h-OLED in series combination,

$$V = I(R_1 + R_2) \tag{3. 14}$$

Since applied voltage V is constant and OLED resistance depends on I or V according to

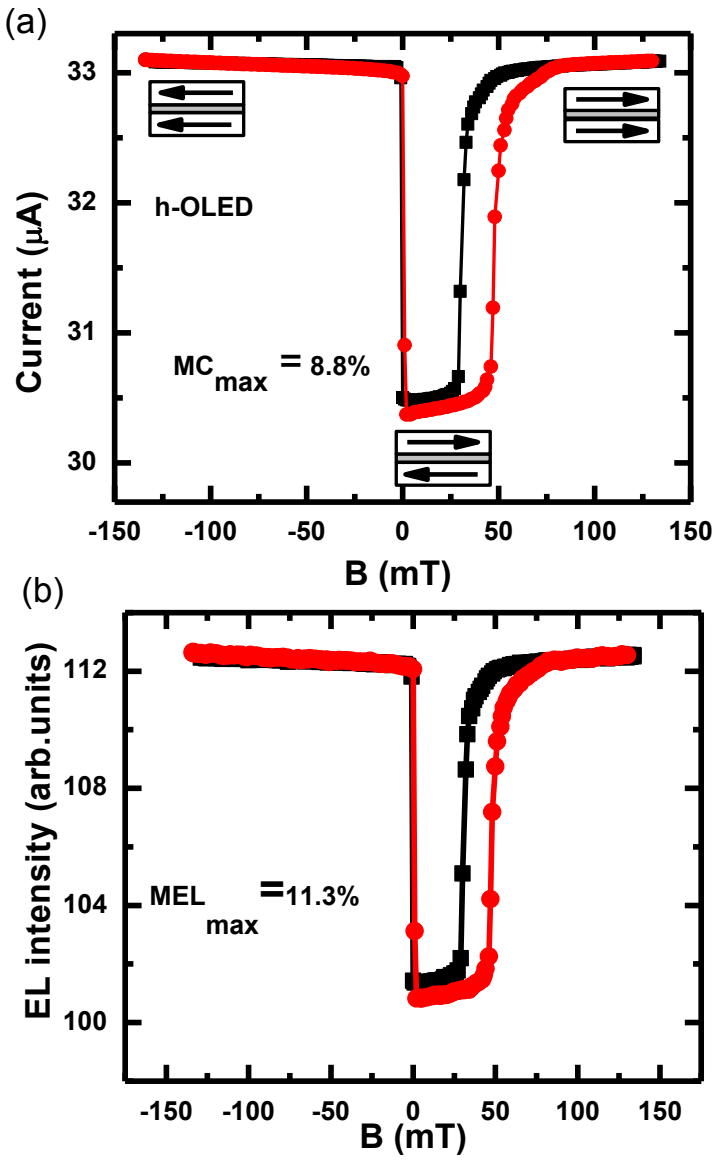

Figure 3.22. MC and MEL in h-OLED. (a) MC and (b) MEL responses of the hybrid-OLED measured at V=4.7 Volt and RT. The maximum MC value, MC_{max}, and MEL value, MEL_{max} are denoted.

Eq. (3.13), differentiating Eq. (3.14) and setting ΔV = 0 for the device operating at constant voltage gives,

$$\Delta V = \Delta I(R_1 + R_2) + I(\Delta R_1 + \left(\frac{dR_2}{dI}\right)\Delta I) \quad (3.\ 15)$$

$$\frac{\Delta I}{I} = -\Delta R_1/(R_1 + R_2 + \frac{IdR_2}{dI}) \quad (3.\ 16)$$

Here, IdR_2/dI can be evaluated using Eq. (3.13) as,

$$\frac{IdR_2}{dI} = \left(\frac{1}{n} - 1\right)R_2 \quad (3.\ 17)$$

Combining Eq. (3.16) and (3.17),

$$\frac{\Delta I}{I} = -\Delta R_1/(R_1 + \frac{R_2}{n}) \quad (3.\ 18)$$

This explains the underlying mechanism of the obtained 'MR amplification' (Figure 3.22(a)); it is due to the OLED nonlinear *I-V* response which effectively reduces R_2 contribution to the MR by a factor n (>1). We conclude that under SCLC operation, the resistance mismatch between the two device components is not as severe as anticipated for an Ohmic R_2. Specifically, we can fit the obtained 'MR amplification' in Figure 3.22(a) using n≈5.9, which is in good agreement with the measured exponent of the OLED *I-V* response in the SCLC regime (see Table 3.1, and Figure 3.21(b)). Figure 3.22(b) shows the MEL(*B*) response of the same h-OLED device, also measured at *V*=4.7 Volt and RT. It is seen that MEL(*B*) response follows that of the MC(*B*). There are sharp MEL increases at B_{c1} and B_0. Also, the maximum MEL, MEL_{max}=11.3% is higher than MC_{max}, which may be explained by the nonlinear EL-*V* response (Figure 3.21(b)). This shows that the h-OLED device may deliver substantive MEL at RT, which has been one of the long-sought goals of the organic spintronics field.

Table 3.1: Summary of the various studied h-OLED devices in this work. The OLED resistance, R2, and the I-V characteristic exponent, n (in the $I \sim V^n$ response), refer to the OLED component. The operational bias voltage, V_{oper}, MC_{max}, and MEL_{max} refer to the entire device.

OSC	**Color**	**R_2 (kΩ)**	**$n_{(I-V)}$**	**V_{oper} (V)**	**MC_{max} (%)**	**MEL_{max} (%)**
D-DOO-PPV	Red	60	17.5	2.13	34	81
Alq_3	Green	119	3.3	3.3	5.7	31
MEH-PPV	Red	121	5.8	4.7	8.8	11.3
PFO	Blue	176	8.3	5.2	6.3	9
PFO 0.02% Ir	White	201	3.7	6.0	3.7	4.9
LED	Red	58	27	1.78	43	91

In principle, the h-OLED device may be used at any temperature, with any OLED system having EPH or EL emission (or both), based on small molecules or polymers, and thus may span the entire visible spectrum. To demonstrate this, we introduce three h-OLED devices that show giant MEL at RT with emission bands in the red (Figure 3.23(a); D-DOO-PPV polymer), green (Figure 3.23(b); Alq_3 molecule), and blue (Figure 3.23(c); PFO polymer), which cover the entire visible spectrum; in all cases, *B* was applied simultaneously on both h-OLED components. The polymer repeat units and Alq_3 molecular structure are given in the respective Figure 3.23 panel insets. A summary of the h-OLED device characteristics, operating voltage, exponent n, and obtained MC_{max} and MEL_{max} values are given in Table 3.1. Consistent with Eq. (3.16), we clearly see that the h- OLED performance is enhanced when the mismatch between R_1 (MTJ) and R_2

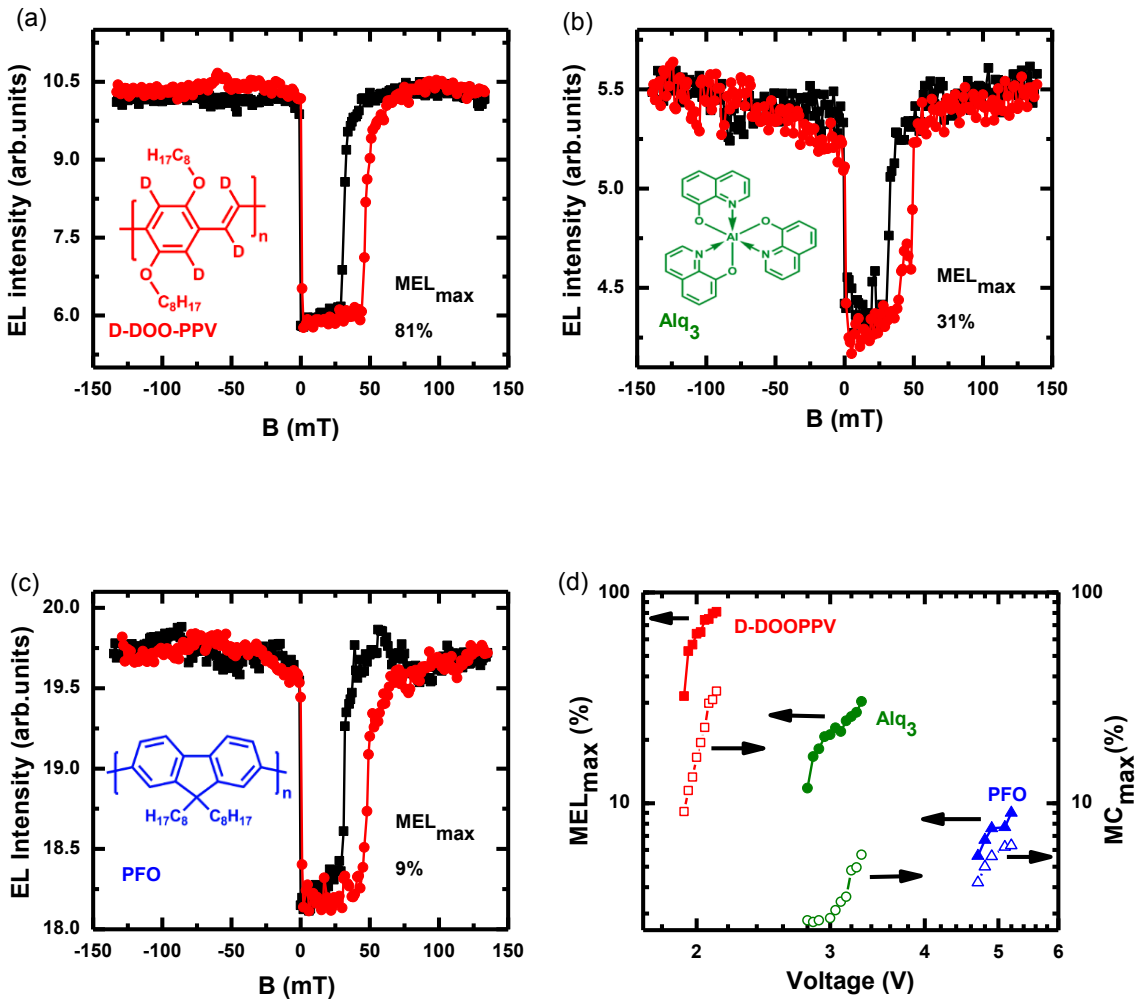

Figure 3.23. MEL(B) response of three h-OLED devices at RT. The devices are based on (a) D-DOO-PPV with red emission; (b) Alq3 with green emission; and (c) PFO with blue emission. The red (black) lines are MEL(B) obtained upon increasing (decreasing) B. The D-DOO-PPV polymer repeat unit (red), Alq3 structure (green) and PFO polymer repeat unit (blue) are shown in the corresponding insets of panels, respectively. (d) MEL_{max} and MC_{max} of the three devices vs. the applied voltage, V plotted on logarithmic scales.

(OLED) at the operating voltage is reduced, or when the exponent, n in the *I*-*V* response is large. As in Figure 3.22(b), the obtained MEL(*B*) response of the three devices follow that of the MC(*B*) response, showing abrupt changes at B_{c1} and B_0, and $MEL_{max}>MC_{max}$ (Table 3.1). In particular, the room-temperature MEL(*B*) response of the h-OLED based on D-DOO-PPV (Figure 3.23(a)) shows giant MEL_{max} of ~81%, which is very promising indeed. In Figure 3.23(d), we plot the obtained MEL_{max} and MC_{max} of the three h-OLED devices vs. the bias *V*. It is seen that both MEL_{max} and MC_{max} strongly increase with *V* (or *I*). This can be explained since the OLED device resistance decreases with *V*, and this further decreases the resistance mismatch between the two h-OLED components. Alternatively the denominator in Eq. (3.16) decreases with *I*, and this causes a MC (MEL) increase with *V*.

A "white" h-OLED was also fabricated based on a host/guest blend of PFO mixed with 0.02% $Ir(btp)_2acac$ molecules, in which the PFO (host) shows blue fluorescence and green luminescence, whereas the Ir-complex (guest) has red phosphorescence emission [115, 116]. The EL spectrum reveals three distinct bands across the visible spectrum, and thus the OLED may be considered to be a 'h-WOLED' (see spectrum, inset of Figure 3.24(a)) [117]. MEL(*B*) response shows the changes of the intensity up to 4.9% at RT. Additionally, as indicated by Eq. (3.16), because the OLED has a nonlinear *I*-*V* response in the SCLC regime, it imposes "MR amplification", and consequently, the EL emission could be readily modulated magnetically. In fact, the concept of "hybrid" technology may be expanded to include inorganic LEDs. Figure 3.24(b) shows the MC(*B*) and MEL(*B*) responses of a conventional inorganic LED device connected to the same MTJ leading to an h-LED. The abrupt change of MC(*B*) due to "MR amplification" also yields giant

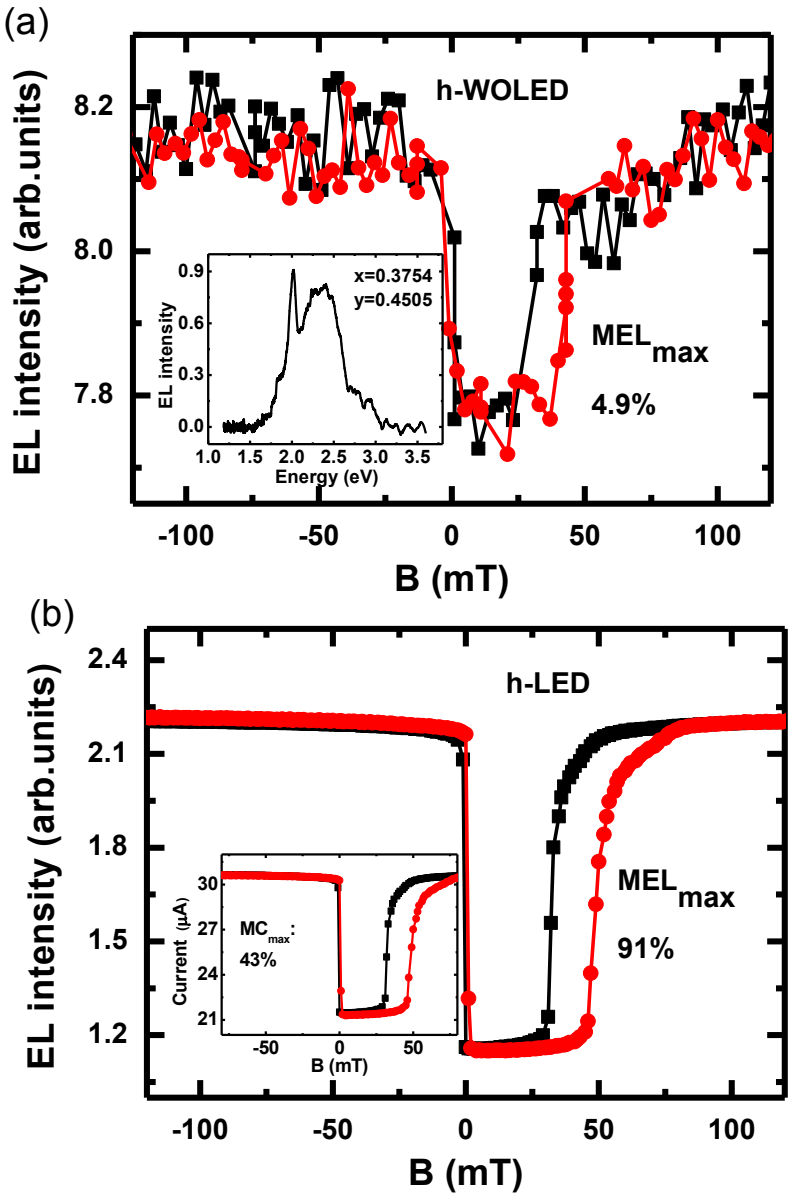

Figure 3.24. MFE response of h-WOLED and h-LED. (a) MEL(*B*) response of a h-WOLED devices based on host/guest blend: PFO polymer doped with 0.02 wt% $Ir(btp)_2acac$ molecules. The inset shows the emission spectrum and its coordinates based on CIE (1931) chromaticity diagram. (b) MEL(*B*) and MC(*B*) response of a h-LED devices based on an inorganic LED. The red (black) lines are MEL(*B*) obtained upon increasing (decreasing) *B*.

$MEL(B)_{max}$ up to 91% (see Table 3.1).

3.4.4 Conclusions

In summary, we conclude that the large resistance mismatch between MTJ and OLEDs that has been considered a bottleneck for organic-based devices is suppressed due to the nonlinear *I-V* response of the OLED component in the SCLC regime. The "MR amplification" principle discussed here suggests a method to circumvent the well-known 'resistance mismatch' between FM injector and organic diodes that prevents large MR values in OSV. Our studies show that working in the SCLC regime may improve OSV operation.

The hybrid OLED device with magnetic field controlled EL emission at room temperature has the potential for a myriad of applications due to its unique advantages. One of the principal advantages is in organic (or inorganic) displays, where the EL emission may be controlled by an external magnetic field, providing another operational mode for controlling the device EL intensity. In this regard, the magnetic field-modulated EL emission can be engineered to be in a remote operational mode, where the field acts on one section of the device (the MTJ) and the EL emission comes from the emissive section. It provides a way for integrating inorganic MTJ arrays for modulating the EL intensity of a large area display based on OLEDs (or LEDs). Furthermore, we note that for h-OLED (or h-LED) devices the EL intensity at $B \sim 0^+$ is at a minimum, since the FM magnetizations are have AP configuration. Consequently, a relatively small B (~1mT) increase in the opposite direction may abruptly enhance the EL intensity. Compared to the conventional, more direct bias voltage or current-modulation, similar

change of the device EL intensity requires a much larger current change. We thus conclude that the magnetically controlled h-OLED (or h-LED) device may consume significantly less driven power and perform a more rapid and sensitive EL switch. These properties and the large obtained MEL_{max} at RT, when taken together, indicate that the hybrid MTJ/OLED (or MTJ/LED) technology may be readily available for immediate commercial applications.

CHAPTER 4

ORGANIC PHOTOVOLTAICS

4.1 Introduction

Organic photovoltaic (OPV) is an emerging field that has seen a rapid development in recent years because of the low cost, flexible device structure, and easy fabrication processes [118-120]. In response to the lower power conversion efficiency (PCE) of the organic bilayer photovoltaic [15] where donor (D) and acceptor (A) layers are deposited sequentially, the scientific community has made promising developments with Bulk Hetero-Junction (BHJ) structures [4, 121], where bicontinuous interpenetrating network of D-A domains are formed. BHJ photovoltaic maximizes the photon absorption from its thick layer of D-A film, and allows the photogenerated singlet excitons to reach to the donor-acceptor interface before they disappear by recombination [122]. In a typical BHJ structure, D-A blends are spin-coated on a cleaned substrate and sandwiched between the electrodes with appropriate electron and hole transport layers [123]. Although there has been a significant increase in PCE by taking advantage of the versatility of synthesis of organic polymers [21, 124-126], the progress is still not good enough to make OPV viable for practical applications, and the complex mechanism of charge dissociation at the D-A interface is still under debate. There has been significant progress in the synthesis of new materials to harvest the infrared solar illumination by

widening the absorption range using low bandgap polymers [126, 127], optimizing the donor/acceptor ratio and the organic active layer thickness [128], using suitable transport layers and the electrodes [129, 130], improving morphology [19], and employing the tandem cell architecture [118, 131]. Compared to the 5% PCE [132] reported for most studied polymer/fullerene blend of regio-regular poly(3-hexylthiophene) (P3HT)/ 1-(3-(methoxycarbonyl)propyl)-1-phenyl)(6,6)C_{61} (PCBM), PCE of 10.6% in tandem OPV cell has been reported [118].

The ideal polymer solar cell in a BHJ structure should exhibit the following set of physical properties: a broad absorption with high coefficient in the solar spectrum to efficiently harvest solar energy, a bicontinuous network with domain width within twice that of the exciton diffusion length, and high donor-acceptor interfacial area to favor exciton dissociation and efficient transport of separated charges to the respective electrodes [133]. Upon the solar light absorption by the polymer, singlet excitons are formed and dissociated by a charge transfer process at the D-A interface [24], leading to either long-range charge separation or the formation of bound interfacial charge transfer state(^{1}CT) [21]. The charge-transfer state, initially in a singlet state, may transform to triplet ^{3}CT state, recombine to the ground state, or separate into coulombically bound polaron pairs (PP) having a relatively long lifetime. The PP may dissociate, and consequently generate free carriers that are collected at the electrodes producing current in the circuit. The large number of ^{3}CT states, statistically 3:1 ratio of ^{3}CT to ^{1}CT population, may be formed following the PP or free carrier recombination. If the ^{3}CT state has higher energy than the polymer triplet state (T_1), which is usually the case in blends of low bandgap polymers [134], and the dissociation rate is smaller, then the

relaxation of ^{3}CT to T_1 in the polymer may occur. Though this loss is realized as the major loss in OPV performance, and several methods are employed to avoid it, reducing the ^{3}CT state density by spin manipulation has been largely ignored so far.

In this work, we demonstrate a method to minimize the triplet loss in OPV. In our previous work, we have successfully reported the PCE enhancement in P3HT/PCBM device by 18% after adding the spin ½ free radical, galvinoxyl (2,6-di-t-butyl-α-(3,5-di-t-butyl-4-oxo-2,5-cyclohexadien-1-ylidene)-p-tolyloxy) in the blend [128]. Here, we report a low bandgap polymer, PTB7 (fluorinated poly-thienothiophene-benzodithiophene) blended with PC60BM that shows superior OPV performance after adding galvinoxyl spin ½ radicals. PTB7 is a low bandgap polymer which contains alternating thienothiophene (TT) and benzodithiophene (BDT) blocks (molecular structure shown in Figure 4.1 inset) in each repeat unit, and yields high PCE of >7% in OPV cells based on this polymer [123]. Because of the electron affinity difference between the alternating blocks, these new copolymers have in-chain charge transfer characteristics that enhance broad absorption in both the UV/vis and near-IR regions [135]. Through detailed optical and electrical studies of the pristine polymer and its blend with PCBM fullerene in OPV devices and the films, we identified that the spin ½ radical facilitates CT states intersystem conversion from triplet to singlet contributing to the current generation which is verified by increase in short-circuit photocurrent density (J_{sc}). This idea is further supported by our experimental results on the reduction in the polymer triplet state measured optically by photo-induced absorption (PA) spectroscopy. We also strengthened this assumption by Magneto-PA (MPA) measurements, a powerful technique to identify and monitor the triplet excitons. As a control experiment, we

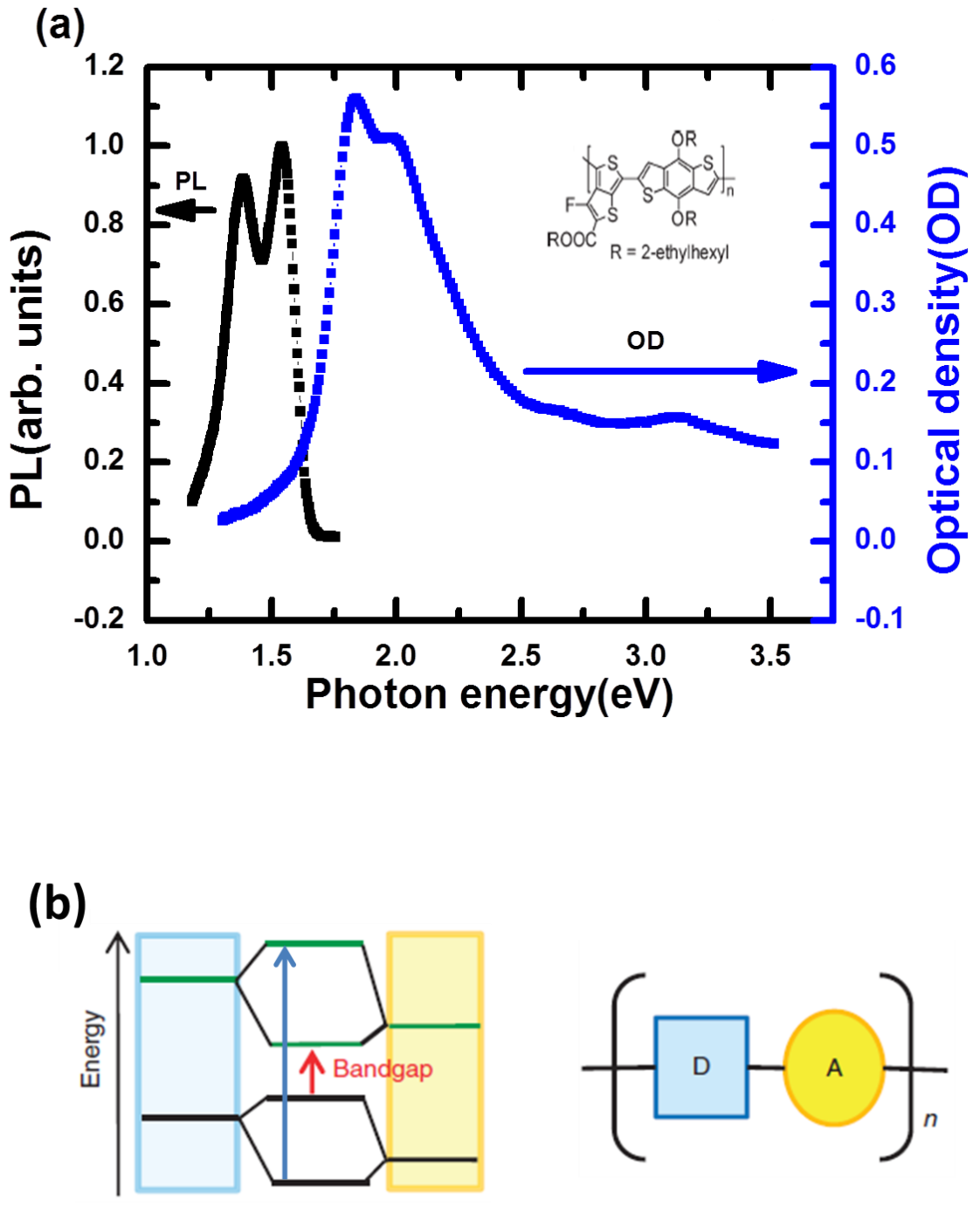

Figure 4.1. PTB7 polymer. (a) Absorption (blue) and emission (black) spectra of PTB7 polymer. (b) energy levels in donor-acceptor copolymer. Repeat unit in D-A shown as a block (right) (Adapted from reference [133]).

demonstrate that PTB7/PC70BM, where galvinoxyl has detrimental effect in PCE, does not show the reduction in polymer triplet density, implying the inability of the radical to convert ^{3}CT into ^{1}CT state. We believe that the efficiency of this process depends on the resonant condition of radical's singly occupied molecular orbital (SOMO) level with the CT states. We note that the underlying physics is completely different when the polymer triplet state is higher than the charge transfer state as in the case of P3HT/PCBM [134, 136]. In this case, the spin ½ radical plays a role in defining the steady state density of polaron pair triplet and singlet states in the polymer donors rather than the CT states, as explained in our previous work [128].

In the last section of this chapter, we report the substantial differences in the device performances based on P3HT/PCBM BHJs under different conditions. First, the PCE of the devices depends on the molecular weight of the polymer, and is higher for devices with high molecular weight P3HT [137]. Second, regio-regular P3HT forms the large domain size and lamellar structure compared to regio-random P3HT; this eases carrier transport through the active layer, reduces the recombination, and exhibits higher PCE [20]. Finally, device performance after adding galvinoxyl spin ½ radical in the blend is reported [128].

4.2 Experimental

PTB7 polymer was synthesized by the Luping Yu group at the University of Chicago; P3HT was supplied by Plextronics, Inc.; PC60BM and PC70BM were purchased from the American Dye Source, Inc.; and galvinoxyl was purchased from Sigma Aldrich. These materials were used as received without further purification. The

polymer solution is prepared in ODCB at the concentration of 10 mg/ml. PTB7 blend films were prepared in the ratio of 1:1.5 by weight in the mixture solvent of of 1,2-dichlorobenzene (ODCB) and 1,8- diiodooctane (DIO) (97:3 by volume). P3HT blend was prepared in the ratio of 1:0.8 by weight in ODCB. Several percentage weight of galvinoxyl radical is mixed in the blend to measure the effect of spin ½ radicals. Spin-coated films are used for the optical and electrical studies.

For the PA and PL spectroscopy studies we placed the films in a closed cycle He refrigerator cryostat at 50K. The steady state PA spectrum was measured using a standard setup [137]. We used for excitation a diode laser at $\hbar\omega$=1.8 eV that was modulated at frequency f of 310 Hz, and the output beam of an incandescent tungsten/halogen lamp as probe light source. The change, ΔT in the probe transmission, T induced by the laser pump excitation was measured using a lock-in amplifier referenced at f, a monochromator, and various combinations of gratings, filters, and solid-state photodetectors spanning the spectral range 0.3< $\hbar\omega$(*probe*) <2.3 eV. This setup was also used for measuring the PL spectrum. The PA spectrum was obtained from the relation PA= $-\Delta T/T$, the negative fractional change in transmission.

The same setup was used for the MPA measurement, with an external magnetic field provided by an electromagnet that produced field B up to 1800 Gauss that was applied parallel to the film surface. Since the materials of most mirrors and posts contain some magnetic impurities that can react with the applied magnetic field, care was taken to use nonmagnetic optical elements in our optical setup. In addition, we also performed several control experiments to minimize possible magnetic field artifacts. The MPA(B) response is defined by the relation MPA(B)=[PA(B)-PA(0)]/PA(0), where PA(B) is the

PA at field strength *B* and PA(0) is the PA at *B*=0.

For the DIA measurement, the PTB7 film was doped in iodine vapor for 1 minute and the linear absorption was measured before and after doping. For the PADMR measurements, we used an optically accessed 3 GHz μ-wave resonator located between the poles of a superconducting electromagnet inside the Helium cooled cryostat. For the EA measurement, very thin film was deposited on the substrate having 40μm wide gold finger electrodes and an ac electric field of 10^5V/cm is applied at 500Hz modulation frequency using a transformer and function generator.

The OPV device structure was in the form of ITO/HTL/active layer/Ca/Al. HTL was a hole transport layer of 40 nm thick film of PEDOT:PSS poly(3,4-ethylenedioxythiophene)/poly(styrenesulfonate); the active layer was a ~100nm film of PTB7 or P3HT blend; and the cathode was a calcium film (20 nm thick) and aluminum layer for protection; the device area was 2mm×2mm. The OPV fabrication comprised of several steps. First, the anode ITO substrate was cleaned by ultrasonic treatment with acetone, 2% micro-90 soap, de-ionized water, methanol, and propanol; each for 10 minutes. Subsequently, the PEDOT:PSS was spin-coated onto the ITO substrate, and heat treated for 30 minutes at 100°C. The resulting bilayers were transferred to a glove-box filled with nitrogen atmosphere, where the PTB7 solutions were spin-coated at 1000 rpm and the P3HT solutions were spin-coated at 400 rpm. Top electrodes of Ca and Al layers were deposited using a thermal evaporation bell-jar inside the glove-box. The device fabrication process was finalized by encapsulating the device with a cover glass using UV-curable optical adhesive to minimize the exposure to the air (mainly oxygen). I-V characteristics is measured using Xenon lamp light source (calibrated with Si PV from

NREL) with Keithley 236 Source-Measure unit under AM 1.5 conditions.

4.3 Results and Discussion

4.3.1 PTB7 Polymer

Figure 4.1 (a) shows the absorption (blue) spectrum of the PTB7 polymer. The absorption band is red-shifted compared to high bandgap polymers such as P3HT and PPV, which enables the device to harness more of the solar spectrum. This polymer has two absorption bands with peaks at high energy (2.0 eV) and at low energy (3.14 eV) with the absorption onset at ~1.6 eV which is the optical bandgap. A vibronic replica at 1.84 eV is also clearly observed. The two absorption bands are justified since this is a donor-acceptor copolymer, as schematically shown in Figure 4.1(b). The band at 2.0 eV is interpreted as due to absorption from LUMO of donor to HOMO of acceptor and the band at 3.14 eV is due to the transition between HOMO of donor to LUMO of acceptor moieties in the polymer chain, as depicted in Figure 4.1(b). This is an interesting coincidence, as green leaves in plants also do not absorb green, but rather absorb lower and higher energies. This kind of absorption is ideal for solar cells, as it covers the large range of the solar spectrum in the visible/near-infrared. Figure 4.1(a) shows the PL spectrum (black) of this polymer when excited with 660 nm diode laser and measured at low temperature of 45K. It has a 0-0 transition at 1.54 eV and 0-1 vibronic transition at 1.38 eV. The PL spectrum shows very strong, and almost equal intensity 0-0 and 0-1 transitions, and no other higher order replicas; The PL quantum efficiency of this polymer is 24%; this is very high as compared to 4% for regioregular P3HT. This gives further evidence for the intrachain exciton recombination and the lack of aggregation.

From the electroabsorption measurement shown in Figure 4.2, we can identify the band at ~1.8 eV as the lowest exciton state, $1B_u$. At ~2.2 eV, we can recognize an induced absorption feature, assigned as mA_g. According to the separation of EA exciton contribution ($1B_u$) and continuum band (mA_g), we can estimate the exciton binding energy as ~0.4 eV. There are two other B_u and A_g bands at 3.1eV and 3.5eV, respectively, which are due to $1B_u$ and mA_g from donor to acceptor moieties and we assign them as $1B_u$* and mA_g*. This kind of higher energy EA features are also present in other copolymers, such as PCPDTBT and PDTP-DFBT that we observed in our laboratory.

To understand the polaron absorption band in this polymer, we performed DIA measurements of the film at room temperature. For this we exposed the polymer film with iodine vapor for 1 minute and the difference in absorption before and after doping were measured. The DIA spectrum in Figure 4.3 shows doping-induced absorption bands at 0.4 eV and 1.1 eV, respectively. Since there are two polaronic transitions, as mentioned in section 1.3.2, these transitions are assigned as P_1 and P_2. Here, we want to emphasize that the DIA is a crucial measurement to help identify the characteristic transitions of the polarons in this particular polymer.

In order to understand the excitonic nature in the polymer, we studied picosecond photomodulation spectra of thin film. Transient measurements were carried out by Mr. Uyen Huynh in our group with the pulse laser system of high repetition rate 80 MHz and low energy 0.1 nJ/pulse. Figure 4.4 shows the PA spectrum at time T= 0ps, 100ps and 500 ps. The transient spectrum contains three PA bands at 0.4eV, 0.7eV and 1.1eV, respectively. From the EA spectrum of the polymer, we identify the 0.4eV band as due to

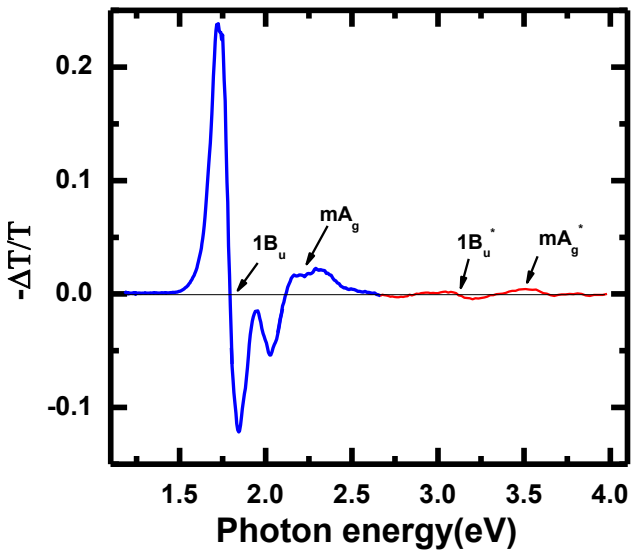

Figure 4.2. EA spectrum of the PTB7 polymer measured at 40K.

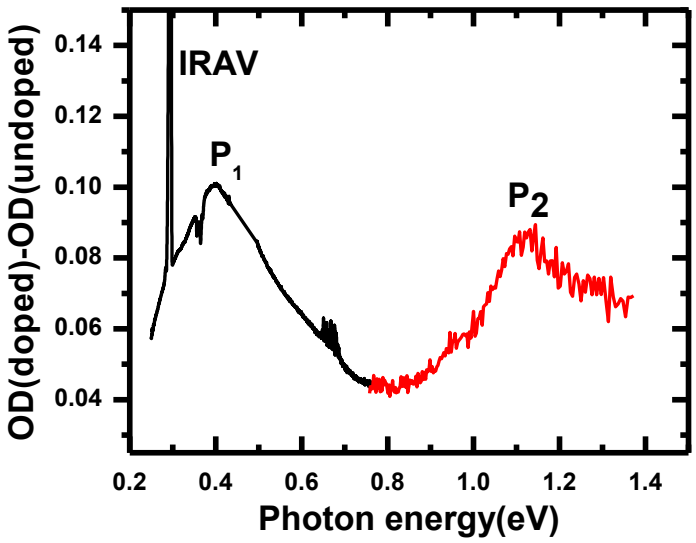

Figure 4.3. DIA spectrum of the PTB7 film exposed to Iodine vapor for 1 minute at room temperature.

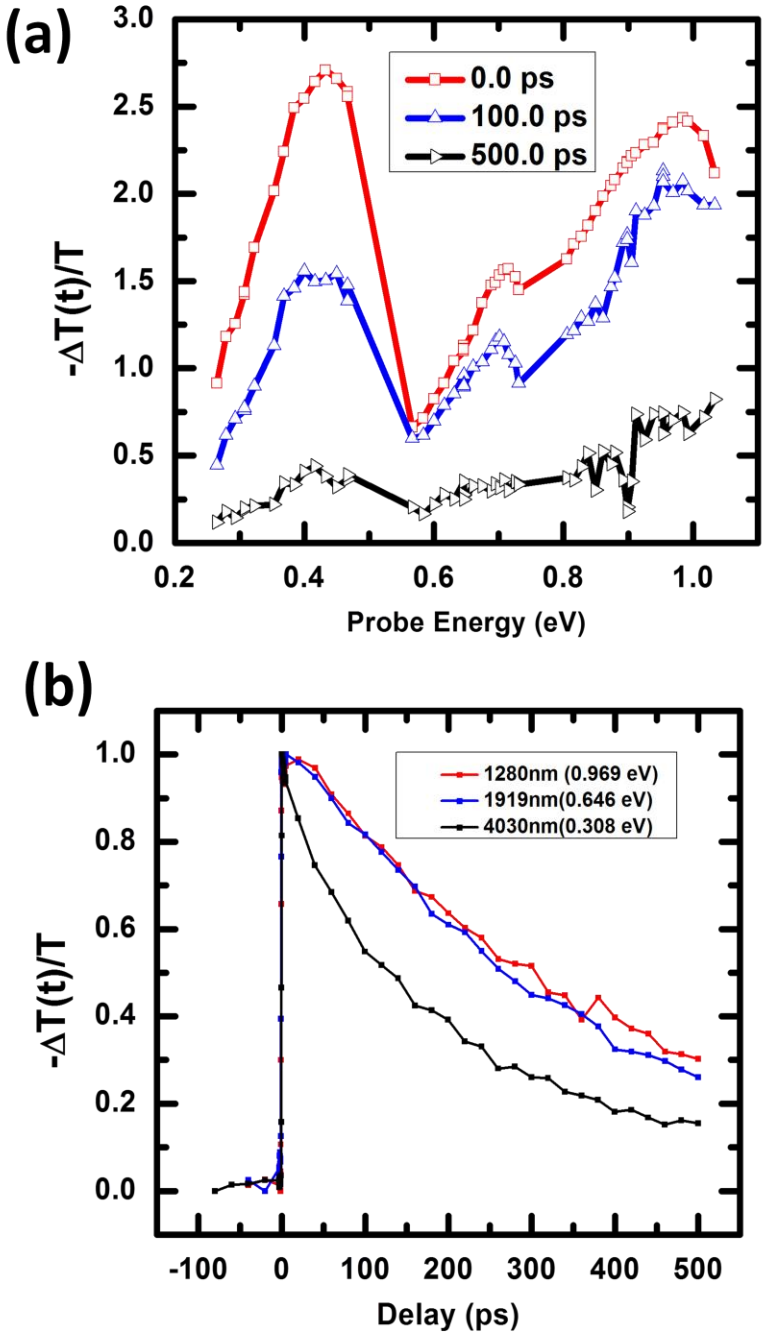

Figure 4.4. Transient PA of PTB7 film. (a) Spectra at different delay times of PTB7 polymer. (b) Decay kinetics of the PA at three different bands.

singlet excitons. Also from the decay dynamics shown in Figure 4.4(b), it decays faster than the other two bands. At the same time, the other two bands at 0.7 eV and 1.1 eV have very similar decay (Figure 4.4(b)). We thus assigned these bands as triplet pairs (TT) and triplets (T_1), respectively. These bands are nearly instantaneously generated, at least within our instrumental response time of 300 fs; and the lack of intensity dependence also supports the assumption that they originate from geminate pairs. The band at 0.7 eV is assigned as TT pair as it decays while the polarons and the triplet in the blend rises with a similar time constant.

In Figure 4.5(a), we show the cw PA spectrum at 45K. It has a PA band at 1.1 eV and there is no polaron band (within the noise level) at lower energy which implies the good quality of a defect free polymer. We have performed Optically-detected Magnetic Resonance (ODMR) to identify the nature of the excited species in this polymer. PA-detected Magnetic Resonance (PADMR) at 1.1eV shows both the full field and half field resonance signal as presented in Figure 4.5(b). As explained in section 2.7, these resonances are due to the transitions between different spin energy sublevels of the triplet excitons. We thus conclude that the CW PA signal is due to triplet excitons. Furthermore, PL-detected Magnetic Resonance (PLDMR)(Figure 4.5(c)) also shows the same kind of triplet powder pattern. This is explained as PL is influenced by singlet exciton collision with triplet excitons in the film [88]. The positive ODMR signal tells us that these collisions reduce the singlet exciton density in the polymer film, in agreement with the reduction of triplet excitons revealed by PADMR. We can estimate the zero field splitting parameters (ZFS), D and E, from the powder pattern by locating the position of steps and divergences in the experimental data.

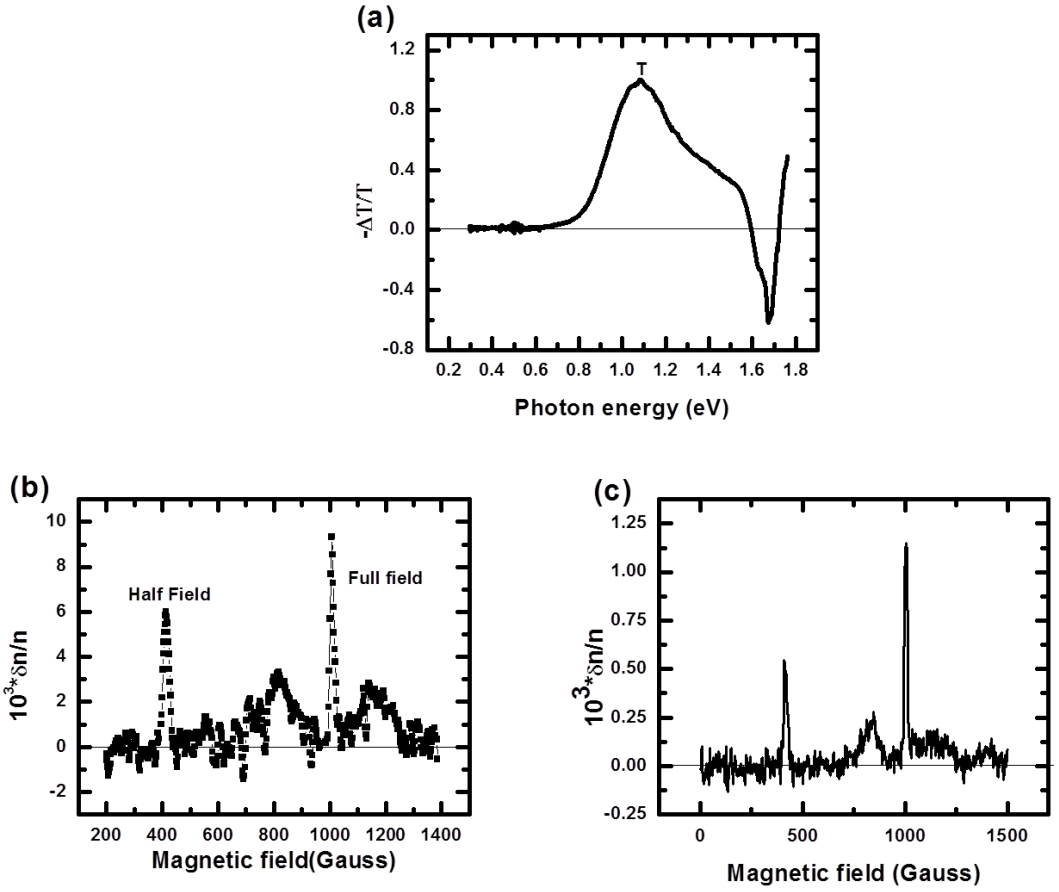

Figure 4.5. PA spectroscopy of PTB7 film. (a) PA spectrum, (b) PADMR at probe energy 1.1eV and (c) PLDMR

For Full field resonance:

Steps at: $$H_{1,2} = H_0 \pm D \tag{4. 1}$$

Divergences at: $$H_{3,4} = H_0 \pm \left(\frac{D - 3E}{2}\right) \tag{4.2}$$

For Half field Resonance:

Divergence at: $$H_{HF} = \frac{1}{2}\sqrt{H_0^2 - (D + E)^2} \tag{4.3}$$

Using Eq. (4.2) and (4.3) and the values H_0= 1006G, H_3= 1160G, H_4=817G, and H_{HF}=416G, the ZFS parameters are estimated to be ~510G and ~56G for D and E, respectively.

There is another powerful approach to identify the photogenerated species in the film. The technique, called MPA, as introduced in section 2.3 is used here on the PA band. MPA response depends on the splitting of the levels involved, and in case of triplet excitons, it is due to the different recombination and/or dissociation rate of triplets at different spin sublevels in the presence of magnetic field. We measured the MPA full width half maximum of ~370G which is much larger than the hyperfine interaction (<100G) in π-conjugated polymers, and conclude that the MPA response originates from triplets**.** We see that the triplet excitons' MPA response has opposite sign to that of the Magneto-Photoluminescence (MPL) response of the polymer, as shown in Figure 4.6(a) and (b) respectively. When triplet interacts with the singlet excitons, decrease in the triplet exciton density in the presence of magnetic field should follow by an increase in the singlet exciton density, which is in agreement with our experimental results.

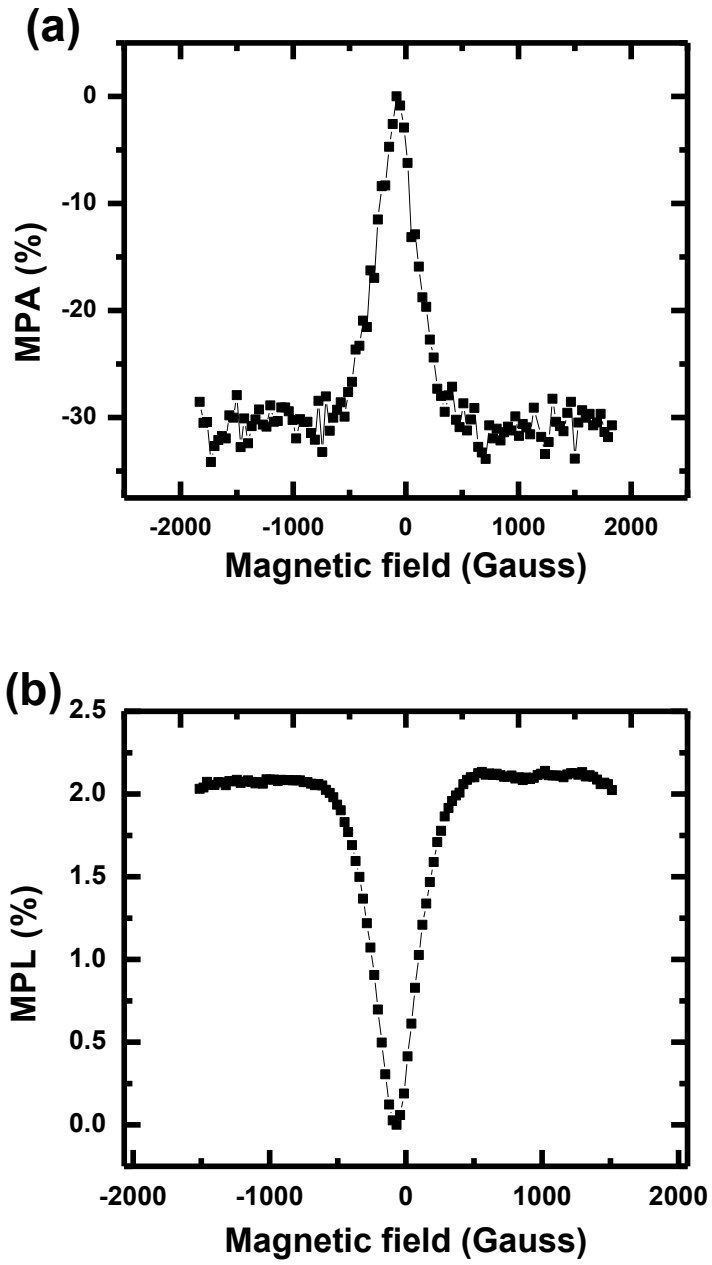

Figure 4.6. Magnetic field effect on PA and PL in PTB7 film at 45K. (a) MPA at 1.1 eV, and (b) MPL.

4.3.2 PTB7 Blend

We studied the optical properties of the polymer mixed with the acceptor PC70BM. Blends are prepared in ODCB solvent without and with DIO molecular additives, which improve the morphology of the film. Figure 4.7(a) shows the optical density of the blend film with and without DIO. The addition of the acceptor molecule makes the strong absorption in the higher energy range which otherwise has almost no absorption in the polymer. The blend with DIO has nice flat absorption region which helps to absorb the solar spectrum efficiently. PL emission from the blends shows highly reduced PLQE of 1% and 0.5%, respectively, as compared to the 24% of the pristine polymer. This shows the strong charge transfer nature of this blend. Since it is a donor-acceptor copolymer blend, singlet excitons generated in the polymer are delocalized within the polymer itself and easily find their way out to reach to the acceptor PCBM

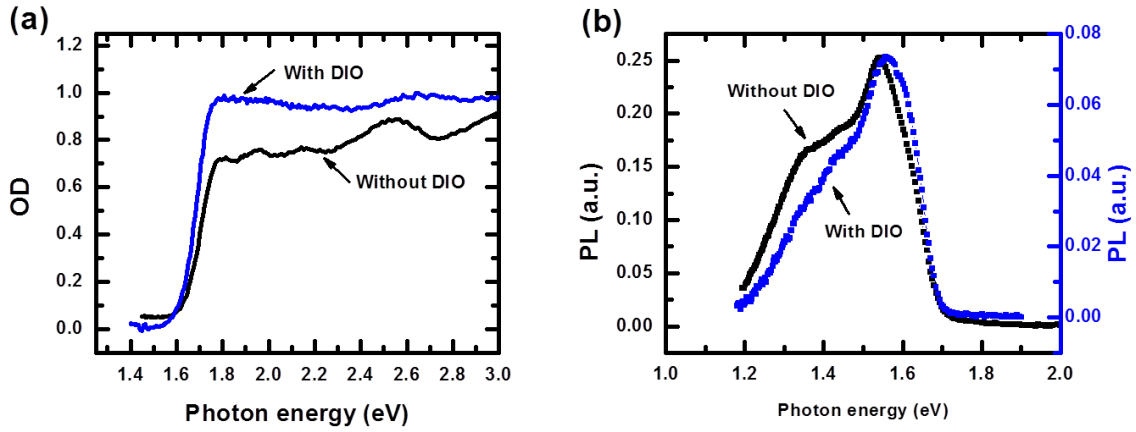

Figure 4.7. Absorption and emission of PTB7/PC70BM blend. (a) Absorption and (b) PL spectra with (blue) and without (black) DIO solvent additives.

molecule and thereby reduces recombination. We will show the superior power conversion efficiency of the OPV device based on this blend in section 4.3.3.

We studied PA spectroscopy of this blend at low temperature of 45K. Here, we do not see the significant differences in the blend with and without DIO. Figure 4.8(a) shows the PA spectrum in the blend which consists of two bands at ~0.4 eV and ~1.1 eV. These PA bands are identified as due to polaronic bands, as verified by the DIA measurements shown in Figure 4.3. The PADMR response at 1.1 eV does not show the triplet powder pattern and together with the absence of half field response enable us to assign this band at 1.1 eV as the polaron band, P_2.

MPA measurements shown in Figure 4.8(c) and (d) of these bands reveal that the band at ~0.4eV is the polaron, as it has very small FWHM of ~ 70G which is near the typical hyperfine coupling strength in the polymer. MPA at 1.1 eV shows the triplet excitonic response with FWHM of ~320G which contradicts the PADMR and DIA results. However, if we look carefully, we notice two important details to resolve this contradiction. First, the FWHM of the MPA in the blend at 1.1eV is always less than that of the triplet exciton in the pristine polymer. Second, the PA of the polymer also lies at 1.1 eV, which masks the polaronic nature in MPA as MPA_{max} of the polaron is very small compared to the triplets. Therefore, we conclude that the PA at 1.1 eV is due to both polaron and triplet which cannot be easily resolved because of the overlap of two PA bands. MPA at 1.1 eV is strongly dominated by the triplet as seen in the Figure 4.8(d) where we have the high value of MPA_{max} of 15%, whereas the PADMR at 1.1 eV is dominated by the spin ½ transitions at B~ 1007 Gauss.

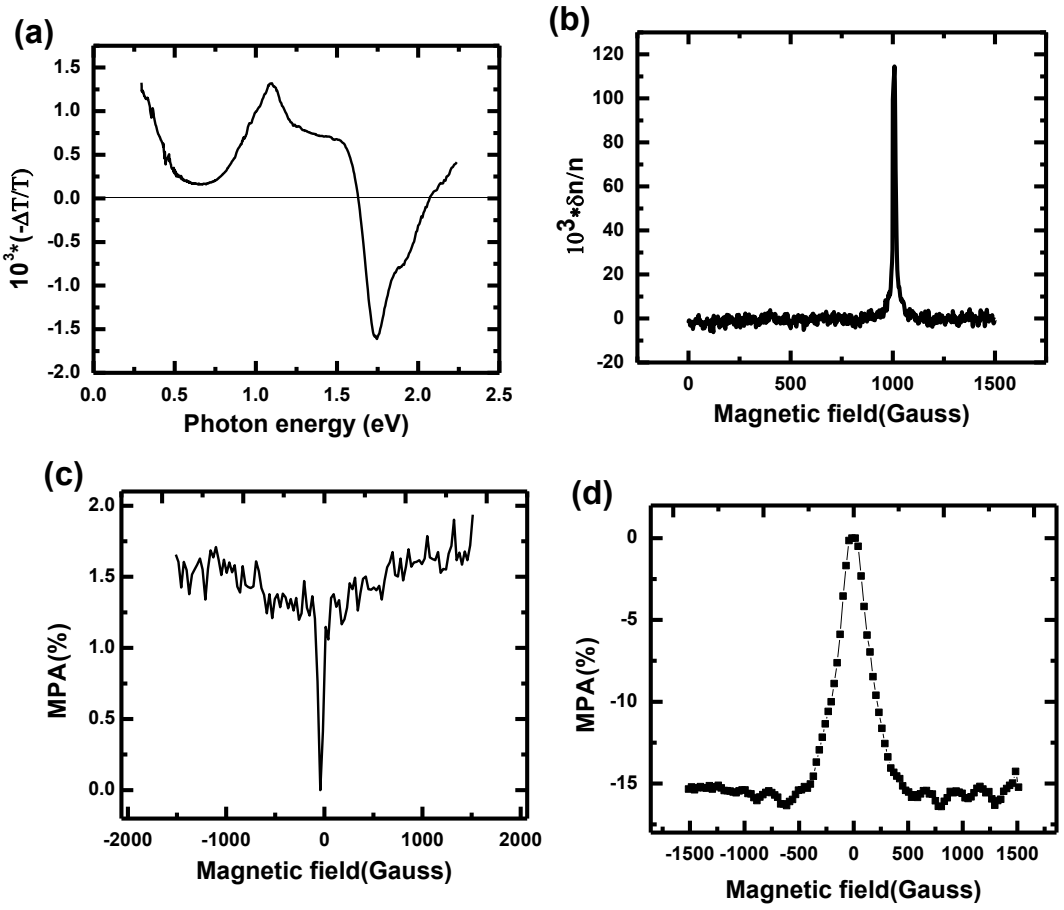

Figure 4.8. Magneto-optical spectroscopy of PTB7/PC70BM blend. (a) PA spectrum and, (b) PADMR response at 1.1 eV. MPA(B) response at (c) 0.4eV and (d) 1.1 eV.

4.3.3 PTB7 Devices

Figure 4.9(a) and (b) show the I-V characteristics of the PTB7/PC71BM device with and without DIO solvent. As mentioned earlier, DIO improves the absorption and morphology of the film, as in the case of other blends with PC70BM reported in the literature [123, 138]. The moderate PCE of the device without adding DIO is enhanced to almost ~7% from ~5.4%. These devices are fabricated in the same conditions and from the same batch of processing materials. The higher device performance can be explained by the increased mobility due to better morphology, and reduction of the recombination which is reflected in the I-V characteristics under illumination as an increase in short-circuit current density and fill factor (FF) of the device.

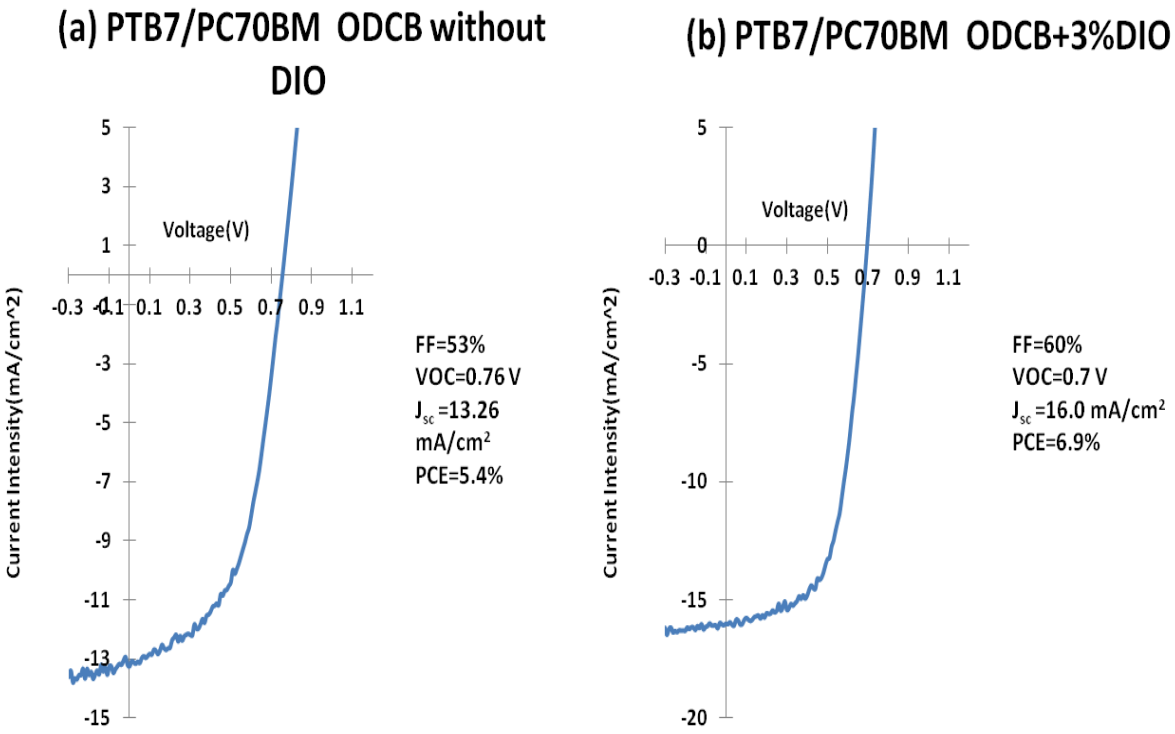

Figure 4.9. I-V characteristics of the photovoltaics of PTB7/PC70BM. (a) without and (b)with solvent additive DIO.

Next, we studied the PCE enhancement in OPV using spin ½ radicals. Earlier, in our previous work, we showed that the PCE of P3HT/PCBM devices increases after adding galvinoxyl in the bulk hetero-junction (BHJ). Details of the device characteristics will be explained in section 4.3.4.3. Here, in the OPV device based on PTB7 polymer and PC60BM blend, we obtained significant increase in PCE of the device with galvinoxyl by 30%, that is, from 5.2% to 6.8%, as shown in Figure 4.10 (a). In the Figure, we show the I-V characteristics under AM1.5 sun illumination of the two devices; namely PTB7/PC60BM(black) and PTB7/PC60BM with inclusion of spin ½ Galvinoxyl (blue). It is clearly seen that the enhancement in PCE is due to increase in short-circuit current, J_{sc}, from 10.4mA/cm^2 to 14.4mA/cm^2. We have plotted the J_{sc} and PCE of devices under sun illumination versus % galvinoxyl in Figure 4.10(b). PCE follows the same trend as J_{sc} and is maximized for 2% Gxl device. Device parameters J_{sc} , V_{oc}, Fill factor, and PCE for various percentages of Galvinoxyl are listed in Table 4.1.

To understand the mechanism of the PCE increase in galvinoxyl added devices, we studied the photo-physics of the thin film of the PTB7/PC60BM blend. The blended film with and without galvinoxyl is optically excited by the 660nm diode laser and probed with the tungsten lamp. In Figure 4.11(a), we show that the PA spectrum with (red) and without (black) galvinoxyl additives has two bands at 0.4eV and 1.1eV, same as the previously observed bands in PTB7/PC70BM blend. The band at 1.1 eV is the mixture of triplet excitons (T) and the polarons (P_2) as verified by DIA and PADMR measurements, whereas the band at ~0.4eV is due to photogenerated polarons. We note that the polaron intensity is higher in the case of the blend with galvinoxyl as compared to the blend without galvinoxyl. The effect of spin ½ additives in the blend is to enhance

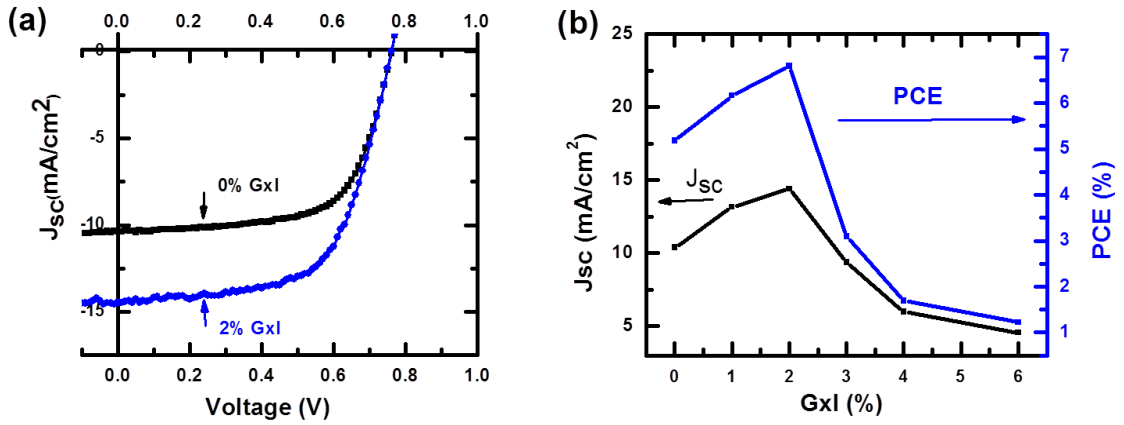

Figure 4.10. Photovoltaic characteristics of PTB7/PC60BM device. (a) I-V plot of the device without(black) and with(blue) galvinoxyl.(b) PCE(blue) and Jsc(black) of the OPV devices versus percentage galvinoxyl.

Table 4.1. Device parameters versus galvinoxyl percentage.

% GxI	Jsc(mA/cm^2)	Voc(V)	FF(%)	PCE(%)
0	10.4	0.77	65	5.2
1	13.2	0.76	62	6.2
2	14.4	0.76	62	6.8
3	9.4	0.72	46	3.1
4	6.0	0.65	43	1.7
6	4.6	0.64	42	1.2

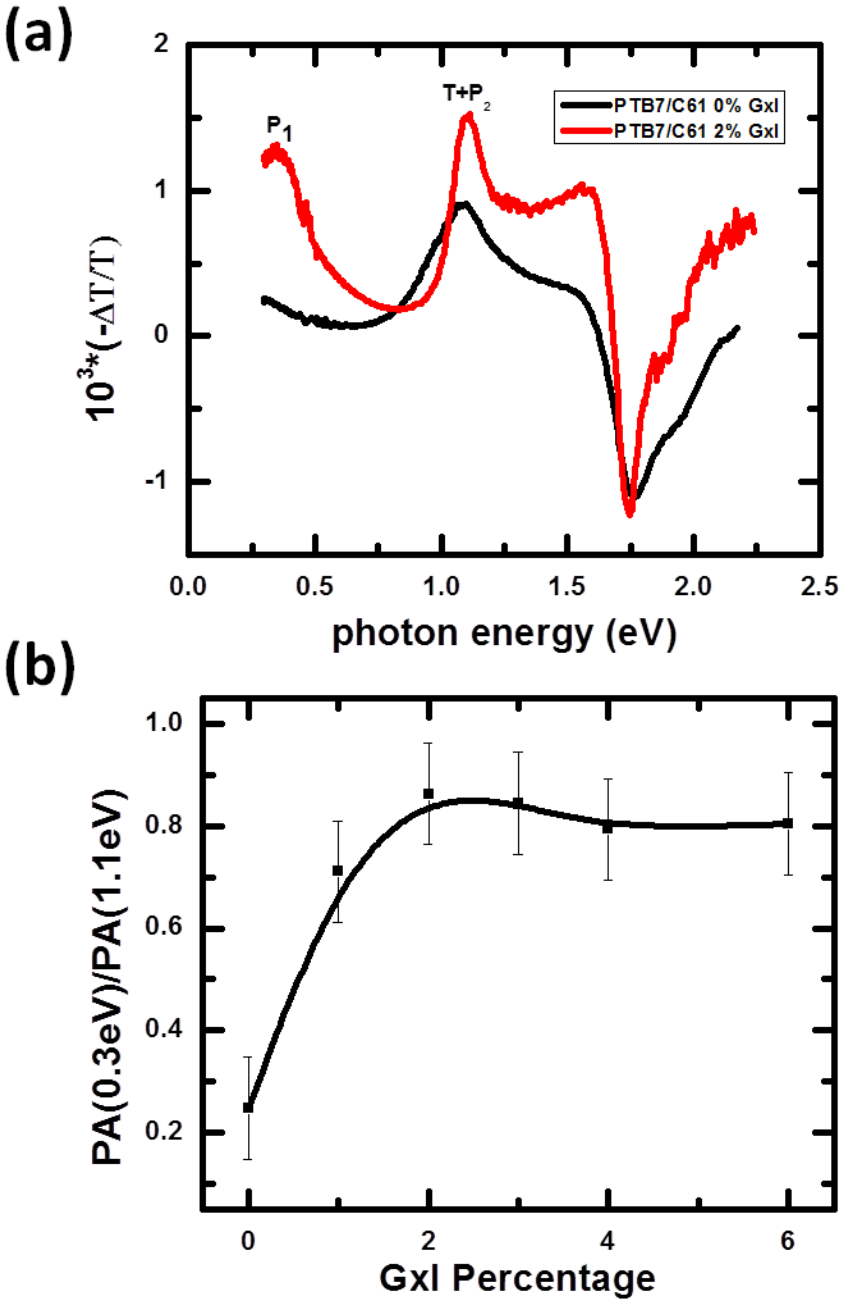

Figure 4.11. Photo-physics of PTB7/PC60BM. (a) PA spectra of the PTB7/PC60BM blend without(black) and with(red) galvinoxyl additives. (b) Ratio of the PA intensity at 0.34 eV to the intensity at 1.1 eV, measured vs. the galvinoxyl %.

the polaron density at the expense of triplet density, which would dissociate easily into free carriers. This effect is summarized in Figure 4.11(b) where the ratio of the intensity of the polaron to the band at 1.1 eV is presented. This ratio increases with the % galvinoxyl and reaches saturation at high concentrations.

We further analyzed the PA band at 1.1 eV by applying the magnetic field. MPA of the PTB7/PC60BM blend (Figure 4.12 (a)) shows the high MPA_{max} of ~23% which comes from the triplet exciton, as polaron does not show very high MPA and the FWHM of ~340G is comparable with the MPA of the polymer (Figure 4.6 (a)). However, after adding galvinoxyl in the blend (Figure 4.12(b)), MPA response is dramatically reduced to <1% and the FWHM becomes smaller (~230G). As the triplet intensity is reduced, the band at 1.1eV has significant contribution from polarons, which influences the FWHM of the superposition of two bands smaller. Here, we want to note that the MPA at ~0.4eV does not show significant changes in the magnitude; we conclude that MPA from polarons is an intrinsic process that does not depend on the polaron density. The decrease in triplet density at 1.1eV after adding galvinoxyl is also evident from the ultrafast PA result. Figure 4.13 (a) shows the decay dynamics of the 1.1 eV band of the PTB7/PC60BM blend with different weight % of galvinoxyl. Earlier, we have shown the instantaneous generation of triplet states in the polymer which decay very quickly. In the blend, triplets first decay, and then increase again showing a secondary triplet generation. This secondary generation process of triplet comes about from another route: It is very likely that this occurs through the charge transfer exciton that relaxes back to the triplet state at the heterojunction. When the % galvinoxyl increases, the CT triplet density decreases and consequently the generation of triplet excitons in the polymer through the

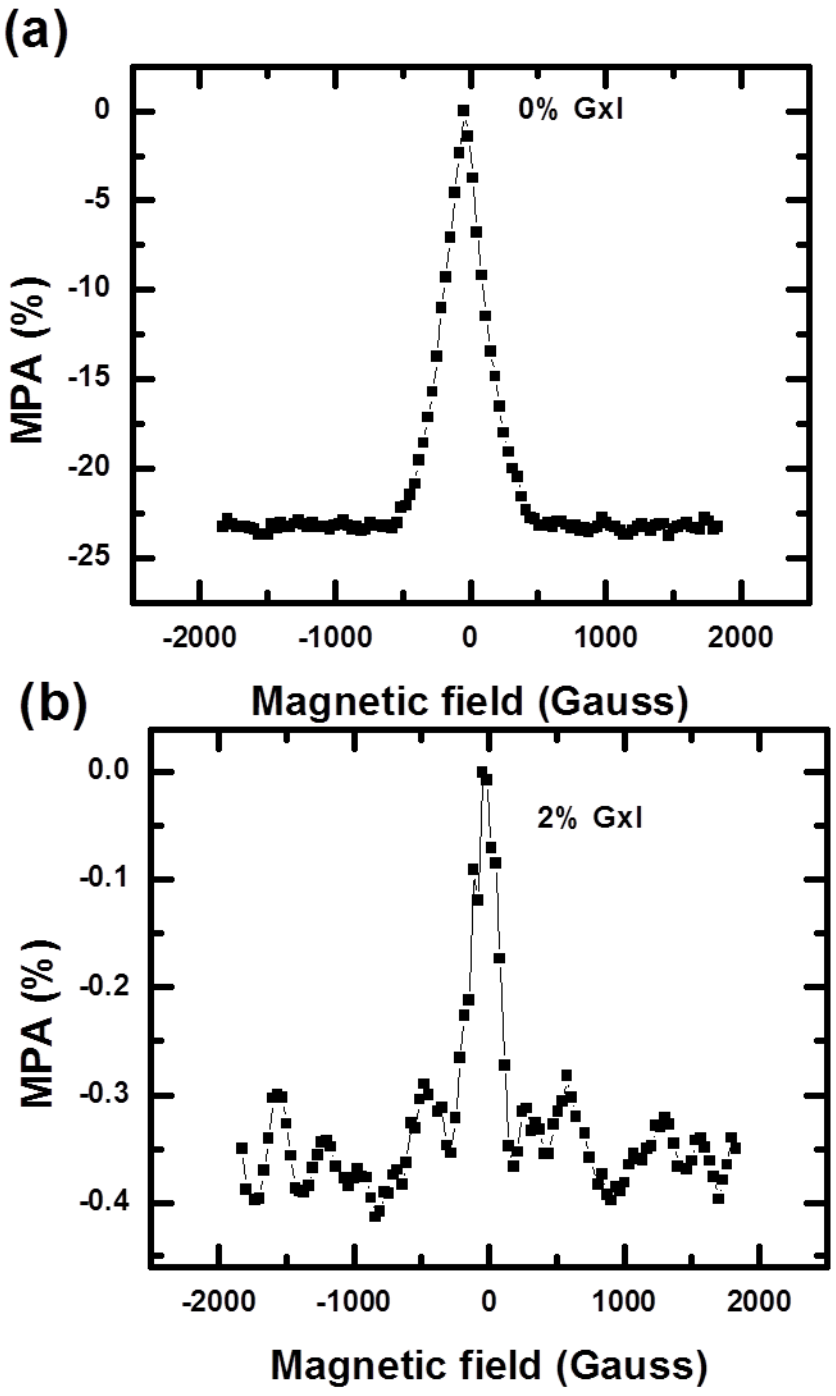

Figure 4.12. MPA(B) response of PTB7/PC60BM films at probe energy 1.1eV; (a) pristine and (b) with galvinoxyl additives.

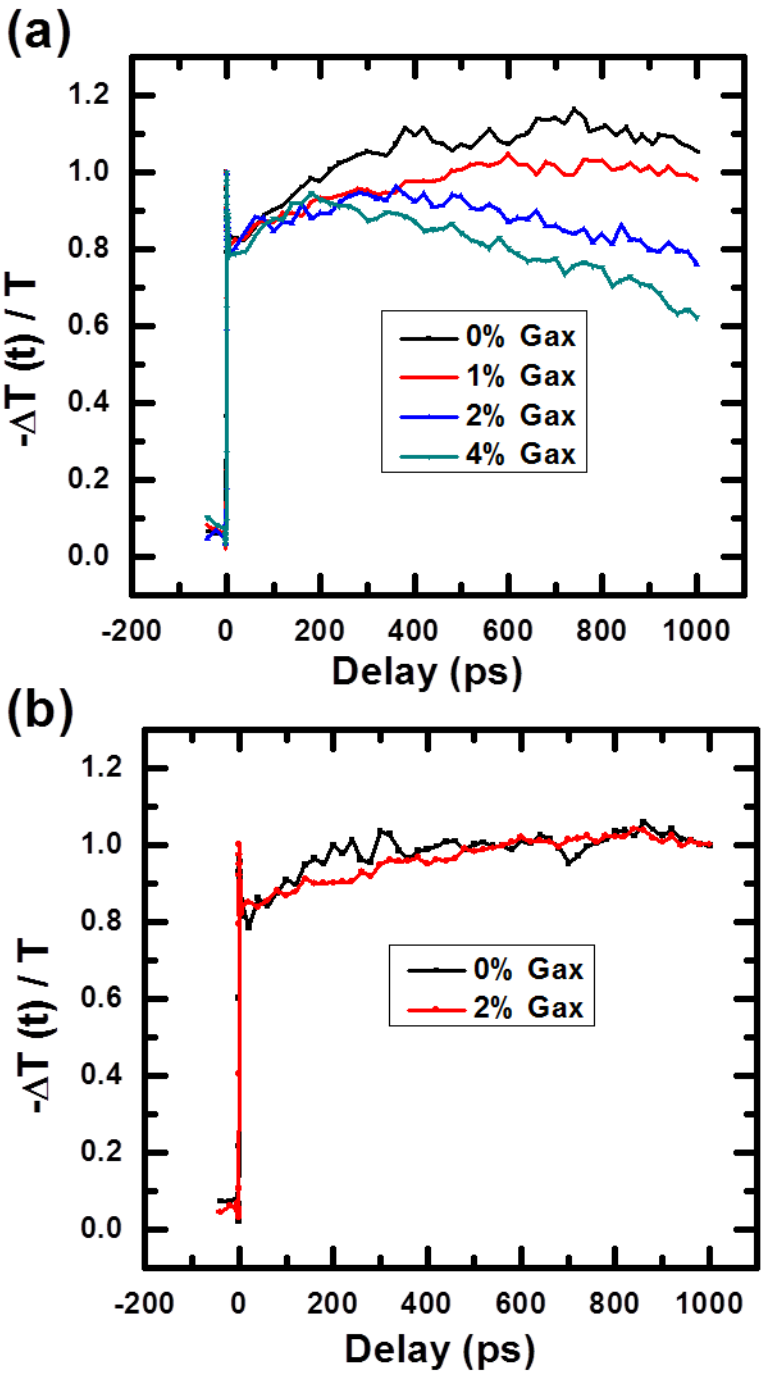

Figure 4.13. PA decay kinetics at 1.1 eV of (a) PTB7/PC60BM and (b) PTB7/PC70BM devices with different percentage of galvinoxyl.

CT state (the second generation channel) is suppressed, which is in agreement to our CW PA measurements.

To explain how the Galvinoxyl enables charge separation process, we have shown the details process of the charge separation in BHJ (Figure 4.14) modified from reference [24]. First, photo-excited singlet excitons are transferred to charge transfer states where they either dissociate into polarons or relax to the lowest CT state. CT excitons either dissociate to free carriers or relax to form triplet excitons, since the CT state's energy level, ~1.27eV, is higher than that of T_1, ~0.9eV, in the polymer [134]. We propose that the spin ½ additives facilitates the intersystem conversion of singlet and triplet CT states, and thereby either enhances or lowers the device photocurrent. If the singly occupied energy level (SOMO) of the radical is in resonance with the CT state energy level, then this intersystem conversion would be efficient. Whether this interconversion increases the triplet or singlet exciton density may depend upon recombination and dissociation rate of

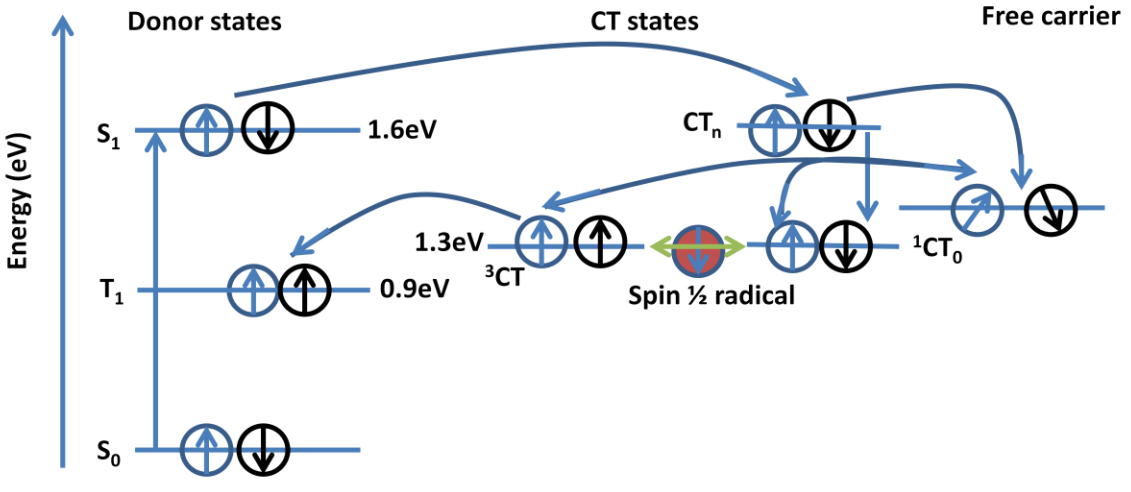

Figure 4.14. Schematic of working principle of PTB7/PC60BM electronic processes in the presence of galvinoxyl radical upon photon absorption.

those states. In PTB7/PC60BM, we have shown that PCE is enhanced; number of triplet excitons is reduced after adding galvinoxyl, implying that it prevents the CT triplet formation from the CT singlet.

We also studied the galvinoxyl effect in PTB7/PC70BM device where it is detrimental to the PCE performance. Figure 4.15 (a) shows the I-V characteristics of the device in PTB7/PC70BM blend with (red) and without (black) galvinoxyl. In contrast to the PTB7/PC60BM blend, the PCE here is lower after adding 2% galvinoxyl from 6.8% (J_{sc}= 18.7mA/cm^2, V_{oc}= 0.70V, FF = 0.52) to 3.7% (J_{sc}= 11.0mA/cm^2, V_{oc}= 0.69V, FF = 0.49). The decrease is PCE is mainly due to decrease in $J_{sc,}$ and also a slight decrease in fill factor. According to our scheme, galvinoxyl is unable to avoid the major loss due to triplet excitons. This may be due to the different CT state energy than that in the PTB7/PC60BM blend, which is not in resonance with the spin ½ SOMO level of the galvinoxyl or due to faster dissociation rate of ^{3}CT than its relaxation rate to triplet exciton [24]. In the latter case, device performance is not affected by radical-induced singlet to triplet CT conversion; rather galvinoxyl may act as defect and hinders the carrier transport which results in lower J_{sc} and PCE.

PA spectra of PTB7/PC70BM blends are shown in Figure 4.15 (b). Similar to the PTB7/PC60BM blend, we have triplet overlapped with the polaron at 1.1 eV and the polaron at 0.4 eV. The band at 1.1 eV is dominated by the triplet excitons, both with and without galvinoxyl. MPA of the film without (Figure 4.15(c)) and with (Figure 4.15(d)) galvinoxyl shows no difference. In both cases, MPA effect is ~17% and FWHM is ~350G. Ultrafast decay dynamics in this blend also does not show any sign of suppression of triplet rise after adding the galvinoxyl, as shown in Figure 4.13(b). These

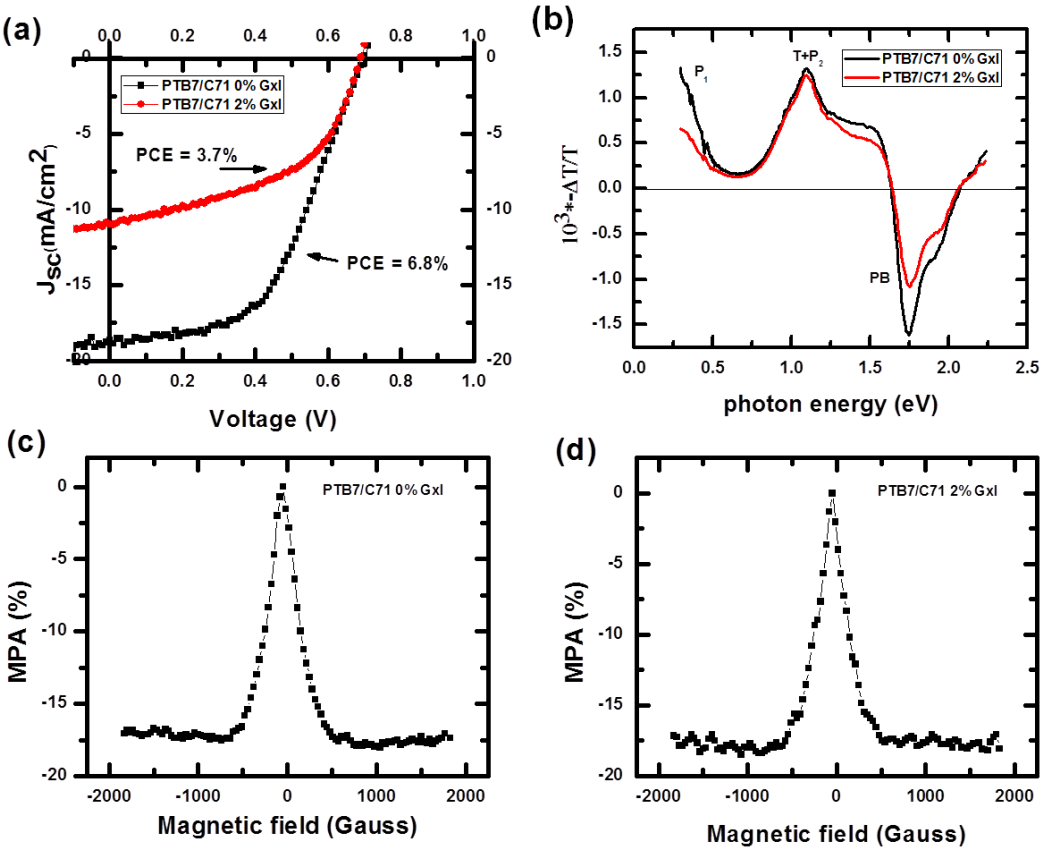

Figure 4.15. PTB7/PC70BM device and photo-physics of films. (a) Photo-current I-V without (black) and with (red) galvinoxyl. (b) PA spectra without(black) and with(red) galvinoxyl. MPA at 1.1 eV without (c) and with (d) galvinoxyl.

results imply that galvinoxyl radicals cannot reduce the triplet exciton formation in this blend. It may be possible to find other spin radicals which match with the CT state energy in the blend, and may facilitate the formation of free carriers instead of triplet exciton through interaction between CT singlet and triplet states.

4.3.4 P3HT/PCBM Devices

4.3.4.1 High and Low Molecular Weight

We have studied the photovoltaic device characteristics of the P3HT/PCBM solar cells based on the different molecular weight of P3HT: one polymer has high molecular weight (HMW) of 50kDa, and the other has low molecular weight (LMW) of 15kDa. We show that OPV cells based on the HMW polymer have ~20% higher PCE than cells based on the LMW polymer. The polymer chain quality can be discerned by the variety of cw and ps transient optical techniques including photomodulation (PM), photoluminescence (PL), and laser action [137]. The HMW polymer film is more homogeneous, shows better order, its steady state PM spectrum does not contain trapped polarons, and it has a prominent stimulated emission (SE) band and laser action at high excitation intensities. Figure 4.16 shows the I-V characteristics of two OPV devices under solar illumination. Device parameters: Jsc, Voc, FF, and PCE for HMW device and LMW device are 9.9mA/cm^2, 0.61V, 68%, 4.0%, and 8.8mA/cm^2, 0.59V, 70%, 3.4% respectively. Both devices show very good fill factor (FF) and overall I-V properties. However, while the FF and open-circuit voltage of the two devices are similar, the short-circuit current density, J_{sc}, is substantially higher in HMW polymer device. The higher J_{sc} may be due to more efficient carrier generation, carrier transport, or both. In either case,

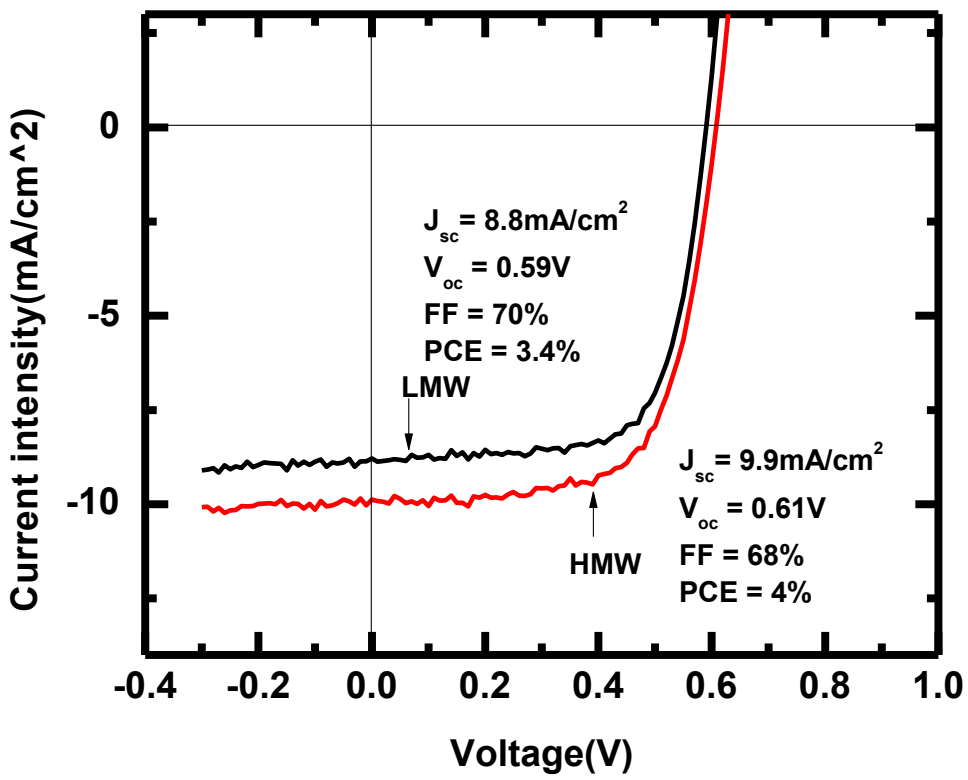

Figure 4.16. The I-V characteristics under solar-like illumination of AM1.5 of two OPV cells based on PCBM blend with HMW (red) and LMW (black) P3HT polymers.

the P3HT polymer quality is involved. One viable mechanism for more efficient carrier generation and transport in the HMW polymer domains might be larger exciton diffusion/carrier mobility based on polymer quality [139, 140]. It is shown that the low quality of the LMW P3HT polymer is manifested in the spectroscopic techniques, where it has broader replica lines and smaller 0-0 suppression in the PL spectrum, and the occurrence of a transient PA band in the visible spectral range that obscures the transient SE band [137].

4.3.4.2 Regio-regular (RR) and Regio-random (RRa) P3HT

In donor-acceptor blends with optimum domain separation such as regio-regular P3HT/PCBM blend of 1.2:1 ratio, solar cell power conversion efficiency (PCE) is ~4%. Instead, in D-A blends with smaller domain size such as regio-random P3HT/PCBM blend of 1.2:1 ratio, solar cell power conversion efficiency is ~0.1%. This result is explained by the two-step charge photogeneration mechanism in polymer/fullerene blends [20]. In RR blends, photogenerated intrachain excitons decay within ~ 10ps and no charge polarons are generated at their expense up to ~2ns. There is a buildup of charge transfer(CT) excitons at the D-A interfaces having the same kinetics as the exciton decay, which dissociate into separate polarons in the D and A domains at much later time(>>1ns). In contrast, in RRa blends where the D and A domain sizes are much smaller, CT excitons are photogenerated at the expense of excitons much faster. However, their dissociation is less efficient because of larger binding energy [141], which explains the smaller PCE value. OPV devices are fabricated from the blend of 1.2:1 polymer to PCBM ratio that was spin-coated and on a cleaned ITO substrate with the

PEDOT on it. RR film is annealed at 150˚C for 30 minutes to enhance the D-A domain size prior to cathode electrode deposition, whereas RRa film is used without annealing. Solar I-V characteristics of the RR (red) and RRa (black) devices are measured and presented in Figure 4.17. PCE and J_{sc} of the RR and RRa devices are 4.0%, 9.87mA/cm^2, and 0.1%, 0.6mA/cm^2, respectively. It is seen that the RR device has an order of magnitude higher PCE and short-circuit current density than the RRa device. Other parameters Voc and FF are also shown in the inset of Figure 4.17.

4.3.4.3 Spin ½ Radicals Additives

In addition to optimizing parameters such as material mass ratio, active layer thickness, and annealing temperature, numerous other approaches have been tried to enhance the efficiency by improving the device morphology, engineering new polymer/fullerene materials, manipulating electrode optical properties, and employing tandem cell architecture and enhancing optical absorption. In this work, we demonstrate a new method to improve OPV efficiency by doping the device active layer with spin ½ radicals to reduce PP recombination at the polymer fullerene interfaces. The spin ½ radical that enhances OPV performance in this work is galvinoxyl (2,6-di-*t*-butyl-α-(3,5-di-*t*-butyl-4-oxo-2,5-cyclohexadien-1-ylidene)-*p*-tolyloxy), a π-conjugated molecule with C_2 symmetry (Figure 4.18(a)). The bulky *t*-butyl groups on the molecule stabilize the radical by keeping other molecules apart thus preventing further radical-radical interaction in the solid state. The unpaired electron is delocalized over the entire molecule and thus its molecular structure may be regarded as a resonance hybrid of two configurations having a localized unpaired spin-polarized electron on a different oxygen

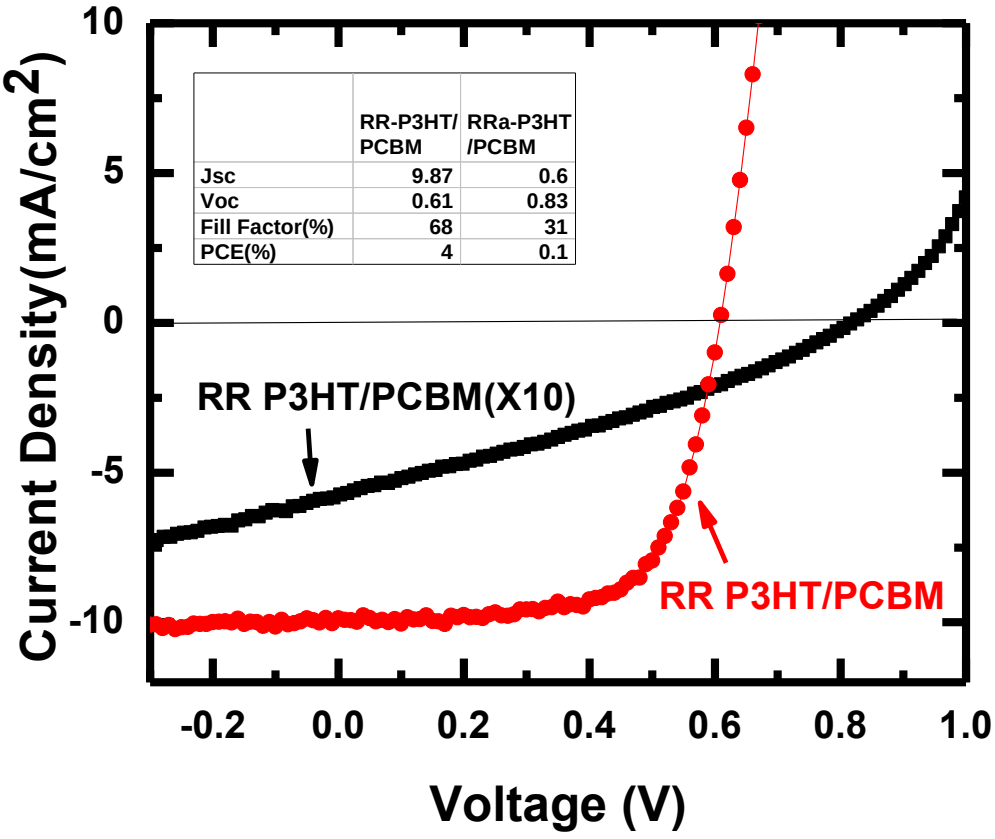

Figure 4.17. The I-V characteristics of two solar cells based on the PCBM blend with RR-P3HT (red) and RRa-P3HT (black) donor polymers under solar-like illumination of AM1.5. The inserted table gives the device photovoltaic characteristics parameters such as short-circuit current density Jsc, open-circuit voltage Voc, fill factor FF, and power conversion efficiency PCE in %.

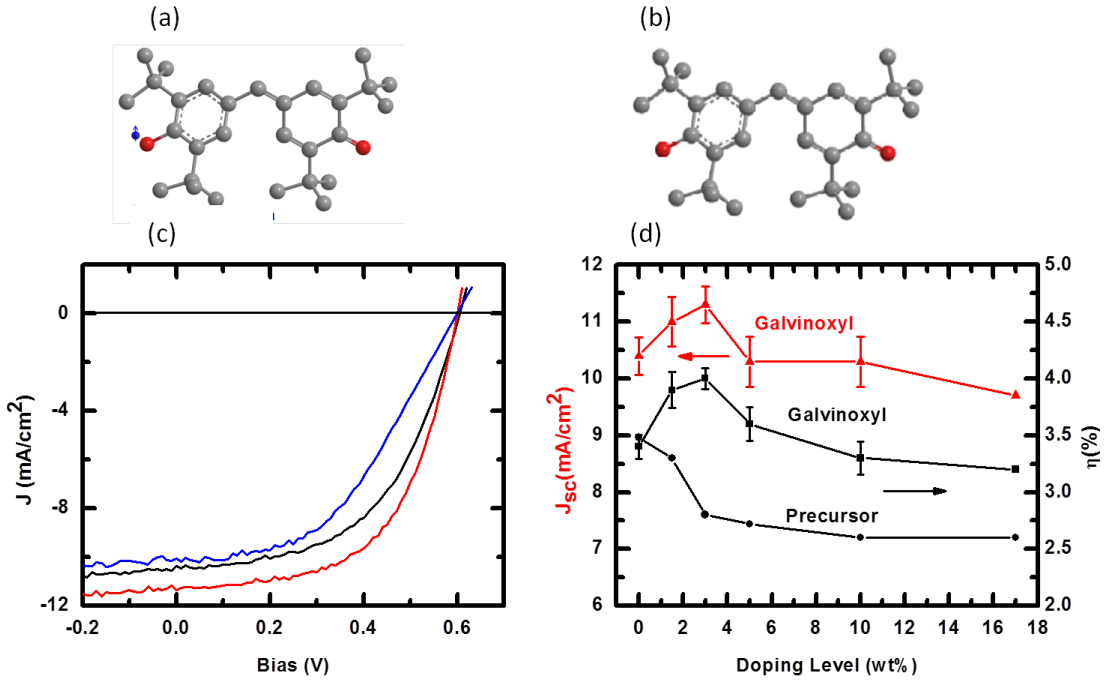

Figure 4.18. Effect of galvinoxyl radical in OPV. Molecular structures of (a) Galvinoxyl radical, (b) Galvinoxyl precursor which does not possess spin ½ radical. (c) J-V characteristics of OPV solar cells of pristine P3HT/PCBM blend (η = 3.4%, Black line), the blend doped with 3 wt% galvinoxyl radicals (η = 4.0%, Red line) and the blend doped with 3 wt% precursor (η = 2.8%, Blue line) under AM1.5 'sun illumination' condition. (d) The change in OPV device properties with galvinoxyl-additive concentration, Jsc (triangles) and η (squares), are shown versus galvinoxyl wt% in the P3HT/PCBM blend. η of OPV devices doped with galvinoxyl precursor is also shown for comparison (circles).

[142]. We investigated the effect of galvinoxyl doping into a 'standard' P3HT/PCBM device with 1.2:1 weight ratio. We note that our standard P3HT/PCBM devices were fabricated using a well-optimized recipe, and the obtained η-value is ~ 3.4%. Figure 4.18(c) shows that by doping 3 wt% of galvinoxyl, η increases from 3.4% (short-circuit current: J_{sc}=10.4 mA/cm^2, open-circuit voltage: V_{oc}=0.6 V, fill factor: FF=0.56) to 4.0% (J_{sc}=11.3 mA/cm^2, V_{oc}=0.6 V, FF=0.62), exhibiting an 18% enhancement in the power conversion efficiency. The 18% increase in η is significantly larger than the standard deviation in η-values of our standard devices (±3%); thus doping with galvinoxyl unambiguously raises the device η-value. The 8.7% increase in J_{sc} that accounts for about half of the improvement in the device η indicates that carrier generation is enhanced, carrier recombination is reduced, or both. Further experimental evidence reveals that reduced PP recombination at the D-A interfaces is responsible for this enhancement and this enhances carrier generation [128]. The remaining enhancement in η is due to an increase in FF indicating a reduced series resistance that results from an improved carrier transport due to galvinoxyl doping. Figure 4.18(d) summarizes the P3HT/PCBM (1.2:1) device properties for all investigated doping concentrations (1.5-17 wt%). The enhancement in J_{sc} and η induced by the galvinoxyl radicals peaks at ~3 wt%, and gradually vanishes with further increased doping. Actually, at high doping level (>10 wt%), galvinoxyl suppresses the device performance. The optimal doping concentration (~3 wt%) at which η maximizes divides the effect of doping galvinoxyl into two regimes: an "enhancement" regime, where η increases with doping, and a "suppression" regime, where η decreases with doping. Controlled experiments of the doped and undoped devices have no variation in absorption and morphology as seen in the absorption, PL,

and XRD measurements [128]. To further check the importance of the galvinoxyl spin 1/2 properties rather than its doping ability, we measured OPV device performance with the addition of 'galvinoxyl precursor' molecule that has one extra hydrogen atom, and thus does not possess a spin 1/2 radical (its molecular structure is shown in Figure 4.18(b)). In contrast to galvinoxyl doping, we found that doping with this precursor monotonically reduces the OPV device performance (Figure 4.18(d). We therefore conclude that the viable mechanism for the OPV η increase with galvinoxyl additives is suppression of PP recombination at the D–A interfaces due to the spin 1/2 radicals.

We studied OPV devices based on P3HT/PCBM blends doped with other spin ½ radicals including (2,2,6,6-Tetramethylpiperidin-1-yl)oxyl (TEMPO), *α,γ*-Bisdiphenylene-β-phenylallyl (BDPA), and bis(1-hydroxy-2,2,4,6,6-pentamethyl-4-piperidinyl) oxalate (molecular structures in Figure 4.19). However, we observed no efficiency enhancement (Table 4.2). Here, we note that not all devices were fabricated under ideal fabrication condition, i.e. oxygen level in glovebox higher than 1 ppm, and therefore, the reference pristine device efficiencies were not as high as 3.4%. However, since both reference and doped devices were fabricated under the same conditions, our conclusions are still valid. For an effective exchange interaction, energy resonance among the interfacial states (CT excitons) and radicals are crucial. Other radicals than galvinoxyl possibly do not have the singly occupied molecular orbital (SOMO) in resonance with the CT states and do not show the improvement in PCE.

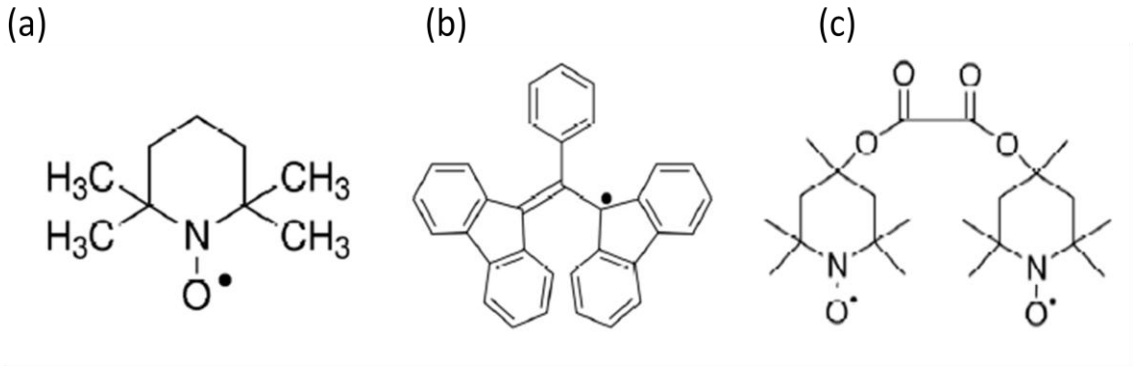

Figure 4.19. Molecular structures of other tested spin ½ radicals. (a) 2,2,6,6-Tetramethylpiperidin-1-yl)oxyl (TEMPO), (b) α,γ-Bisdiphenylene-β-phenylallyl(BDPA) and (c) bis(1-hydroxy-2,2,4,6,6-pentamethyl-4-piperidinyl) oxalate. Black dot denotes unpaired electron.

Table 4.2. The OPV characteristic properties under AM 1.5 illumination condition of P3HT/PCBM OPV devices doped with other spin ½ radicals. Radicals tested were TEMPO, BDPA, and bis(1-hydroxy-2,2,4,6,6-pentamethyl-4-piperidinyl) oxalate, however, no efficiency enhancement were observed.

		J_{sc} (mA/cm^2)	V_{oc} (V)	*FF*	η (%)
TEMPO	**pristine**	**9.3**	**0.61**	**0.51**	**2.9**
	3 wt%	**10.4**	**0.61**	**0.43**	**2.7**
	5 wt%	**10.3**	**0.61**	**0.38**	**2.4**
BDPA	**pristine**	**7.5**	**0.60**	**0.63**	**2.8**
	3 wt%	**7.1**	**0.59**	**0.64**	**2.7**
	6 wt%	**6.4**	**0.57**	**0.42**	**1.6**
bis(1-hydroxy-2,2,4,6,6-pentamethyl-4-piperidinyl)oxalate	**pristine**	**7.4**	**0.57**	**0.66**	**2.8**
	3 wt%	**3.2**	**0.53**	**0.26**	**0.4**
	6 wt%	**1.0**	**0.55**	**0.42**	**0.2**

4.4 Conclusions

We studied the optical and electrical properties of the film and devices of the low bandgap polymer PTB7. We identified the triplet transition in polymer that occurs at 1.1 eV and polaron transitions that occurs at 0.4eV and 1.1eV, as verified by DIA, PADMR, and MPA spectroscopies. The formation of triplet excitons in the presence of radical is analyzed with the PA and MPA method along with the ultrafast pump-probe measurements. Devices based on PTB7/PC60BM blend have shown the enhancement in PCE using the spin ½ additives. We demonstrated that the terminal loss of the photogenerated excitons into the tightly bound triplet states in the blend where the triplet state lies below the CT state can be reduced by manipulating the spins of the charge transfer states. This work provides an avenue for improving the PCE of OPV devices in addition of existing methods in the field. Also, a comparison is made between the devices based on P3HT/PCBM blends of different polymer quality and on the effect of adding galvinoxyl spin ½ radicals.

CHAPTER 5

CONCLUSIONS

In this thesis, we studied optical and electrical properties of films and devices of several organic semiconductors that are used for organic light emitting diodes (OLEDs) and organic photovoltaic (OPV) cells. Several optical techniques such as absorption, photoluminescence (PL), photo-induced absorption (PA), doping-induced absorption (DIA), electro-absorption (EA), photoluminescence quantum efficiency (PLQE), and PA-detected magnetic resonance (PADMR) have been used to study the long-lived photoexcitations such as triplet excitons, polarons, and polaron pairs in the organic semiconductor films. Device characteristic parameters of OPV were obtained by analyzing Current-Voltage (I-V) characteristics for measuring the photocurrent and power conversion efficiency (PCE), whereas Electroluminescence-Voltage (EL-V) characteristics including I-V were used for OLEDs. We also studied magnetic field effect (MFE) such as magneto-PL (MPL) and magneto-PA (MPA) on films; magneto-conductance (MC) and magneto-electroluminescence (MEL) on the OLED. The first two chapters of this thesis are devoted to introduce the field of organic semiconductors and describe the experimental methods used in the present work. Results and discussions of our experimental findings are presented in Chapter 3 and Chapter 4 for OLEDs and OPVs, respectively.

We studied the spin response of various magnetic field effects and magneto-transport in both protonated and deuterated aluminum tris(8-hydroxyquinoline) [Alq_3]-based OLEDs and spin-valve (OSV) devices. We have shown the role of hyperfine interaction (HFI) in MC, MEL, and magneto-resistance (MR) in OSV and OLED. Using the spin ½ conductivity-detected magnetic resonance (CDMR) and MR in OSV devices based on H- and D- Alq_3, we showed that the HFI is a significant spin-mixing mechanism for spin ½ polarons in Alq_3. In addition, the low field (B<20mT) MEL response is also isotope sensitive, showing that HFI-induced spin mixing of polaron-pairs spin sublevels also dominates this field response. However, the MC response was found to be less sensitive to isotope exchange at low fields, in agreement with previous studies. The disparity between the isotope sensitivity of MC and MEL responses in Alq_3 indicates that the HFI in the MC response is overwhelmed by an isotope-independent spin-mixing mechanism. We propose that collisions of spin ½ carriers with triplet polaron-pairs may be the main spin-mixing mechanism in the low field MC response of Alq_3 diodes.

We also studied the energy transfer in OLED devices based on host-guest blends with different guest concentrations of the fluorescent polymer poly-[2-methoxy, 5-(2'-ethyl-hexyloxy)phenylene vinylene] (MEHPPV- host), and phosphorescent molecule PtII–tetraphenyltetrabenzoporphyrin [Pt(tpbp); guest]. We used steady state optical spectroscopy such as PL, PA, and MPA for studying the energy transfer dynamics in the related films. Our study shows that the host triplet exciton density in the blend is significantly enhanced, and the emission intensity is highly reduced for both EL emission in OLEDs and PL emission in films. The underlying mechanism of this curious behavior is the triplet level of MEHPPV. Since E_T(guest)>E_T(host), there is a subsequent Dexter

type energy transfer from E_T(guest) to E_T(host). This energy transfer sequence has profound influence on the PL and EL emission spectra in both films and OLED devices based on the MEHPPV-Pt(tpbp) system. This 'ping-pong' type reaction sequence is unique to this host/guest blend. Furthermore, the MPA and MPL responses in the blend show that the triplet-triplet annihilation (TTA) response occurs at lower laser power in the blend, thus verifying the presence of large number of triplet excitons in the blend system.

We have also shown that the magnetic field can manipulate the EL color in OLEDs. Host-guest blend OLED devices have the advantage of generating broad band white light as compared to single polymer OLED. Here, with the suitable combination of these materials (i.e. matching the emission spectrum of the host to the absorption spectrum of the guest), we showed white OLED in a single layered device. We have explored the possibility of color tuning in such devices via the magnetic field effect, in addition to the current-induced color change. We showed that the underlying mechanism of this color change is the polaron pair model of MFE in OLEDs.

We also fabricated hybrid OLED (h-OLED), where inorganic magnetic tunnel junction (MTJ) is connected in series with OLED. The advantage of large MR of MTJ and large electroluminescence of OLED is combined to produce room temperature spin manipulated MEL. The large resistance mismatch between MTJ and OLEDs that has been considered a bottleneck for organic-based devices is suppressed due to the nonlinear *I-V* response of the OLED component in the space charge limited current regime. At RT the h-OLED devices exhibit up to 80 % giant MEL in the red, green, and blue spectral ranges, which may be controlled either by a local magnetic field or a field in a remote

operational mode. The novel h-OLED device opens a new avenue in the application of multifunctional organic displays.

We also studied the optical and electrical properties of the film and devices of the low bandgap polymer PTB7 (fluorinated poly-thienothiophene-benzodithiophene). We used varieties of optoelectronic techniques such as PA, MPA, DIA, and PADMR to identify and monitor the triplet exciton densities. We identified the triplet transition in polymer that occurs at 1.1 eV, and polaron transitions that occurs at 0.4eV and 1.1eV. The formation of triplet excitons in the presence of radical was analyzed with the PA and MPA method along with the ultrafast pump-probe measurements. We found that one of the major losses that limit the power conversion efficiency of OPV devices is the formation of triplet excitons in the polymer through recombination of charge-transfer (CT) excitons at the donor-acceptor interface, and presented a method to suppress the dissociation of CT states by incorporating additives such as the spin ½ radical galvinoxyl in the bulk heterojunction architecture. We have shown that the 30% enhancement in PCE of the cell in the presence of galvinoxyl is due to the suppression of CT recombination channel. Also, correlation between performances of a photovoltaic cell based on different film qualities such as high and low molecular weight; regio-regular and region-random P3HT (poly(3-hexylthiophene)) was explored.

REFERENCES

[1] O. Ostroverkhova, Handbook of Organic Materials for Optical and (Opto) Electronic Devices: Properties And Applications, Elsevier, 2013.

[2] S. Günes, H. Neugebauer, N.S. Sariciftci, Chemical Reviews, 107 (2007) 1324-1338.

[3] J. Burroughes, D. Bradley, A. Brown, R. Marks, K. Mackay, R. Friend, P. Burns, A. Holmes, Nature, 347 (1990) 539-541.

[4] N. Sariciftci, L. Smilowitz, A. Heeger, F. Wudl, Science, 258 (1992) 1474-1476.

[5] G. Horowitz, Advanced Materials, 10 (1998) 365-377.

[6] Z. Xiong, D. Wu, Z.V. Vardeny, J. Shi, Nature, 427 (2004) 821-824.

[7] W. Baker, K. Ambal, D. Waters, R. Baarda, H. Morishita, K. van Schooten, D.R. McCamey, J.M. Lupton, C. Boehme, Nature Communications, 3 (2012) 898.

[8] A.G. MacDiarmid, Angewandte Chemie International Edition, 40 (2001) 2581-2590.

[9] A.J. Heeger, S. Kivelson, J. Schrieffer, W.-P. Su, Reviews of Modern Physics, 60 (1988) 781.

[10] R.E. Peierls, Quantum Theory of Solids, Oxford University Press, 1955.

[11] W.-P. Su, J. Schrieffer, A. Heeger, Physical Review B, 22 (1980) 2099.

[12] S. Mazumdar, S. Dixit, Physical Review Letters, 51 (1983) 292-295.

[13] D. Campbell, A. Bishop, Nuclear Physics B, 200 (1982) 297-328.

[14] H. Mizes, E. Conwell, Physical Review B, 50 (1994) 70211-11246.

[15] C.W. Tang, Applied Physics Letters, 48 (1986) 183-185.

[16] G. Yu, J. Gao, J. Hummelen, F. Wudl, A. Heeger, Science, 270 (1995) 1789-1791.

[17] A.J. Moulé, K. Meerholz, Advanced Materials, 20 (2008) 240-245.

[18] Y. Gao, J.K. Grey, Journal of the American Chemical Society, 131 (2009) 9654-9662.

[19] R. Noriega, J. Rivnay, K. Vandewal, F.P. Koch, N. Stingelin, P. Smith, M.F. Toney, A. Salleo, Nature Materials, 12 (2013) 1038-1044.

[20] S. Singh, B. Pandit, T.P. Basel, S. Li, D. Laird, Z.V. Vardeny, Physical Review B, 85 (2012) 205206.

[21] A.A. Bakulin, A. Rao, V.G. Pavelyev, P.H. van Loosdrecht, M.S. Pshenichnikov, D. Niedzialek, J. Cornil, D. Beljonne, R.H. Friend, Science, 335 (2012) 1340-1344.

[22] J.J. Benson-Smith, L. Goris, K. Vandewal, K. Haenen, J.V. Manca, D. Vanderzande, D.D. Bradley, J. Nelson, Advanced Functional Materials, 17 (2007) 451-457.

[23] T. Drori, J. Holt, Z. Vardeny, Physical Review B, 82 (2010) 075207.

[24] A. Rao, P.C. Chow, S. Gélinas, C.W. Schlenker, C.-Z. Li, H.-L. Yip, A.K.-Y. Jen, D.S. Ginger, R.H. Friend, Nature, 500 (2013) 435-439.

[25] C. Tang, S. VanSlyke, Applied Physics Letters, 51 (1987) 913.

[26] H. Bässler, Physica Status Solidi (b), 175 (1993) 15-56.

[27] R. Friend, R. Gymer, A. Holmes, J. Burroughes, R. Marks, C. Taliani, D. Bradley, D. Dos Santos, J. Bredas, M. Lögdlund, Nature, 397 (1999) 121-128.

[28] M. Baldo, D. O'brien, Y. You, A. Shoustikov, S. Sibley, M. Thompson, S. Forrest, Nature, 395 (1998) 151-154.

[29] H. Uoyama, K. Goushi, K. Shizu, H. Nomura, C. Adachi, Nature, 492 (2012) 234-238.

[30] M.A. Lampert, P. Mark, Current Injection in Solids, Academic Press New York, 1970.

[31] V. Coropceanu, J. Cornil, D.A. da Silva Filho, Y. Olivier, R. Silbey, J.-L. Brédas, Chemical Reviews, 107 (2007) 926-952.

[32] R.H. Parmenter, W. Ruppel, Journal of Applied Physics, 30 (2004) 1548-1558.

[33] D. Sun, L. Yin, C. Sun, H. Guo, Z. Gai, X.-G. Zhang, T.Z. Ward, Z. Cheng, J. Shen, Physical Review Letters, 104 (2010) 236602.

[34] M. Julliere, Physics Letters A, 54 (1975) 225-226.

[35] J. Kalinowski, M. Cocchi, D. Virgili, P. Di Marco, V. Fattori, Chemical Physics Letters, 380 (2003) 710-715.

[36] V. Prigodin, J. Bergeson, D. Lincoln, A. Epstein, Synthetic Metals, 156 (2006) 757-761.

[37] P. Bobbert, T. Nguyen, F. Van Oost, v.B. Koopmans, M. Wohlgenannt, Physical Review Letters, 99 (2007) 216801.

[38] F. Wang, H. Bässler, Z.V. Vardeny, Physical Review Letters, 101 (2008) 236805.

[39] P. Desai, P. Shakya, T. Kreouzis, W. Gillin, N. Morley, M. Gibbs, Phys. Rev. B, 75 (2007) 094423.

[40] S. Zhang, T. Kreouzis, W. Gillin, Synthetic Metals, 173 (2013) 46-50.

[41] J. Rybicki, T.D. Nguyen, Y. Sheng, M. Wohlgenannt, Synthetic Metals, 160 (2010) 280-284.

[42] E. Ehrenfreund, Z.V. Vardeny, Israel Journal of Chemistry, 52 (2012) 552-562.

[43] T. Nguyen, B. Gautam, E. Ehrenfreund, Z.V. Vardeny, Physical Review Letters, 105 (2010) 166804.

[44] M. Liess, S. Jeglinski, Z. Vardeny, M. Ozaki, K. Yoshino, Y. Ding, T. Barton, Physical Review B, 56 (1997) 15712.

[45] X. Wei, PhD Thesis, Unpublished, 1992.

[46] C. Tang, S. VanSlyke, C. Chen, Journal of Applied Physics, 65 (1989) 3610.

[47] W. Li, R.A. Jones, S.C. Allen, J.C. Heikenfeld, A.J. Steckl, Journal of Display Technology, 2 (2006) 143-152.

[48] Ö. Mermer, G. Veeraraghavan, T. Francis, Y. Sheng, D. Nguyen, M. Wohlgenannt, A. Köhler, M. Al-Suti, M. Khan, Physical Review B, 72 (2005) 205202.

[49] Y. Sheng, T. Nguyen, G. Veeraraghavan, Ö. Mermer, M. Wohlgenannt, S. Qiu, U. Scherf, Physical Review B, 74 (2006) 045213.

[50] C. Garditz, A.G. Muckl, M. Colle, Journal of Applied Physics, 98 (2005) 104507-104507-104504.

[51] N.J. Rolfe, M. Heeney, P.B. Wyatt, A.J. Drew, T. Kreouzis, W.P. Gillin, Physical Review B, 80 (2009) 241201.

[52] J. Gomez, F. Nüesch, L. Zuppiroli, C. Graeff, Synthetic Metals, 160 (2010) 317-319.

[53] B. Koopmans, W. Wagemans, F.L. Bloom, P.A. Bobbert, M. Kemerink, M. Wohlgenannt, Philosophical Transactions of the Royal Society A: Mathematical, Physical and Engineering Sciences, 369 (2011) 3602-3616.

[54] A. Carrington, A.D. McLachlan, Introduction to Magnetic Resonance: with Applications to Chemistry and Chemical Physics, Harper & Row New York, 1967.

[55] T.D. Nguyen, G. Hukic-Markosian, F. Wang, L. Wojcik, X.-G. Li, E. Ehrenfreund, Z.V. Vardeny, Nature Materials, 9 (2010) 345-352.

[56] C.C. Tong, K.C. Hwang, The Journal of Physical Chemistry C, 111 (2007) 3490-3494.

[57] F. Wang, C. Yang, E. Ehrenfreund, Z. Vardeny, Synthetic Metals, 160 (2010) 297-302.

[58] M. Colle, C. Garditz, M. Braun, Journal of Applied Physics, 96 (2004) 6133-6141.

[59] H.D. Burrows, M. Fernandes, J. Seixas de Melo, A.P. Monkman, S. Navaratnam, Journal of the American Chemical Society, 125 (2003) 15310-15311.

[60] H. Hayashi, Introduction to Dynamic Spin Chemistry: Magnetic Field Effects upon Chemical and Biochemical Reactions, World Scientific, 2004.

[61] C. Timmel, U. Till, B. Brocklehurst, K. McLauchlan, P. Hore, Molecular Physics, 95 (1998) 71-89.

[62] J. Tang, J. Norris, Chemical Physics Letters, 92 (1982) 136-140.

[63] V. Ern, R. Merrifield, Physical Review Letters, 21 (1968) 609-611.

[64] U.E. Steiner, T. Ulrich, Chemical Reviews, 89 (1989) 51-147.

[65] A. Abragam, B. Bleaney, Electron Paramagnetic Resonance of Transition Ions, Clarendon Press Oxford, 1970.

[66] J. Kido, K. Hongawa, K. Okuyama, K. Nagai, Applied Physics Letters, 64 (1994) 815-817.

[67] M.C. Gather, A. Köhnen, K. Meerholz, Advanced Materials, 23 (2011) 233-248.

[68] F.B. Dias, K.N. Bourdakos, V. Jankus, K.C. Moss, K.T. Kamtekar, V. Bhalla, J. Santos, M.R. Bryce, A.P. Monkman, Advanced Materials, 25 (2013) 3707-3714.

[69] F. Kessler, Y. Watanabe, H. Sasabe, H. Katagiri, M.K. Nazeeruddin, M. Grätzel, J. Kido, Journal of Materials Chemistry C, 1 (2013) 1070-1075.

[70] C.-H. Lin, Y.-C. Chiu, Y. Chi, Y.-T. Tao, L.-S. Liao, M.-R. Tseng, G.-H. Lee, Organometallics, 31 (2012) 4349-4355.

[71] A.H. Davis, K. Bussmann, Journal of Vacuum Science & Technology A: Vacuum, Surfaces, and Films, 22 (2004) 1885-1891.

[72] M. Baldo, D. O'brien, M. Thompson, S. Forrest, Physical Review B, 60 (1999) 14422.

[73] R. Holmes, B. DAndrade, S. Forrest, X. Ren, J. Li, M. Thompson, Applied Physics Letters, 83 (2003) 3818-3820.

[74] B.C. Krummacher, V.-E. Choong, M.K. Mathai, S.A. Choulis, F. So, F. Jermann, T. Fiedler, M. Zachau, Applied Physics Letters, 88 (2006) 113506.

[75] Y. Yuan, S. Li, Z. Wang, H. Xu, X. Zhou, Optics Express, 17 (2009) 1577-1582.

[76] E.L. Williams, K. Haavisto, J. Li, G.E. Jabbour, Advanced Materials, 19 (2007) 197-202.

[77] Y. Sun, N.C. Giebink, H. Kanno, B. Ma, M.E. Thompson, S.R. Forrest, Nature, 440 (2006) 908-912.

[78] T. Drori, E. Gershman, C. Sheng, Y. Eichen, Z.V. Vardeny, E. Ehrenfreund, Physical Review B, 76 (2007) 033203.

[79] C. Borek, K. Hanson, P.I. Djurovich, M.E. Thompson, K. Aznavour, R. Bau, Y. Sun, S.R. Forrest, J. Brooks, L. Michalski, Angewandte Chemie, 119 (2007) 1127-1130.

[80] J.R. Sommer, A.H. Shelton, A. Parthasarathy, I. Ghiviriga, J.R. Reynolds, K.S. Schanze, Chemistry of Materials, 23 (2011) 5296-5304.

[81] I. Campbell, D. Smith, S. Tretiak, R. Martin, C. Neef, J. Ferraris, Physical Review B, 65 (2002) 085210.

[82] X. Gong, J.C. Ostrowski, D. Moses, G.C. Bazan, A.J. Heeger, Advanced Functional Materials, 13 (2003) 439-444.

[83] A. Monkman, H. Burrows, L. Hartwell, L. Horsburgh, I. Hamblett, S. Navaratnam, Physical Review Letters, 86 (2001) 1358.

[84] H.D. Burrows, J.S. de Melo, C. Serpa, L. Arnaut, A.P. Monkman, I. Hamblett, S. Navaratnam, The Journal of Chemical Physics, 115 (2001) 9601.

[85] M.T. Whited, P.I. Djurovich, S.T. Roberts, A.C. Durrell, C.W. Schlenker, S.E. Bradforth, M.E. Thompson, Journal of the American Chemical Society, 133 (2010) 88-96.

[86] B. Hu, Y. Wu, Nature Materials, 6 (2007) 985-991.

[87] J. Rybicki, R. Lin, F. Wang, M. Wohlgenannt, C. He, T. Sanders, Y. Suzuki, Physical Review Letters, 109 (2012) 076603.

[88] B.R. Gautam, T.D. Nguyen, E. Ehrenfreund, Z.V. Vardeny, Physical Review B, 85 (2012) 205207.

[89] W. Wagemans, F. Bloom, P. Bobbert, M. Wohlgenannt, B. Koopmans, Journal of Applied Physics, 103 (2008) 07F303.

[90] J. Bergeson, V. Prigodin, D. Lincoln, A. Epstein, Physical Review Letters, 100 (2008) 067201.

[91] R. Liu, Y. Zhang, Y. Lei, P. Chen, Z. Xiong, Journal of Applied Physics, 105 (2009) 093719.

[92] A. Cadby, P. Lane, H. Mellor, S. Martin, M. Grell, C. Giebeler, D. Bradley, M. Wohlgenannt, C. An, Z. Vardeny, Physical Review B, 62 (2000) 15604.

[93] A. Hayer, A.L. Khan, R.H. Friend, A. Köhler, Physical Review B, 71 (2005) 241302.

[94] L. Herz, R. Phillips, Physical Review B, 61 (2000) 13691.

[95] G. Zeng, W.-L. Yu, S.-J. Chua, W. Huang, Macromolecules, 35 (2002) 6907-6914.

[96] U. Lemmer, S. Heun, R. Mahrt, U. Scherf, M. Hopmeier, U. Siegner, Chemical Physics Letters, 240 (1995) 373-378.

[97] X. Gong, P.K. Iyer, D. Moses, G.C. Bazan, A.J. Heeger, S.S. Xiao, Advanced Functional Materials, 13 (2003) 325-330.

[98] L. Romaner, A. Pogantsch, P. Scandiucci de Freitas, U. Scherf, M. Gaal, E. Zojer, E.J. List, Advanced Functional Materials, 13 (2003) 597-601.

[99] S.R. Forrest, Nature, 428 (2004) 911-918.

[100] A. Hepp, H. Heil, W. Weise, M. Ahles, R. Schmechel, H. von Seggern, Physical Review Letters, 91 (2003) 157406.

[101] C.J. Brabec, S. Gowrisanker, J.J. Halls, D. Laird, S. Jia, S.P. Williams, Advanced Materials, 22 (2010) 3839-3856.

[102] T.D. Nguyen, E. Ehrenfreund, Z.V. Vardeny, Science, 337 (2012) 204-209.

[103] V.A. Dediu, L.E. Hueso, I. Bergenti, C. Taliani, Nature Materials, 8 (2009) 707-716.

[104] C. Barraud, P. Seneor, R. Mattana, S. Fusil, K. Bouzehouane, C. Deranlot, P. Graziosi, L. Hueso, I. Bergenti, V. Dediu, Nature Physics, 6 (2010) 615-620.

[105] F. Wang, Z.V. Vardeny, Synthetic Metals, 160 (2010) 210-215.

[106] V. Dediu, L. Hueso, I. Bergenti, A. Riminucci, F. Borgatti, P. Graziosi, C. Newby, F. Casoli, M. De Jong, C. Taliani, Physical Review B, 78 (2008) 115203.

[107] T. Santos, J. Lee, P. Migdal, I. Lekshmi, B. Satpati, J. Moodera, Physical Review Letters, 98 (2007) 016601.

[108] S.S. Parkin, C. Kaiser, A. Panchula, P.M. Rice, B. Hughes, M. Samant, S.-H. Yang, Nature Materials, 3 (2004) 862-867.

[109] S. Parkin, X. Jiang, C. Kaiser, A. Panchula, K. Roche, M. Samant, Proceedings of the IEEE, 91 (2003) 661-680.

[110] W. Butler, X.-G. Zhang, T. Schulthess, J. MacLaren, Physical Review B, 63 (2001) 054416.

[111] S. Ikeda, J. Hayakawa, Y. Ashizawa, Y. Lee, K. Miura, H. Hasegawa, M. Tsunoda, F. Matsukura, H. Ohno, Applied Physics Letters, 93 (2008) 082508.

[112] T. Nguyen, Y. Sheng, J. Rybicki, M. Wohlgenannt, Physical Review B, 77 (2008) 235209.

[113] M. Reufer, M.J. Walter, P.G. Lagoudakis, A.B. Hummel, J.S. Kolb, H.G. Roskos, U. Scherf, J.M. Lupton, Nature Materials, 4 (2005) 340-346.

[114] B. Hu, L. Yan, M. Shao, Advanced Materials, 21 (2009) 1500-1516.

[115] X. Gong, W. Ma, J.C. Ostrowski, G.C. Bazan, D. Moses, A.J. Heeger, Advanced Materials, 16 (2004) 615-619.

[116] Y. Kawamura, K. Goushi, J. Brooks, J.J. Brown, H. Sasabe, C. Adachi, Applied Physics Letters, 86 (2005) 071104.

[117] In CIE (1931) chromaticity diagram, with the coordinates corresponding to the emission from h-WOLED device (x=0.3754, y=0.4505), the human eye perceives this color as white (the equi-enery point for pure white light (0.333, 0.333)).

[118] J. You, L. Dou, K. Yoshimura, T. Kato, K. Ohya, T. Moriarty, K. Emery, C.-C. Chen, J. Gao, G. Li, Nature Communications, 4 (2013) 1446.

[119] G. Li, R. Zhu, Y. Yang, Nature Photonics, 6 (2012) 153-161.

[120] F.C. Krebs, N. Espinosa, M. Hösel, R.R. Søndergaard, M. Jørgensen, Advanced Materials, 26 (2014) 29-39.

[121] G. Li, V. Shrotriya, J. Huang, Y. Yao, T. Moriarty, K. Emery, Y. Yang, Nature Materials, 4 (2005) 864-868.

[122] D. Venkataraman, S. Yurt, B.H. Venkatraman, N. Gavvalapalli, The Journal of Physical Chemistry Letters, 1 (2010) 947-958.

[123] Y. Liang, Z. Xu, J. Xia, S.T. Tsai, Y. Wu, G. Li, C. Ray, L. Yu, Advanced Materials, 22 (2010) E135-E138.

[124] M. Morana, H. Azimi, G. Dennler, H.J. Egelhaaf, M. Scharber, K. Forberich, J. Hauch, R. Gaudiana, D. Waller, Z. Zhu, Advanced Functional Materials, 20 (2010) 1180-1188.

[125] Y. Liang, L. Yu, Accounts of Chemical Research, 43 (2010) 1227-1236.

[126] L. Dou, C.-C. Chen, K. Yoshimura, K. Ohya, W.-H. Chang, J. Gao, Y. Liu, E. Richard, Y. Yang, Macromolecules, 46 (2013) 3384-3390.

[127] Y. Zhu, R.D. Champion, S.A. Jenekhe, Macromolecules, 39 (2006) 8712-8719.

[128] Y. Zhang, T.P. Basel, B.R. Gautam, X. Yang, D.J. Mascaro, F. Liu, Z.V. Vardeny, Nature Communications, 3 (2012) 1043.

[129] J.H. Seo, A. Gutacker, Y. Sun, H. Wu, F. Huang, Y. Cao, U. Scherf, A.J. Heeger, G.C. Bazan, Journal of the American Chemical Society, 133 (2011) 8416-8419.

[130] J.-H. Huang, J.-H. Fang, C.-C. Liu, C.-W. Chu, ACS Nano, 5 (2011) 6262-6271.

[131] J. Gilot, M.M. Wienk, R.A. Janssen, Advanced Materials, 22 (2010) E67-E71.

[132] M. Reyes-Reyes, K. Kim, D.L. Carroll, Applied Physics Letters, 87 (2005) 083506.

[133] R. Tautz, E. Da Como, T. Limmer, J. Feldmann, H.-J. Egelhaaf, E. Von Hauff, V. Lemaur, D. Beljonne, S. Yilmaz, I. Dumsch, Nature Communications, 3 (2012) 970.

[134] M.K. Etherington, J. Wang, P.C. Chow, N.C. Greenham, Applied Physics Letters, 104 (2014) 063304.

[135] J.M. Szarko, B.S. Rolczynski, S.J. Lou, T. Xu, J. Strzalka, T.J. Marks, L. Yu, L.X. Chen, Advanced Functional Materials, 24 (2014) 10-26.

[136] D. Veldman, S.C. Meskers, R.A. Janssen, Advanced Functional Materials, 19 (2009) 1939-1948.

[137] G. Hukic-Markosian, T. Basel, S. Singh, Z.V. Vardeny, S. Li, D. Laird, Applied Physics Letters, 100 (2012) 213903.

[138] M.S. Su, C.Y. Kuo, M.C. Yuan, U. Jeng, C.J. Su, K.H. Wei, Advanced Materials, 23 (2011) 3315-3319.

[139] R.J. Kline, M.D. McGehee, E.N. Kadnikova, J. Liu, J.M. Fréchet, Advanced Materials, 15 (2003) 1519-1522.

[140] S. Shaked, S. Tal, Y. Roichman, A. Razin, S. Xiao, Y. Eichen, N. Tessler, Advanced Materials, 15 (2003) 913-916.

[141] M. Hallermann, S. Haneder, E. Da Como, Applied Physics Letters, 93 (2008) 053307.

[142] I. Novak, B. Kovač, Chemical Physics Letters, 413 (2005) 351-355.